Exfoliation of Conductive Layered Materials in Solutions

Kumulative Dissertation

zur Erlangang des Grades

,,Doktor der Naturwissenschaften‘‘

im Fachbereich Chemie, Pharmazie, und Geowissenschaften der

Johannes Gutenberg-Universität Mainz und in Kooperation mit dem

Max-Planck-Institut für Polymerforschung Mainz

vorgelegt von

Sheng Yang

geboren in Chongqing / China

Mainz, 2018

Dekan: Prof. Dr.
1. Berichterstatter: Prof. Dr.
2. Berichterstatter: Prof. Dr.
Tag der mündlichen Prüfung:

Die vorliegende Arbeit wurde in der Zeit von September 2013 bis August 2017 im Max-Planck-Institut für Polymerforschung in Mainz unter der Betreuung von Prof. Dr. [redacted] durchgeführt.

Ich danke Prof. Dr. [redacted] für seine wissenschaftliche und persönliche Unterstützung sowie für seine ständige Diskussionsbereitschaft.

Table of Contents

Chapter 1 Introduction

1.1 Layered materials

As early as 300 AD, Mayans in Mesoamerica started to produce dyes as part of their ritual sacrifices. Those pigments on murals, called Maya blue, kept stunning for thousands of years, in spite of the hot, humid climate. However, the origin of their colour and their resistance to corrosion was not fully understood until 1996, when researchers uncovered that the mystery behind it was palygorskite, a fibrous magnesium aluminum silicate, which was constructed by two-dimensional silicon-oxygen layers (Fig. 1.1).[1]

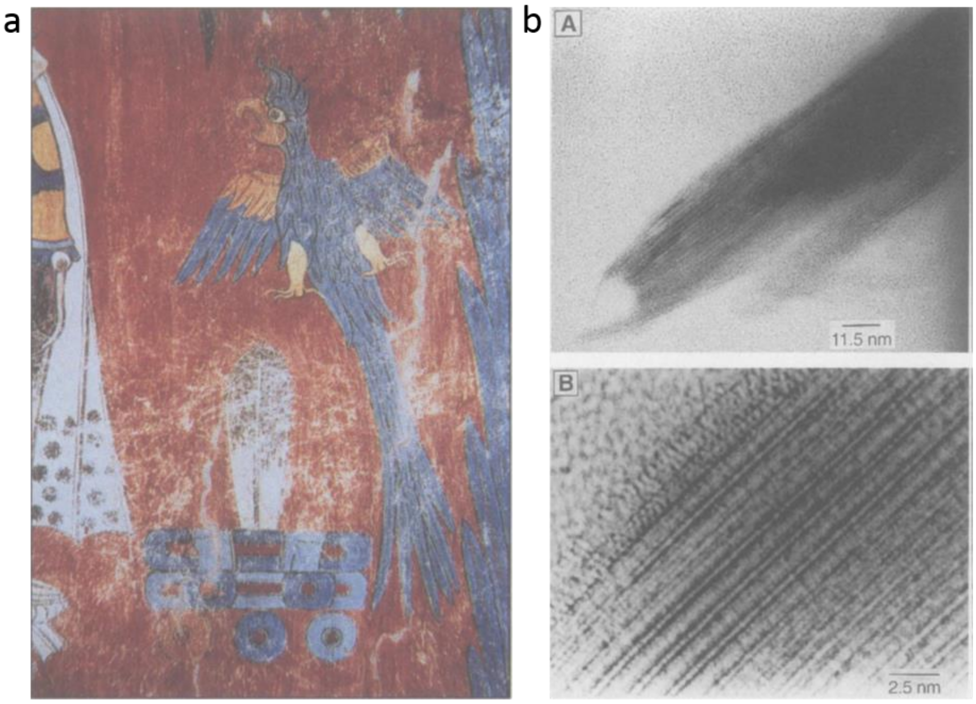

Figure 1.1 a) Maya blue used on mural, b) The structure of palygorskite crystals [1]

In fact, such layered solids are widespread on our planet. Most of them consist of successive layers of chemically bonded atomic layers with the thickness ranging from one to multiple atoms. Individual layers are held together by weak out-of-plane interactions such as van der Waals forces.[2] Therefore, these layered compounds are generally categorized into the group of "van der Waals solids", which contain a variety of materials up to date (Fig. 1.2). The simplest model is graphite, which is built by hexagonal atomically thin carbon layers. The carbon atoms are distributed in a honeycomb lattice, and the distance between each layer is 0.33 nm. As another single-element layered material, black phosphorus (BP) is the most stable allotrope of phosphorus that demonstrates a puckered orthorhombic structure with an interlayer distance of 0.53 nm.[3] Beyond that, boron nitride (BN), often referred to as "white graphite", has the same hexagonal structure as graphite but is an electrical insulator. Transition metal dichalcogenides (TMDs, such as MoS_2, WS_2) contain a plane of metal atoms sandwiched with two layers of halide or chalcogen atoms.[4] Similarly, layered double hydroxide (LDHs, such as $Zn_6Al_2(OH)_{16}$), layered metal oxides (such as TiO_2, MnO_2) and layered clays (such as hydrated phyllosilicates) have been extensively studied in the field of layered materials.[5] Recently, a new group of layered compounds, namely MAX phases, has unleashed a great deal of attention. There, M refers to an early transition metal, A is a group IIIA or IVA element and X is C and/or N. One of their unique features is, that the separated layers are not connected by weak van der Waals force, but solely by strong metallic bonds.[6]

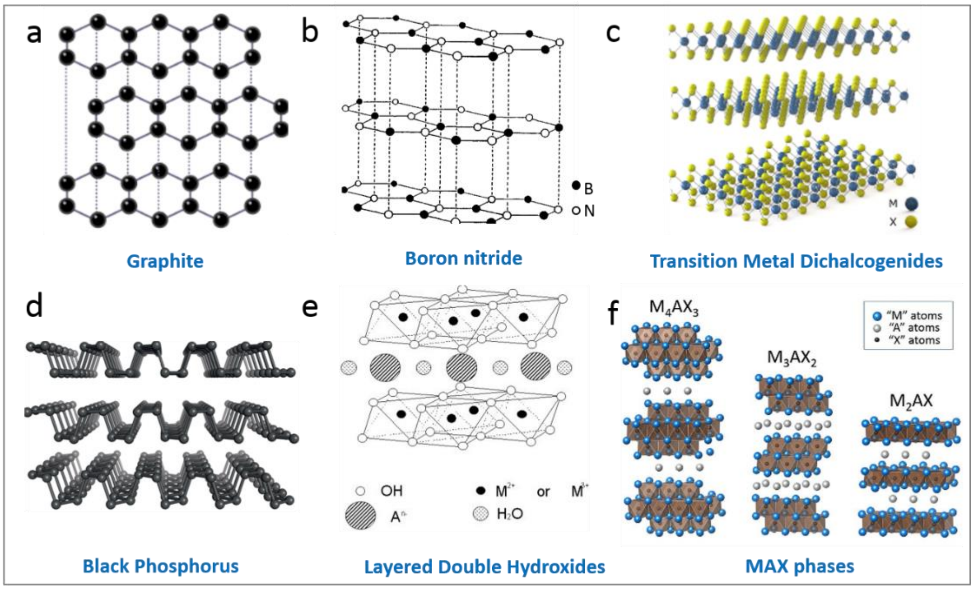

Figure 1.2 Schematic structure of typical layered materials including a) graphite, b) boron nitride, c) transition metal dichalcogenides,[7] d) black phosphorus,[8] e) layered

double hydroxides[9] and f) MAX phases (Source: a: www.bbc.co.uk/education/guides /zjgmn39/revision; b: www.google.com/patents/US8288466; f : https://en. wikipedia. org/wiki/MXenes)

1.2 Two-dimensional materials

The delamination of van der Waals crystals gives birth to individual atomic thin layers. In theory, the weak interlayer interactions are easy to overcome using external forces or chemical intercalation methods. However, the laminar structures and properties of thin layered materials were not well understood until recently, when graphite was used as the initial test model for chemists to develop intercalation chemistry, which eventually paved a way to kinetically stable two-dimensional (2D) flakes. Two-dimensional materials, with fully accessible surface areas, brought enhanced chemical reactivity and unprecedented physical properties. Particularly, graphene, a monolayer of graphite, was discovered by mechanical exfoliation for the first time. This breakthrough work conducted by Geim and Novoselov was honoured with the Nobel Prize for Physics in 2010. Graphene exhibits a wide array of outstanding physical properties, such as high transparency (97.7 %)[10] and Young's modulus (~1.0 TPa),[11] high intrinsic mobility (~200,000 $cm^2 V^{-1} s^{-1}$),[12] high surface area (2630 $m^2 g^{-1}$),[13] strikingly different from its bulk, layered counterpart. Nevertheless, graphene does not have an intrinsic band gap (nearly 0 eV).[14] It requires post-functionalization or size confinement to open the band gap.[15] Therefore, sustainable efforts have been devoted to developing other non-carbon-based 2D materials, boosting the studies on their synthesis and characterization, from semiconducting TMDs, insulating *h*-BN, to many other elemental 2D systems including germanene, single-layer antimony and black phosphorus.[16]

In terms of electronic properties, molybdenum disulfide (MoS_2) and tungsten diselenide (WSe_2) monolayers own an intrinsic band gap in the range of 1.0-2.0 eV.[17] However, there is still a huge space between zero bandgap graphene and wide bandgap TMDs. Recently, black phosphorus fills the gap. It has variable band gaps from 0.3 eV (bulk crystal) to 2.0 eV (single layer),[18] which has potential prospects in novel electronics and optoelectronics. Besides, boron nitride thin layers have very wide band gap nearly 6.0 eV [19] and poor chemical reactivity, which are ideal for insulating coating or anticorrosion. Therefore, 2D materials are useful toolkits for the design of electronics or synthesis of hybrid composites, as they cover almost the entire band gap (from 0 to 6.0 eV) (Fig. 1.3). However, because the physical and chemical properties of 2D materials strongly depend on their thickness and surface functionalities, to access the superlative properties of 2D materials, efficient synthetic protocols are critically important.

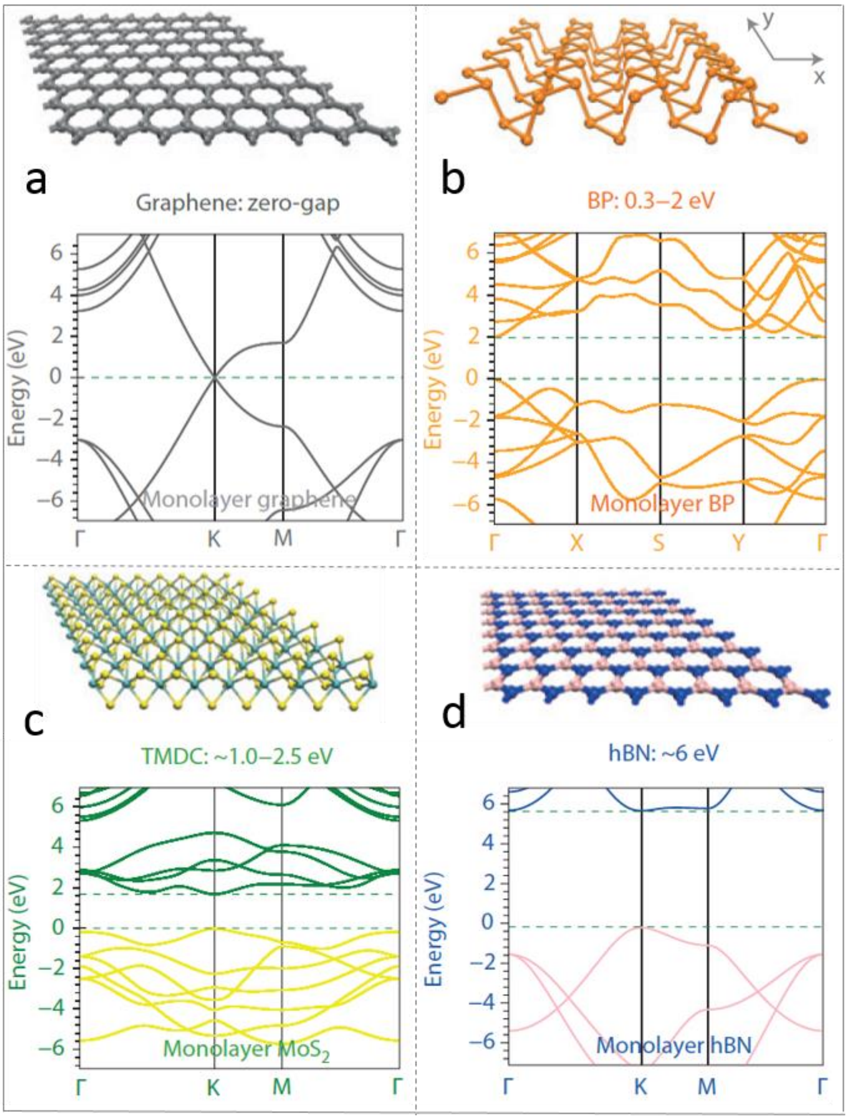

Figure 1.3 Band structure of monolayer (a) graphene, (b) BP, (c) MoS_2 and (d) *h*-BN.[20]

1.3 Synthesis of graphene and other two-dimensional materials

From the synthetic point of view, 2D materials can be obtained by either top-down or bottom-up methods. Top-down methods refer to the separation of bulk layered materials into thin sheets. In an ideal case, the original integrity of the flakes is not interrupted. For commonly-used van der Waals solids, the key issue of exfoliation is on overcoming interlayer interaction in parent crystals. The pioneering work in early 18th century was carried out through chemical oxidation and/or chemical intercalating reactions to prepare oxidized or intercalated precursors, such as graphite oxide or graphite intercalated compounds.[21] Oxidation is very effective but destructive to the intact structure of 2D materials, considering that some of them are chemically unstable. At the beginning of the 20th century, mechanical cleavage and liquid sonication have been developed as the most popular methods to minimize the density of defects on the exfoliated flakes.[5] Conversely, bottom-up methods rely on the chemical reactions to organize small molecules into covalently-linked, structurally well-defined flakes or monolayers. Usually, bottom-up synthesis takes place in solutions[22] or solid surfaces,[23] through assembly of building blocks to produce high-quality graphene and other 2D networks with designed components or structures.

1.3.1 Mechanical cleavage

Two major mechanical forces, i.e. adhesive force and shear force, are able to peel off individual layers from bulk crystal. Adhesive force, caused by the physical interaction between 2D surfaces and the polymer coating on scotch tape, usually applies along the vertical direction towards 2D surface. On the other hand, shear force is unaligned force that pushes simultaneously in two opposite directions, at the top and the bottom, thus causing the layers to slide horizontally along the 2D surfaces.[24]

Micromechanical exfoliation, also known as Scotch-tape cleavage, is effective to reduce the layer numbers of graphite. The process is very simple. Basically, when the fresh surface of HOPG (i.e. highly oriented pyrolytic graphite) was pressed against scotch tape, adhesive force was strong enough to overcome the stacking interactions and a thin layer of material was detached that could be transferred onto any surfaces. After repeating the processes, the thickness of flakes can be decreased down to monolayers (Fig. 1.4). Novoselov and Geim were the pioneers to prepare graphene flakes with this method in 2004.[25] The obtained monolayer graphene flake exhibits a remarkable room-temperature mobility of ~10,000 cm^2 V^{-1} s^{-1}. Inspired by that, many 2D materials have been subsequently investigated. For instance, a single-layer MoS_2 sheet delivers a field effect mobility of 200 cm^2 V^{-1} s^{-1} at room temperature with hafnium oxide gate dielectric.[26] WS_2 monolayer shows a hole mobility of 83 cm^2 V^{-1} s^{-1} at ambient temperature with Al_2O_3 dielectric and thiol passivation.[27] Using MoS_2 atomic layers as model material, the detaching process of this technique was monitored under direct *in situ* transmission electron microscopy (TEM) that was able to control the layer numbers from a monolayer to multiple layers.[28] Based on the force balance near the contact point, the specific surface energy of a single-layer MoS_2 was estimated to be 0.11 N m^{-1}. Although micromechanical cleavage has extremely low efficiency, up to date, it is still the most popular protocol for physicists to access pristine, clean and high-quality 2D flakes.

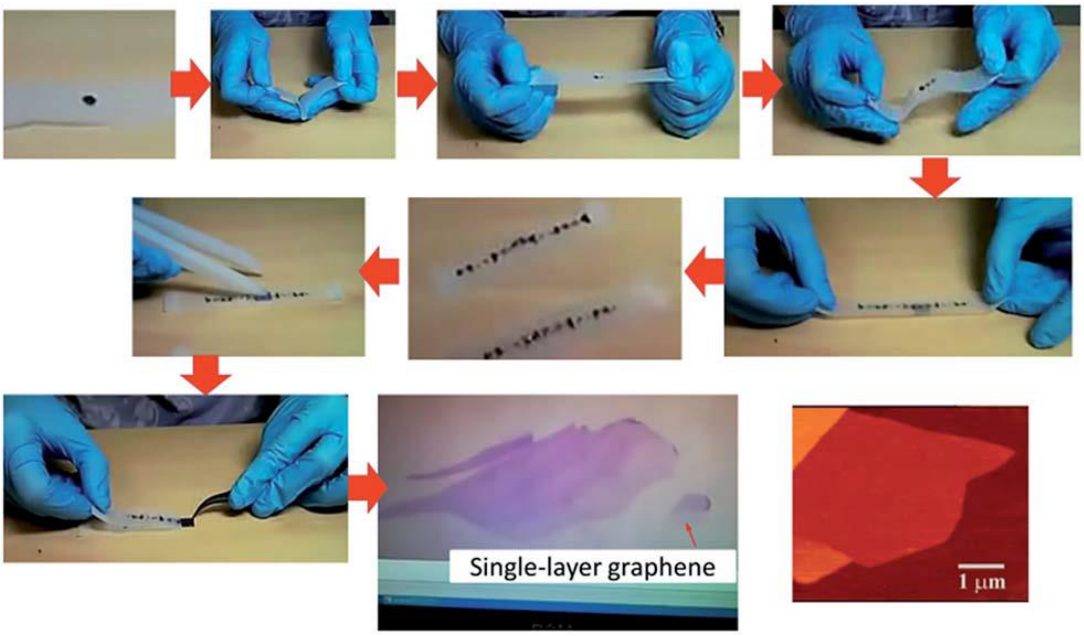

Figure 1.4 A typical process for micromechanical cleavage of HOPG.[24]

Ball milling is another effective mechanical method, which makes use of molecular adsorption and mechanical shear stress.[29] The general process consists of planetary ball mills and grinding media (either liquids or solids). Graphene production using this system has been studied in the wet state with proper organic solvents like *N,N*-dimethylformamide (DMF) and *N*-methyl-2-pyrrolidone (NMP).[30] As an example, ball milling with zirconium oxide balls in NMP can directly delaminate graphite without using any additives.[31] The exfoliation yield is about 26 % and a high-concentration graphene dispersion (2.6 mg mL^{-1}) has been achieved. Under solid conditions, graphene sheets are produced through non-covalent interaction with triazine derivatives.[32] Especially, the use of melamine facilitates the production of a graphene dispersion with concentration of 0.38 mg mL^{-1} in DMF, much higher than that from other triazine compounds (0.06-0.18 mg mL^{-1}). Ball milling in the presence of dry ice (i.e carbon dioxide) functionalizes the edges of exfoliated graphene with carboxylic groups. Such edge-carboxylated graphite has great dispersibility in many solvents and can be spontaneously exfoliated into single and few-layer graphene flakes.[33] Based on the formation of a hydrogen-bonding network, hydroxide-assisted ball milling is also effective for the scalable exfoliation of boron nitride (BN) with yield of 18 %.[34] The exfoliated BN flakes can form a stable dispersion in isopropyl alcohol (~0.42 mg mL^{-1}). The ball milling method has demonstrated good capability for large-scale production of graphene materials, however, the high-energy collision among the grinding medium introduces fragmentation as well as basal defects to exfoliated flakes.[24]

1.3.2 Liquid-phase sonication

Liquid-phase sonication was initially designed to exfoliate and disperse carbon nanotubes (or bundles).[35] In stable dispersions, the surface energies of dispersing solvents match that of the nanotubes. From this inspiration, Johnathan Coleman *et al* first reported the exfoliation of graphite in a range of organic solvents, for example, DMF and NMP.[36] The weak van der Waals interactions between adjacent graphene layers can be simply broken using a low power sonication bath. The concentration of dispersed graphene was measured using a combination of filtration, weighing and adsorption spectroscopy. The peak concentration appeared with solvent surface tension close to 40 N m^{-1}, which was translated to surface energy of 70 mJ m^{-2}. The experiment and thermodynamic modelling revealed that the energy balance for graphene flakes and dispersed solvents shall follow this equation:[37]

$$\frac{\Delta H_{mix}}{V_{mix}} \approx \frac{2}{T_{flake}}(\sqrt{E_s} - \sqrt{E_G})^2 \emptyset_G$$

where $\frac{\Delta H_{mix}}{V_{mix}}$ is the enthalpy of mixing per unit volume, T_{flake} is the thickness of nanoflake, E_s and E_G are the surface energies of solvent and graphene, respectively. $\emptyset_G$ is the dispersed graphene volume fraction.

Apparently, when E_s and E_G are close, the value of mixing enthalpy will be reduced and graphite exfoliation is more likely to happen. The calculated surface energy of graphene is ~68 mJ m^{-2}. For a successful exfoliation, the selection of proper solvents plays an important role. They shall be able to peel off the layers and stabilize them in dispersions to avoid re-aggregation. Table 1.1 shows the most commonly-used solvents with various surface tensions. Among them, NMP and other pyrrolidone-based solvents are very effective for graphite delamination. However, these high boiling point solvents are problematic for practical applications as they are difficult to remove. Besides single solvents, some binary mixtures like DMF/*n*-butyl alcohol,[38] H_2O/*t*-butyl alcohol,[39]H_2O/isopropyl alcohol (IPA),[40] have been studied. By carefully tuning the ratios of constituent solvents, the surface tension of mixture is able to match that of layered materials. For example, the addition of 10-30 wt% of *t*-butyl alcohol or IPA to water can greatly enhance the exfoliation yield of graphite and MoS_2. [39] The addition of surfactants into water is another strategy to control the mixed surface tension. For instance, graphite exfoliation in water containing sodium dodecylbenzenesulfonate (SDBS) leads to few-layer (< 5 layers, 40 %) and monolayer (~3 %) graphene.[41] An aqueous solution with 2 wt% sodium cholate exfoliates graphite into few-layer graphene dispersion with concentration exceeding 90 µg mL^{-1}.

[42] Importantly, binary systems reduce the safety hazards and cost but provide lower boiling points that are easy for post processing.

Table 1.1 Surface tension and boiling points of some common solvents (Data source: www.surface-tension.de; https://en.wikipedia.org/wiki/Surface-tension_values)

Solvents	**Surface Tension (N m^{-1})**	**Boiling Points (°C)**
N-methyl-2-pyrrolidone (NMP)	40.79	202
N,*N*-dimethylforamide (DMF)	37.10	153
Dimethyl sulfoxide (DMSO)	43.54	189
Propylene carbonate (PC)	41.10	242
Benzylbenzoate (BNBZ)	45.95	323
Diethylene glycol (DEG)	44.80	244
Ethylene glycol (EG)	47.70	197
Tetrahydrofuran (THF)	26.40	66
Isopropyl alcohol (IPA)	23.00	83
Chloroform	27.50	61
Toluene	28.40	111
Ethanol	22.10	78
Water	72.80	100

In a typical protocol (Fig. 1.5), the exfoliation process contains three main steps: (1) immerse bulk layered crystals or powders into a suitable liquid media; (2) subject the mixture to bath or tip sonication; (3) discard unexfoliated material and separate the resultant flakes from dispersion into diverse lateral sizes and number of layers by a density gradient centrifugation. Regarding the exfoliation mechanism, briefly, ultrasonic cavitation generates massive amount of bubbles, which distribute on the interfaces of layered compounds. Afterwards, the collapse of bubbles results in cavitation forces or shear forces that peel off thin layers from parent bulk material.[24]

Apart from graphite exfoliation, ultrasonic exfoliation is versatile for a variety of layered materials, for instance, BN,[43] transition metal oxides (TMOs),[2] $Ni(OH)_2$,[44] BP,[45] TMDs,[46] and even for some non-purified natural materials, including talcum powder, cat litter and beach sand.[47]

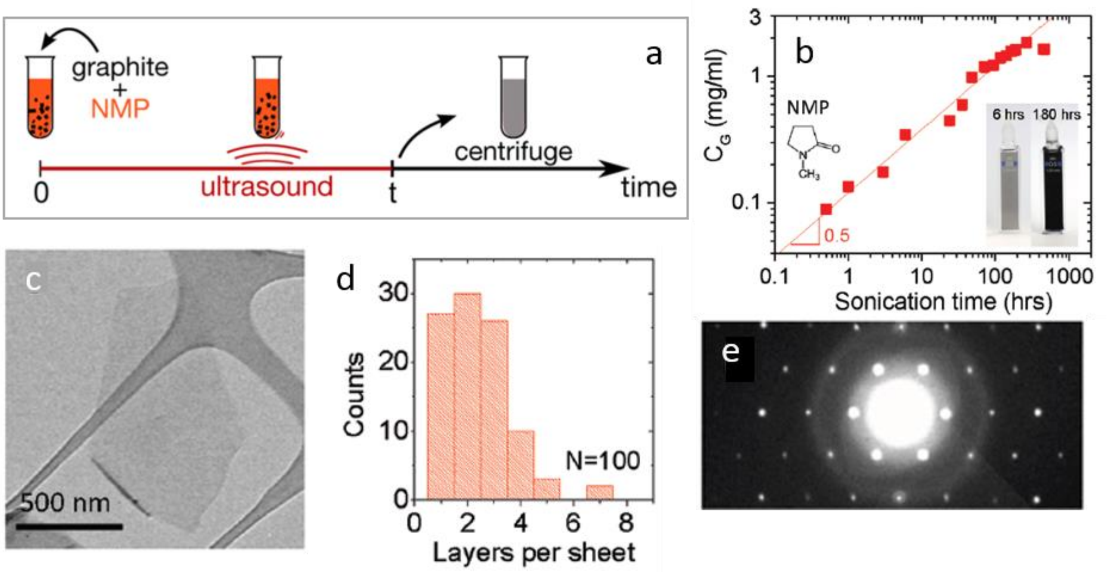

Figure 1.5 (a) Illustrative scheme of liquid-phase exfoliation.[48] (b) Concentration of graphene in NMP as a function of sonication time. (c) TEM image of graphene monolayer. (d) Thickness distribution of exfoliated graphene sheets. (e) Electron diffraction pattern of single-layer graphene.[37]

Liquid sonication is simple to use under ambient conditions and does not involve chemical reactions. It provides possible solution-processability while keeping the intrinsic properties of exfoliated flakes. The potential scalability is another considerable advantage, for instance, the throughput can be scaled up according to the mass of precursors and the dimension of reactors. However, the exfoliated products have poor uniformity in thickness, small fraction of large flakes and monolayers (ca. 1 wt%).[49] The exfoliation yield, calculated from the weight ratio of dispersed flakes to the starting materials, is also low (sub 1 %). By applying shear force (induced by rotor stator mixers), the exfoliation yield has been increased up to 3 % by recycling use of graphitic sediment.[50] However, the concentration of dispersed graphene remains limited (0.01 mg mL^{-1} in NMP after 30 min sonication).[49] Although higher concentration (0.5 mg mL^{-1}) can be achieved by long sonication (i.e. 300 h),[37] the sizes of exfoliated flakes are radically decreased to hundreds of nanometres, owing to ultrasonic fragmentation. Alternatively, the addition of organic molecules, e.g. arachidic acid and 1-phenyloctane, into the NMP-based sonication process (6 h) largely improves graphene concentration to 0.128 mg $mL^{-1}$and 0.1 mg mL^{-1} respectively. In contrast, bare NMP only stabilizes the dispersion with a concentration of up to 0.075 mg mL^{-1}.[51] Nonetheless, prolonged sonication may cause defects in the exfoliated flakes. As illustrated above, ultrasonic exfoliation relies on sonication-induced cavitation, which is a relatively harsh process that includes high local temperature (more than 1000 K) and high pressure (over thousand atm).[52] Defects appear mainly at the flake boundaries for short sonication time, while they will spread onto the basal plane for long-lasting agitation (e.g. over 2 hours).[48]

1.3.3 Chemical intercalation

Chemical intercalation is an old trick that mainly relies on the use of strong oxidants to expand graphite boundaries by covalent functionalization. The spontaneous intercalation of guest species enlarges the interlayer spacing thereby overcoming van der Waals interaction. Graphite oxide, an oxygen-rich graphite derivative, was firstly synthesized by Brodie and Staudenmaier in the late 19th century, using graphite powder and fuming nitric acid. The oxidation procedure was optimized by Hummers and Offeman in 1958, using potassium permanganate ($KMnO_4$), concentrated sulfuric acid (H_2SO_4) and sodium nitrate ($NaNO_3$) as oxidants:[53]

(1) $KMnO_4 + H_2SO_4 \rightarrow K^+ + MnO_3^+ + H_3O^+ + 3HSO_4^-$

(2) $MnO_3^+ + MnO_4^- \rightarrow Mn_2O_7$

Hummers' method is the most popular protocol to prepare graphene materials that can be scaled-up to mass production. Graphite oxide with oxygen-containing groups (such as epoxide, hydroxyl and carboxylic groups) can be exfoliated in water under mild sonication to give birth to graphene oxide (GO) with a high conversion yield (nearly 100 %) (Fig. 1.6). GO is highly hydrophilic and forms stable aqueous colloids through simple solution processes. Moreover, the heavily functionalized surface of GO offers opportunities for chemical modification by classic organic reactions.[54]

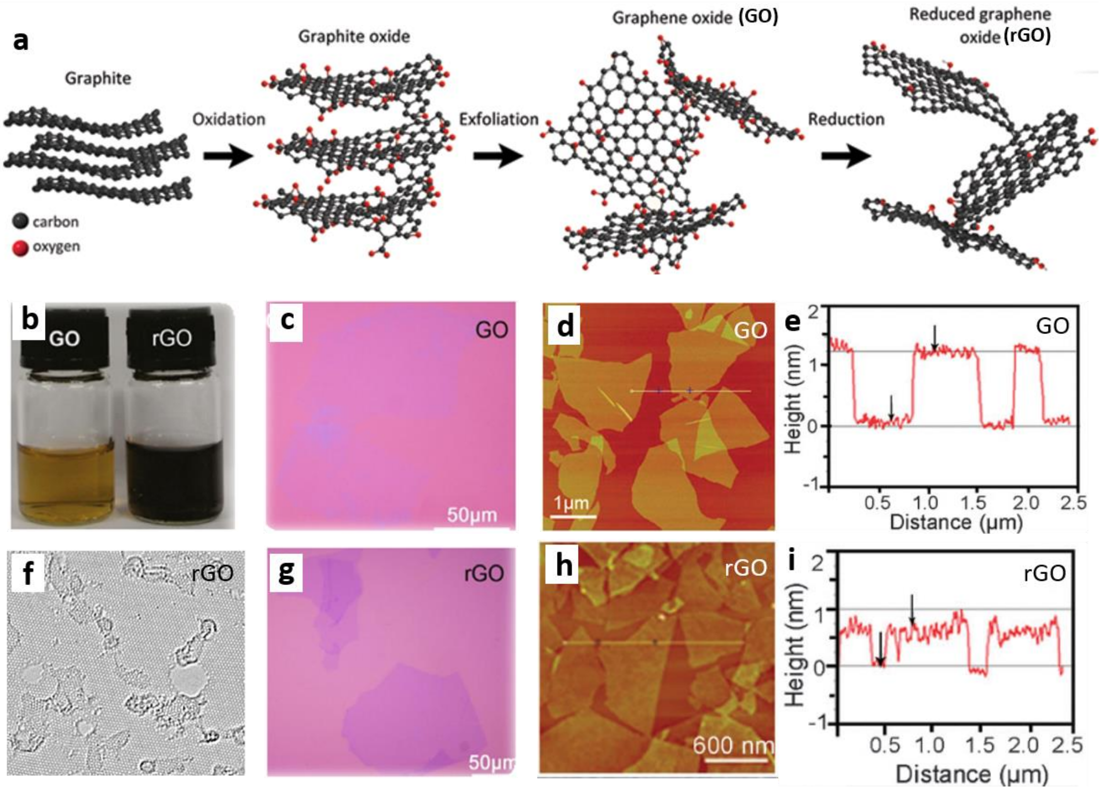

Figure 1.6 (a) The route of chemical intercalation, from graphite to reduced graphene oxide.[55] (b) Optical image of GO and rGO dispersion.[56] (c-e) Optical picture, AFM image and height profile of GO sheets.[57] (f) HR-TEM of a rGO sheet.[58] (g-i) Optical picture, [56] AFM image and height profile of GO sheets.[57]

Graphene oxide is considered as electric insulator owing to the disruption of conjugated graphitic network. In order to recover the conducting sp^2-bonded carbon atoms, substantial efforts have been devoted to eliminating oxygen groups by chemical, thermal, and electrochemical strategies over the past decades. Chemical reduction is usually performed in the presence of reducing agents including hydrazine,[59] sodium borohydride,[60] L-ascorbic acid,[57] hydroiodic acid,[61] sodium-liquid ammonia (Na-NH_3) solution,[62] etc, which produce reduced graphene oxide (rGO) with carbon to oxygen (C/O) ratio in the range of 8.6-22.5 and electric conductivity from 0.045 to 298 S cm^{-1}. Electrochemical reduction is mainly induced by the electron exchange between electrode and GO in an aqueous buffer solution, therefore does not need special chemical agent.[63] By controlling the pH values of the electrolyte, the C/O ratio of rGO reaches 23.9 and the conductivity of resulted rGO film is about 85 S cm^{-1}.[64] Thermal reduction is always conducted at high-temperature (> 300 °C) annealing in vacuum,[65] or under inert gas,[66] or in reducing atmosphere.[67] The thermal shock is effective to kick out the oxygen-containing groups by forming CO_2 and CO gases. The thermally converted rGO presents a C/O ratio higher than 13 and electric conductivity of 550 S cm^{-1} after treatment at 1100 °C.[66] Ultrahigh temperature (2850 °C) can further enhance the conductivity to 2210 (±60) S cm^{-1}.[68] Using a multistep reduction process, i.e. mild reduction at 300 °C for 1 h, followed by microwave irradiation (1000 W, 1-2 s), the quality of rGO has been greatly improved, with exceptional mobility values of > 1000 cm^2 V^{-1} s^{-1}.[69]

Although oxygen groups are relatively easy to remove, the defects caused by oxidation or reduction are difficult to heal by post-treatments. Thus, the synthesis of highly reducible GO is desirable. Based on a modified Hummers' method, a new form of graphene oxide (GO-*n*, or *oxo*-GO) was produced by prolonged oxidation time (16 h) at low temperature (< 10 °C). The oxo-additives protect the basal plane of graphene sheets from excessive oxidation. The *oxo*-GO under beam irradiation exhibits large-area intact sp^2 carbon framework.[70] After reduction by hydriodic/trifluoroacetic acid, the obtained rGO-*n* presents a Raman I_D/I_G ratio < 1.0, a charge-carrier mobility of 250 cm^2 V^{-1} s^{-1} for holes and 200 cm^2 V^{-1} s^{-1} for electrons.[71] In contrast, commonly known GO reduced under similar conditions has a large I_D/I_G ratio (> 1.0) and low mobility of 0.1-1cm^2 V^{-1} s^{-1}.[72]

1.3.4 Non-oxidative intercalation

Non-oxidative intercalation depends on diffusion of guest species into the interlayer spacing of layered materials but involves no chemical oxidation. The insertion of alkali metals (e.g. potassium) into graphite was realized by vapour diffusion under vacuum (110 °C) (Fig. 1.7). The resulted intercalated compound (KC_8) is a great precursor for defect-free graphene (~60 % are 1-2 layers).[73] When KC_8 reacts with tetrahydrofuran (THF), exfoliated graphene flakes can be dispersed in degassed water to form stable dispersion without using surfactants. The filtrated film from these dispersions presents a conductivity of 320 S cm^{-1}.[74] Through a similar vapour-phase intercalation process (35 °C in vacuum), the intercalation with iodine chloride (ICl) and iodine bromide (IBr) into graphite lead to solution dispersions enriched with bilayer and trilayer graphene. The flakes reveal outstanding hole mobility as high as ~400 $cm^2\ V^{-1}\ s^{-1}$.[75] At higher temperature (e.g. 380 °C), iron chloride was pushed into graphite structure, leading to few-layer graphene flakes after reacting with hydrogen peroxide.[76] When intercalated with Brønsted acids (e.g. phosphoric, dichloroacetic and alkylsulfonic acids) at room temperature, the exfoliation of graphite produces single-layer graphene with a yield of 53 %.[77]

Besides graphene synthesis, non-oxidative intercalation has been widely extended to fabricate many other 2D materials. For instance, on the basis of lithium intercalation from *n*-butyllithium in hexane and reacting the intercalated lithium with excessive water, MoS_2 and WS_2 were exfoliated into thin layers.[78] Controllable lithium intercalation has been achieved through monitoring galvanostatic discharge in assembled lithium-ion batteries.[79] Subsequent exfoliation in water or ethanol results in a series of high-quality 2D nanosheets, such as MoS_2, WS_2, TiS_2, TaS_2, few-layer BN, $NbSe_2$, WSe_2, Bi_2Te_3, et al.[80] The insertion of hydroxides into BN using molten salts peel off BN flakes from parent layered crystal.[81] Monolayer graphitic carbon nitride (g-C_3N_4) was produced by soaking inside concentrated sulfuric acid.[82] The intercalation of solvents (e.g. formamide) or large molecules (e.g. tetra-*n*-butylammonium hydroxide) as well as ion exchange are effective for the delamination of layered double hydroxide (LDHs).[83]

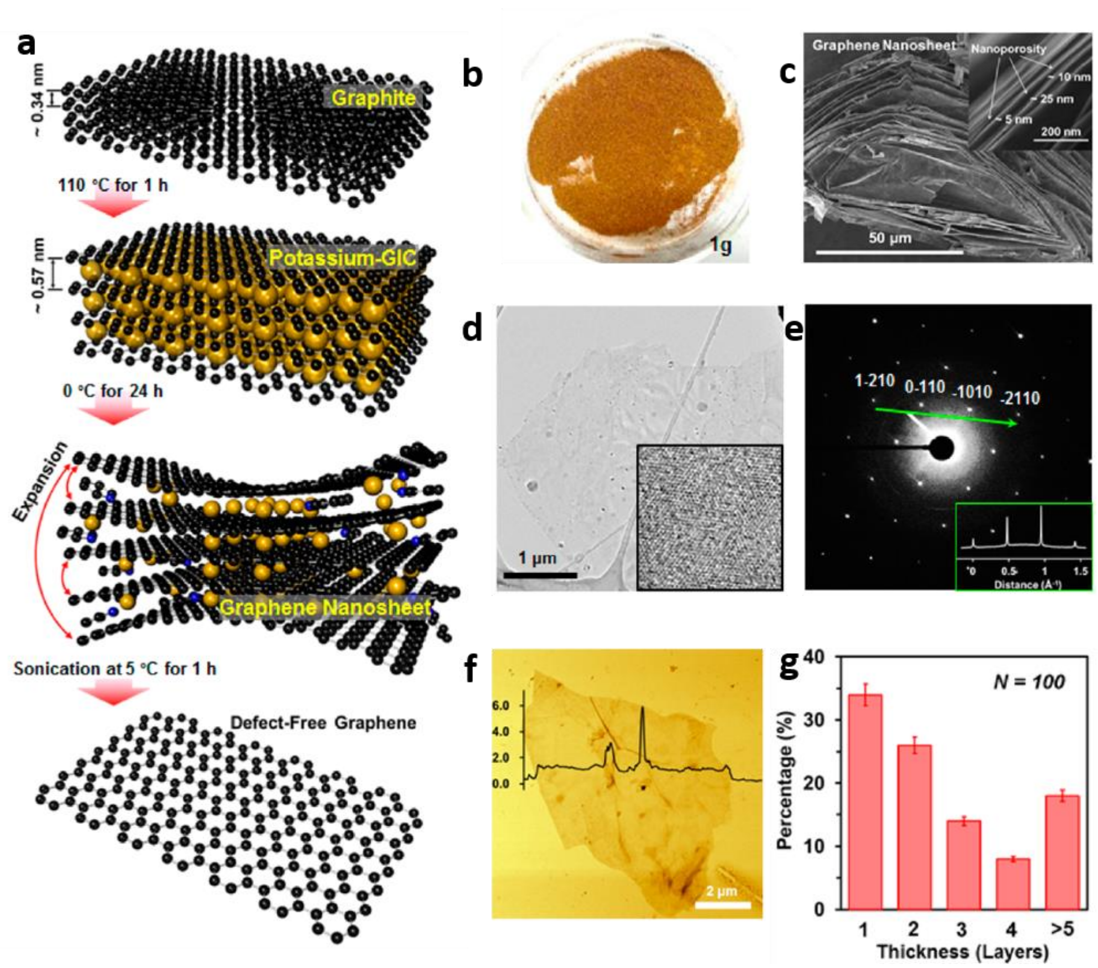

Figure 1.7 (a) The scheme of non-oxidative intercalation of potassium into graphite. (b) Optical image of KC_8 compounds. (c) SEM image of stacked graphene sheets. (d, e) TEM image of graphene sheet and its corresponding electron diffraction pattern. (f, g) Topological AFM image and the related thickness distribution.[73]

1.3.5 Electrochemical exfoliation

Electrochemical methods could be dated back to the 1980s, when they were investigated to prepare graphite intercalated compounds (GICs) by the intercalation of pure sulfuric acid into graphite interlayers.[84] Until recent years chemists were aware of using such straightforward routes for the synthesis of graphene sheets. In general, the electrochemical method involves a conductive liquid media and a current flow to drive structural expansion within graphitic precursors in form of rod, foil, flake or plate. The graphite electrode can be either positively or negatively charged, that allows the intercalation of anions and cations, respectively (Fig. 1.8).[85] Therefore, the exfoliation processes can be broadly classified into (1) anodic exfoliation in the mixture of water and ionic liquids, aqueous solution of inorganic salts or mineral acids; and (2) cathodic exfoliation in organic solvents (e.g. propylene carbonate, dimethyl sulfoxide) containing lithium or alkylammonium salts.[86] The intercalation of charged species usually combines with gas release, as a result of solvent electrolysis (or by post treatments), that further enlarges the interlayer distances and overcomes van der Waals interaction. In contrast to liquid-phase exfoliation or oxidative intercalation strategies, electrochemical methods offer great ease of operation as they are not equipment-intensive and are typically performed at ambient conditions. According to the control over electrolysis parameters, the synthesis process can be designed for the exfoliation of bulk materials and/or the functionalization of 2D flakes.[87] In addition, the electrochemical procedure runs relatively fast, which only takes several minutes to hours to produce materials with gram-scale quantity. Based on electrochemical cell engineering, the throughput can be further scaled up. The exfoliation process is eco-friendly and eliminates apparent pollution by recycling the use of electrolytes. In general, the electrolytes are crucial for the overall exfoliation process. Many research groups have made considerable progress toward exploring electrolytes for graphite exfoliation.

In aqueous solution, the mixture of sulfuric acid and potassium hydroxide (KOH) facilitates thin graphene layers with good quality.[88] The addition of KOH was believed to suppress the strong oxidation from sulfuric acid. The thickness of the exfoliated graphene (EG) sheets was less than 3 nm (more than 65 % of the sheets were thinner than 2 nm). However, the exfoliation yield was quite limited (5–8 %). Based on the variation of H_2SO_4 concentration and/or working bias during the electrochemical exfoliation, a higher yield of EG (~60 %) with graphene concentrations up to 1 mg mL^{-1} in DMF was achieved.[89] 80 % of EG flakes are 1 to 3 layers with a C/O ratio of 12.3. By adding glycine into dilute sulfuric acid, a glycine-bisulfate ionic complex was employed for anodic graphite exfoliation in which the formation of molecule nuclei by the polymerization of intercalated monomeric HSO_4^- and SO_4^{2-} ions played a key role, producing few-layer EG (2–5 layer) with a C/O ratio of 8.1.[90] The use of melamine additives in sulfuric acid generates graphene with high C/O ratio (26.2) and good uniformity (over 80 % are less than 3 layers).[91] Recently, sodium halides (NaCl, NaBr, NaI) were considered as effective media for high-quality graphene sheets with a C/O ratio of 16.7.[92] Nonetheless, structural degradation is a general problem for anodic exfoliated graphene due to the oxidation of water molecules by a large positive voltage.

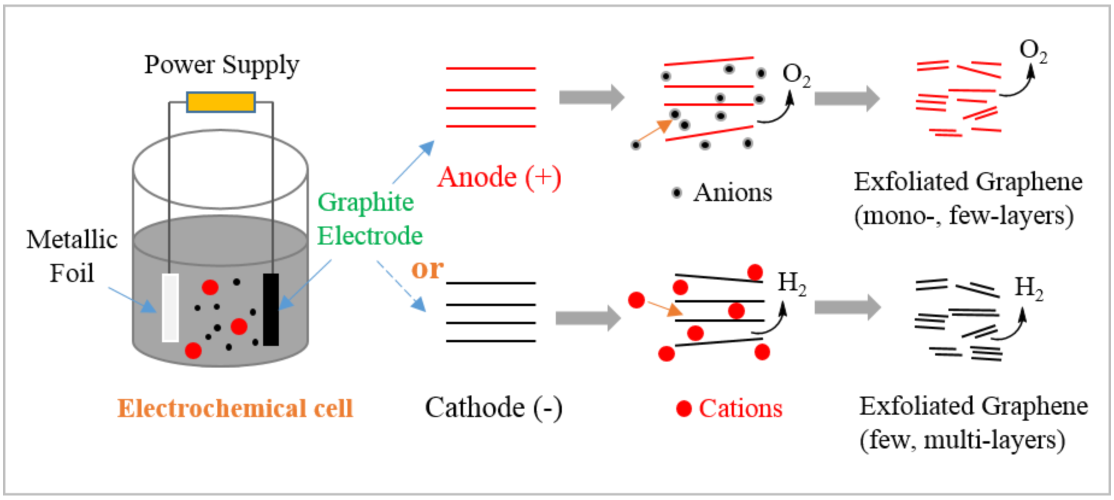

Figure 1.8 Electrochemical exfoliation of graphite at anode or cathode.

Many organic solvents including DMSO, acetonitrile, propylene carbonate and NMP have been explored in non-aqueous systems. Most of them own surface energies close to that of graphite. Cathodic exfoliation in a 1 M LiCl-DMSO electrolyte produces graphene with flake sizes ranging from 1 to 20 µm and thickness lower than 5 nm (5 % less than 0.9 nm).[93] The intercalation of tetra-alkyl-ammonium cations with various alkyl chains yields few-layer graphene (2–5 layers) with good quality that shows only 3 % oxygen increase compared to the graphite precursor. However, an additional sonication step is necessary to reach thorough exfoliation.[94] Apart from high-boiling solvents, other solvents with low-boiling points, such as acetonitrile, have become popular alternatives. By electrochemical co-insertion of perchlorate anions and acetonitrile molecules, graphite was intercalated and partially expanded at a voltage of +5 V for 30 min, then microwave irradiation was applied to complete the exfoliation process, yielding 61 % graphene by recycling the sediment.[95] Notably, 69 % of the graphene flakes were bilayers and 28 % of them were single layers with mean lateral dimensions of 1–2 μm. Generally, exfoliation in organic solvents preserves the structural quality of graphene but mainly with few-layer thickness due to inadequate ion intercalation.

1.4 Basic characterizations

Except mechanical cleavage, other exfoliation methods are generally performed in certain stabilizing liquids and/or the exfoliated flakes are readily dispersible in appropriate solvents, which can be further processed into nanostructured materials by spray coating, inkjet printing and freeze drying.[96] The concentration of dispersion (c, g L^{-1}) is determined by filtration or optical absorbance. The former one is calculated by the mass ratio of materials retained on the filter membrane to the total volume of dispersion. The latter one relies on UV-vis spectroscopy and Lambert-Beer Law ($A=\alpha cL$) where A is the measured absorbance, α is a wavelength-dependent absorptivity coefficient, L is the optical path length and c is the concentration of dispersion. UV-vis spectroscopy also reveals some information on the structure of the exfoliated flakes as the excitonic transitions of many materials are well documented. Besides, the yield of exfoliation is usually defined as the weight percentage of dispersed material to starting precursor.

1.4.1 Morphological investigation

Optical microscopy (OM) is a reliable technique to characterize the shapes and sizes of 2D flakes over a large region. It is very common in laboratories and convenient to use. To identify atomically thin flakes, it requires 2D flakes on silicon oxide substrate (i.e. Si/SiO_2) for good contrast. By using the interference effect, it enables a rapid estimation on the number of layers. In detail, accurate identification of single to few-layered flakes can be realized by measuring contrast difference from the brightness profile of colour pictures or grayscale images of the R, G, or B channel.[97] Fig. 1.9 shows that graphene flakes are clearly visible under optical microscope. It is worth noting that contrast values may vary with the thickness of SiO_2, the angle of illumination and the wavelength of light.[98] The standard charts plotted from contrast difference have been applied to read the thickness of graphene, MoS_2, WSe_2 and TaS_2.[97]

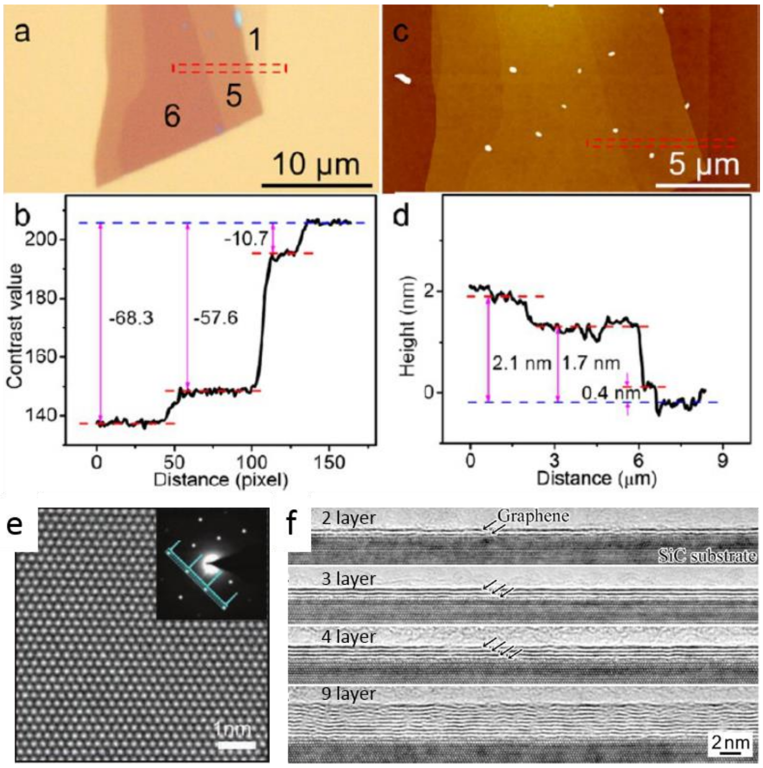

Fig 1.9 (a) Optical and (c) AFM height images of graphene flake on silicon substrate with 90 nm oxide layer. The contrast values obtained from (b) optical images have strong relations to the thickness values from (d) AFM images.[97] (e) HR-TEM image of single-layer graphene (insert: diffraction pattern).[99] (f) The dark lines at graphene edges under HR-TEM.[100]

Atomic force microscope (AFM) provides the morphology of 2D sheets and direct evidence of their crystal thickness (Fig. 1.9c, 1.9d). By applying tapping mode, the height profile clearly tells whether a given nanosheet is single, double or multiple layers. However, the height of monolayer flakes is sometimes dependent on their underlying substrates. For example, graphene flake on SiO_2 shows a height between 0.6 and 1.0 nm, whereas on mica the value is 0.4 nm.[101] Moreover, for solution-processed graphene flakes, due to the presence of residual solvents, the apparent heights are always over-estimated. Many groups notice that the measured heights of one layer of solution-processed flakes are around 1-2 nm, much greater than their theoretical thickness.[96] Based on the scanning in a large area, AFM is especially useful for statistical analysis that gives thickness distribution of exfoliated flakes.

Scanning electron microscope (SEM) is a conventional tool to capture images of 2D flakes. It takes advantage of a focused electron beam that interact with atoms in the sample. Compared to optical microscopy, SEM provides much higher resolution up to 1 nm. For conventional SEM measurement, the samples must be conductive, at least on the surface. Otherwise they should be coated with an ultrathin layer of electrically conducting materials (e.g. gold, platinum) prior to imaging. However, the irradiation by a high energy electron beam could cause damage to flakes especially for metastable samples. SEM has been widely used to visualize graphene and many other semiconducting TMD layers.

Transmission electron microscope (TEM) offers high resolution for nanoscale materials. TEM is ideal for ultrathin samples such as graphene. The selected-area electron diffraction (SAED) pattern can be used for the study of crystal structures (Fig 1.9e).[99] In addition, by counting the dark lines at the boundaries of flake, HR-TEM is able to directly identify the number of layers (Fig 1.9f).[100] However, for high-resolution images, high energy of electrons passing through the sample could result in single atom damage that limits the range of materials. In other words, low electron energy suppresses the damage but decreases the image resolution. The newly developed technologies, such as aberration-corrected TEM, become important choices for the studies of 2D materials.

1.4.2 Quality analysis

Raman spectroscopy is a fast and non-destructive method to study the physical properties of 2D materials. Since it is extremely sensitive to lattice vibration and intramolecular bonding, it provides the structural information under external perturbations, for example, strain, temperature, charge transfer, pressure on material systems with spectral-feature analysis at high resolution.[102] Raman spectrum of graphene displays three main bands, namely D band, G band and 2D band. D band originates from the breathing mode of sp^2 carbon and locates at ~1350 cm^{-1}.[103] It is very weak in high quality graphene (Fig. 1.10a). With an increasing density of defects or surface functionalities on graphene sheet, D band becomes more significant (Fig. 1.10b). Therefore, the intensity of D band is an indicator to estimate graphene quality. The G band is related to the in-plane vibrational mode of sp^2 system. Graphene usually shows up a sharp G band at 1587 cm^{-1}. The position may change according to the number of layers, following this equation:[102]

$$w = 1581.6 + \frac{11}{1 + n^{1.6}}$$

Where w is the position of G band in wavenumbers, n is the number of layers.

However, this estimation can be affected by environmental factors such as strain, doping, temperature, etc.

The 2D band (~2587 cm^{-1}) refers to an overtone of D band. It has strong intensity in pristine graphene when D band disappears. The intensity and shape of the 2D band have a relation with the thickness of graphene.[103] For example, the 2D band of monolayer flakes is symmetric and sharp, almost double height to that of G band. With the increasing number of layers, the intensity of 2D band becomes lower and the shape ultimately turns asymmetric in the spectrum of graphite.

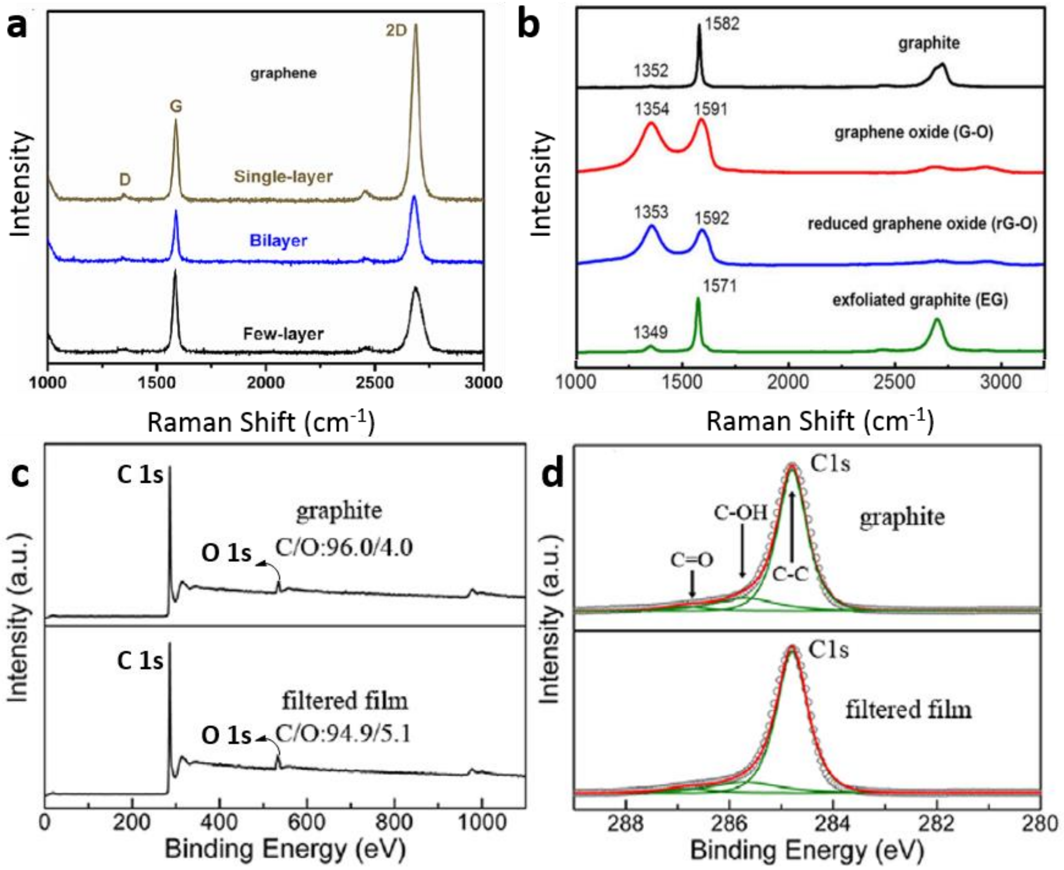

Figure 1.10 (a, b) Raman spectra of graphene, graphite and graphene derivatives.[104] (c, d) XPS spectra of graphite and filtrated graphene film. [105] (Source: 1.10a: https://quantumfrontiers.com/2013/09/06/graphene-gets-serious/)

X-ray photoelectron spectroscopy (XPS) is a universal technique to study the chemical components of the surfaces, especially useful to characterize the concentration and bonding of heteroatom dopants (such as oxygen, nitrogen, boron) in 2D materials. In particular, XPS is able to identify chemical states, atomic bonding configurations and the quantity of excited atoms. The working principles behind XPS measurements can be divided into three steps: [106] 1) an X-ray photon is excited and transfers the energy to a core electron; 2) the target atom emits a photoelectron, as a response, resulting in an empty core state; 3) the photoelectron shifts to the material surface and escapes into vacuum that is measured by an electron detector. In theory, graphene has only sp^2 carbons with binding energy at around 284.8 eV. However, it is usually contaminated with oxygen (e.g. C-O-C and O-C=O components) that shifts binding energy to ~286 eV and ~288.5 eV respectively (Fig. 1.10c-d).[105] According to the integrated area of C1s and O1s peaks, the elemental ratio between carbon and oxygen (C/O ratio) can be calculated. It is an important parameter to determine the quality of graphene. For example, GO is an electric insulator with a C/O ratio of around 2, after chemical reduction, its electric property can be improved and the C/O ratio of rGO reaches the range of 10-20.[107]

Field Effect Transistors (FETs) reveal the electronic properties of exfoliated materials. The standard FET structure consists of at least three electrodes, in which the source and drain electrodes are connected by a 2D flake and channel current is modulated by the electric field generated by the gate electrode. Underlying the 2D flake, a layer of dielectric barrier separates the gate electrode from the channel (Fig 1.11a). The gate control tunes the FET device with ON state (high current) or OFF state (low current). The ratio between high and low current (i.e. ON/OFF ratio) is a crucial parameter of digital switches. However, if the material does not have band gap, its FET devices cannot be switched off and the ON/OFF ratio is expected to be very low.[108] For example, pristine graphene demonstrates a poor ON/OFF ratio of ~7, due to its typical gapless band structure.[109] The creation of bandgaps through confinement, such as graphene nanoribbons with sub 10 nm width, leads to an improved ON/OFF ratio of ~100.[110] By contrast, monolayer MoS_2 shows a high ON/OFF ratio of 1×10^8 at room temperature thanks to its direct bandgap.[26]

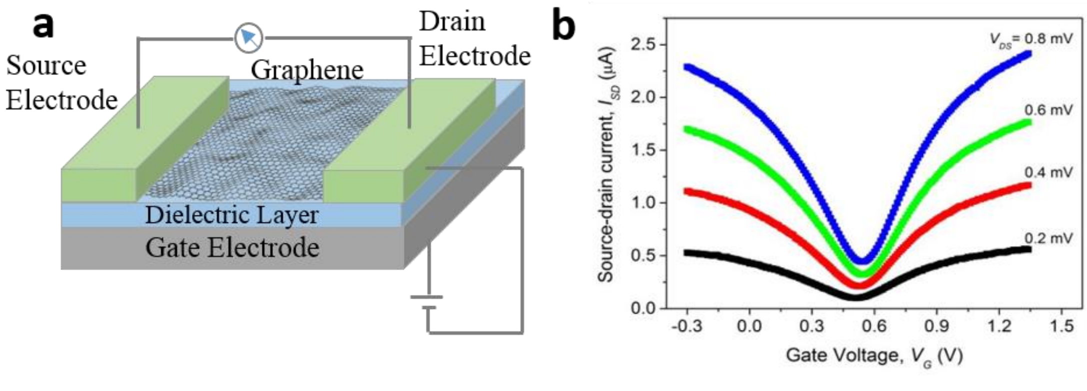

Figure 1.11 (a) Schematic structure of graphene FET device. (b) Transfer curves at different source-drain voltage (V_{DS} = 0.2, 0.4, 0.6 and 0.8 mV).[111]

Graphene FETs display a characteristic V-shape transfer curve (Fig 1.11b). The system without free carriers at T = 0 K and with Fermi level at the Dirac point is called intrinsic graphene, which has a completely filled valence band and an empty conduction band.[111] Chemical doping with heteroatoms fills the electrons into the conduction band that changes the transport features. By varying the external gate voltage, the carrier type in graphene switches between hole (p-type) and electron (n-type) when the Femi level goes across the Dirac point.[112] The hole mobility and electron mobility are respectively calculated from the fitted liner curves of hole and electron conduction region. Pristine graphene from mechanical exfoliation owns remarkable carrier mobility (> 20,000 cm^2 V^{-1} s^{-1}) for both holes and electrons.[113] Recently, graphene from chemical vapour deposition (CVD) shows an outstanding mobility of 350,000 cm^2 V^{-1} s^{-1}.[114] However, owing to the possible defects and residue oxygen moieties, rGOs generally have lower mobility values in a broad range from 1.8 to 1000 cm^2 V^{-1} s^{-1}, depending on the reduction methods.[69, 115]

1.5 The application of exfoliated materials

Transparent electrodes are dominated by indium tin oxide (ITO) and fluorine tin oxide (FTO). However, they have main drawbacks of poor chemical stability and limited mechanical properties. In contrast, graphene is an ideal alternative for transparent electrode (TE) owing to the combination with high optical transparency (~97.7 % for single-layer graphene) and low sheet resistance (35 Ω sq^{-1} at 90 % transmittance), which are also promising for optoelectronic devices such as solar cells and light-emitting diodes (LEDs).[116] Apart from the graphene film grown by the CVD method, other graphene materials exfoliated from wet-chemical methods are usually of small sizes but high scalability and low production cost. The deposition of such materials into a continuous and uniform film is critical towards the practical use of graphene-based transparent electrodes. In the past years, many techniques, including layer-by-layer assembly,[117] vacuum filtration,[118] spin coating[119], Langmuir-Blodgett assembly[120] and spray coating,[121] have been developed for GO film deposition. To obtain a conductive film, subsequent reduction process and/or modification techniques (e.g. chemical doping, integration with nanomaterials) are also necessary (Fig. 1.12a). A GO film by hydroiodic acid (HI) reduction followed by HNO_3 bath doping leads to 59 % transparency and a low sheet resistance of ~565 Ω sq^{-1}.[122] GO reduction with H_2 and integration with silver nanowires result in a hybrid film with high transmittance of 89 % and low resistance of 74±7 Ω sq^{-1}.[123] Recently, spray-coating of high-quality graphene from electrochemical exfoliation produces conductive films with 70 % transparency and 520 Ω sq^{-1} resistance.[124] This fabrication method avoids reduction and doping processes and is appealing for scalable production. Spin-coating of MXene ($Ti_3C_2T_x$) nanosheets from their colloidal dispersion results in the films with transmittance of 93 % and conductivity of ~5736 S cm^{-1}, ranking among the state-of-the-art for future transparent conductive electrodes.[125]

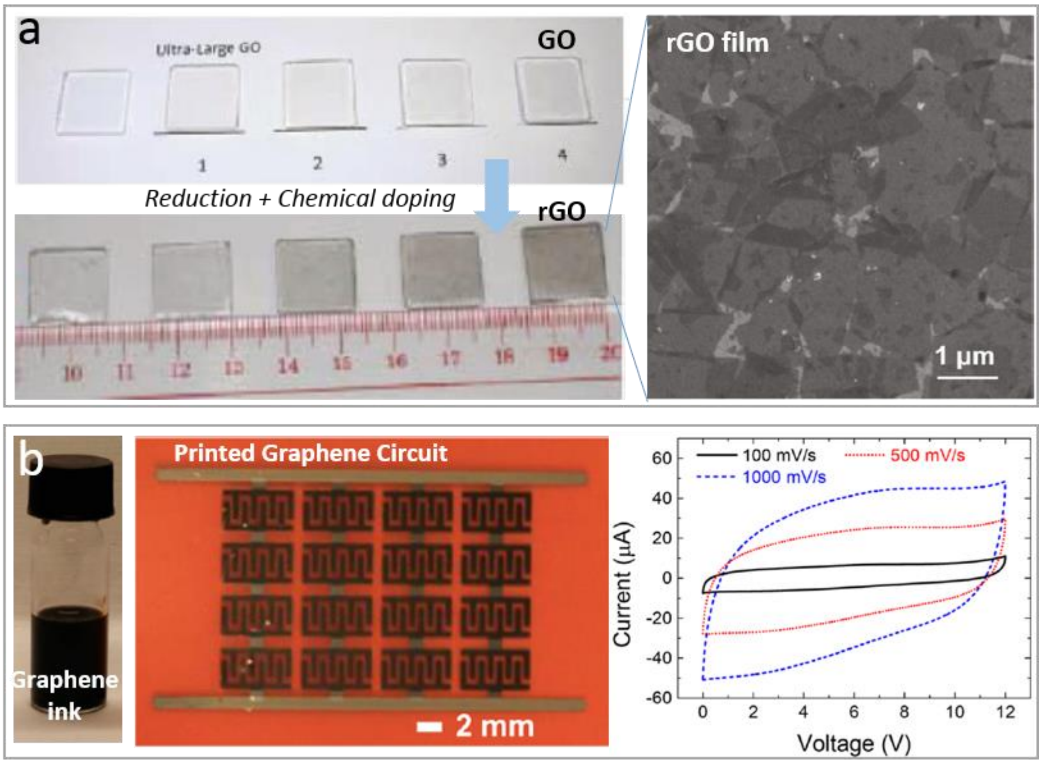

Figure 1.12 (a) Transparent electrodes based on reduced graphene oxide (inset: SEM image of electrode surface).[120] (b) Graphene ink (in DMF/cyclohexanone/terpineol, 2.3 mg mL^{-1}) and ink-printed graphene patterns for microsupercapacitors.[126]

Conductive inks are commonly made of noble metals (e.g. silver flakes), conductive polymers (e.g. poly(3,4-ethylenedioxythiophene) polystyrene sulfonate, PEDOT:PSS), or carbon nanomaterials (e.g. fullerenes, carbon nanotubes). The rise of printed electronics brings graphene into the field of printable inks. Inkjet printing of graphene is especially useful for the occasions where non-transparent but highly conductive patterns are desired. In terms of excellent electric properties, graphene inks hold the potential to replace metallic inks by reducing production costs and biological hazards.[127] For practical applications, the printable graphene ink shall possess suitable viscosity of approximately 10 cP and high concentration (> 1.0 mg mL^{-1}).[128] However, pristine graphene dispersion obtained from prolonged ultrasonication or shear mixing of graphite in DMF or NMP has quite low viscosity (< 2 cP) and low concentration (< 0.1 mg mL^{-1}). Despite graphene oxide offers great ease for ink formation, it is not the best choice due to the degradation of electronic properties. In this scenario, polymer binders (e.g. ethyl cellulose) and additives (e.g. terpineol) are introduced to tailor the ink characteristics (e.g. viscosity, rheology, evaporation kinetics).[129] Benefiting from a small amount of ethyl cellulose, the terpineol dispersion with liquid-exfoliated graphene has a high concentration of ~1 mg mL^{-1}, high viscosity of ~40 cP. The dispersion is stable for several weeks without agglomeration.[128] Similarly, electrochemically exfoliated graphene in such a system enables a high concentration of 2.3 mg mL^{-1}, which has been applied for full-inkjet-printing of microsupercapacitor (MSC) arrays with excellent charge voltage up to 12 V (Fig. 1.12b).[126] Direct patterning on paper substrates using an office printer and a hybrid graphene/PEDOT:PSS ink renders the fabrication of printable flexible MSCs with high areal capacitance of 5.4 mF cm^{-2}.[130] Beyond that, the inkjet printing of phosphorene and MoS_2 provides the opportunities for optoelectronics,[131] thin-film transistors,[132] and logic memory devices.[133]

Energy conversion and storage is the most popular area for the applications of exfoliated materials. In particular, the high specific surface area of graphene is freely accessible to electrolyte ions that is crucial for high-capacitance supercapacitors.

However, the surface area of graphene decreases rapidly with an increasing number of layers and therefore other active materials like polyaniline,[134] PEDOT:PSS,[135] carbon nanotubes[136] are combined with graphene sheets to improve performance and/or avoid restacking of graphene sheets. For example, alternating stacked graphene-conducting polymer films exhibit large areal capacitance of 368 mF cm^{-2} and volumetric capacitance of 736 F cm^{-3}.[137] The creation of 3D porous structures such as aerogels and foams is another strategy to maintain the surface area of graphene. All-solid-state supercapacitor based on ordered mesoporous carbon/graphene aerogel shows a specific capacitance of 44.3 F g^{-1}.[138] Furthermore, the doping with heteroatoms (e.g. boron, nitrogen) is able to introduce pseudocapacitance to graphene-based MSCs, facilitating ultrahigh volumetric capacitance of ~488 F cm^{-3}.[139]

Another promising field is the use of graphene as a supporting material in lithium ion batteries. Generally, graphene serves as flexible and conductive matrix to anchor active materials, which are typically deposited by in-situ growth or electrostatic attraction. A one-step electrochemical synthesis of graphene-based nanocomposites with Fe, Co and V oxides for lithium storage are presented with specific capacity as high as 894 mAh g^{-1} for an Fe_2O_3-loaded anode.[140] Graphene/polyaniline sandwich-structures with different inorganic nanoparticles demonstrate stable reversible capacities of more than 1300 mAh g^{-1} in combination with Si-NPs.[141] As a cathode material, sulfur has been deposited onto graphene using electrochemical process that outputs a capacity of 900 mAh g^{-1} after 60 cycles.[142] By adding a small amount of graphene (2.0 wt%) into commercial $LiFePO_4$ particles, the hybrid cathodes boost a capacity of 208 mAh g^{-1}, about 22 % above the theoretical value of $LiFePO_4$.[143]

1.6 Motivation and Objectives

As illustrated in the previous sections, the remarkable mechanical, electrical and optical properties render graphene an important material across a broad range of applications such as conductive films, printable electronics, energy conversion and storage devices. Although global research progress suggests a bright future of the graphene-based technologies, it is still premature to find their ways into everyday life products, due to the lack of efficient upscaling production protocols. The chemical oxidation methods, although have kilogram-scale production capability, are non-feasible routes to high-quality graphene as the subsequent reduction results in structural defects with variable types and levels, thus leading to low electrical conductivity. Other well-established approaches for high-quality graphene flakes or films, such as sonication-assisted liquid-phase exfoliation and chemical vapour deposition (CVD) growth, are limited by low production rates. Alternatively, electrochemical method becomes a plausible choice for the bulk-scale graphene production. Even though the exfoliated flakes have much better quality than that of reduced graphene oxide, they are still not comparable with pristine graphene flakes. Therefore, it is of great concern to develop reliable strategies to produce high quality graphene with high throughput.

In this thesis, we will mainly focus on the realization of excellent graphene quality as well as high production rates through electrochemical engineering in solutions. Moreover, we will extend this concept to prepare other semi-conducting materials beyond graphene (e.g. black phosphorus), which are of significant importance for the future-generation electronics.

(1) As for electrochemical exfoliation, electric current is the main driving force to facilitate ion diffusion in solutions and push the charged species into the graphite interlayers. Along with intercalation reactions, in aqueous electrolytes, for example, dilute sulfuric acid or inorganic sulfate solution, water oxidation is a serious side

reaction, which generates a large amount of reactive oxygen-containing radicals (e.g. ·OH and ·O), in turn corrode the graphite anode and introduce oxide groups. To suppress the oxidation reactions, in chapter 2, we demonstrate an efficient approach using reducing agents or radical scavengers during exfoliation process. The chemical reduction, by ascorbic acid or sodium borohydride, does not show apparent improvement on graphene quality. Notably, a stable radical, (2,2,6,6-tetra-methyl-piperidin-1-yl)oxyl (TEMPO) is effective to this end by capturing hydroxyl radicals. The exfoliation yield in this system is as high as 75 % and the exfoliated graphene exhibits large dimensional size (5-10 μm on average), outstanding electronic properties (405 $cm^2 V^{-1} s^{-1}$ for hole mobility), low defect density (I_D/I_G ratio < 0.1 in Raman spectra) and high C/O ratio (~25.3). Such high-quality graphene can be dispersible in DMF to prepare printable inks with high concentration (~6.0 mg mL^{-1}), which paves a way to the application of transparent conductive films and flexible supercapacitors.

(2) Although, using special additives into the electrolytes can prevent graphite from over-oxidation thus governing high-quality graphene, this method increases processing complexity and introduces additional cost. To kick out the oxide groups from exfoliated graphene, the manipulation of the applied potential is another rational strategy. Following this pathway, in Chapter 3, we present a new electrochemical system using alternating currents, instead of conventional direct current, to control the exfoliation process. By switching the polarity of working bias, graphite exfoliation occurs at anode and cathode simultaneously, based on the alternative intercalation of sulfate anions and quaternary ammonium cations, respectively. It produces graphene flakes with excellent yield over 75 % and high production rate exceeding 20 g h^{-1}. Thanks to the cathodic reduction, the produced graphene has low defect density (a C/O ratio of 21.2), leading to a high hole mobility of 430 $cm^2 V^{-1} s^{-1}$). As a cathode material, graphene-wrapped lithium iron phosphate delivers a high capacity of 167 mAh g^{-1} at 1 C rate after 500 cycles. The integration of graphene certainly contributes to the overall conductivity of hybrid material and improves its electrochemical

stability.

(3) Graphene does not have band gap, which limits its application in electronic devices. Beyond this, semi-conducting two-dimensional (2D) materials offer endless possibilities for the demonstration of improved or even entirely novel technologies. Especially, black phosphorus (BP) has intrinsic band gap with thickness dependence, which has not been discovered in any other 2D materials isolated to date. Therefore, the exfoliation of bulk BP into large-sized defect-free flakes has emerged as important research direction. Inspired by graphite exfoliation, in Chapter 4, we present an efficient exfoliation approach making use of non-aqueous electrolytes. When placing BP crystal as cathode, the intercalation of tetra-*n*-butyl-ammonium cations and solvated protons promotes high exfoliation yield up to 78 % and large BP flake with lateral dimension up to 20.6 µm. BP flakes have an average thickness of 3.7±1.3 nm, corresponding to 4-10 layers. They are free of lattice defects thus exhibit superior electronic properties. For instance, bottom-gate and bottom-contact field effect transistors based on few-layer BP flakes exhibit an excellent hole mobility of 252±18 $cm^2 V^{-1} s^{-1}$ and a remarkable on/off ratio of $(1.2\pm0.15)\times10^5$ at 143 K under vacuum, well comparable with those of mechanically exfoliated BP flakes.

1.7 References

[1] M. José-Yacamán, L. Rendón, J. Arenas, M. C. S. Puche, *Science* **1996**, *273*, 223-225.

[2] J. N. Coleman, M. Lotya, A. O'Neill, S. D. Bergin, P. J. King, U. Khan, K. Young, A. Gaucher, S. De, R. J. Smith, I. V. Shvets, S. K. Arora, G. Stanton, H.-Y. Kim, K. Lee, G. T. Kim, G. S. Duesberg, T. Hallam, J. J. Boland, J. J. Wang, J. F. Donegan, J. C. Grunlan, G. Moriarty, A. Shmeliov, R. J. Nicholls, J. M. Perkins, E. M. Grieveson, K. Theuwissen, D. W. McComb, P. D. Nellist, V. Nicolosi, *Science* **2011**, *331*, 568-571.

[3] R. Gusmão, Z. Sofer, M. Pumera, *Angew. Chem. Int. Ed.* **2017**, *56*, 8052-8072.

[4] M. Chhowalla, H. S. Shin, G. Eda, L.-J. Li, K. P. Loh, H. Zhang, *Nat. Chem.* **2013**, *5*, 263-275.

[5] V. Nicolosi, M. Chhowalla, M. G. Kanatzidis, M. S. Strano, J. N. Coleman, *Science*

2013, *340*.

[6] M. Naguib, V. N. Mochalin, M. W. Barsoum, Y. Gogotsi, *Adv. Mater.* **2014**, *26*, 992-1005.

[7] R. Woodward, E. Kelleher, *Appl. Sci.* **2015**, *5*, 1440.

[8] H. O. H. Churchill, P. Jarillo-Herrero, *Nat. Nanotechnol.* **2014**, *9*, 330-331.

[9] A. Burzlaff, S. Brethauer, C. Kasper, B.-O. Jackisch, T. Scheper, *Cytometry Part A* **2004**, *62A*, 65-69.

[10] F. Bonaccorso, Z. Sun, T. Hasan, A. C. Ferrari, *Nat. Photon.* **2010**, *4*, 611-622.

[11] C. Lee, X. Wei, J. W. Kysar, J. Hone, *Science* **2008**, *321*, 385-388.

[12] S. V. Morozov, K. S. Novoselov, M. I. Katsnelson, F. Schedin, D. C. Elias, J. A. Jaszczak, A. K. Geim, *Phys. Rev. Lett.* **2008**, *100*, 016602.

[13] M. D. Stoller, S. Park, Y. Zhu, J. An, R. S. Ruoff, *Nano Lett.* **2008**, *8*, 3498-3502.

[14] Y. Zhang, T.-T. Tang, C. Girit, Z. Hao, M. C. Martin, A. Zettl, M. F. Crommie, Y. R. Shen, F. Wang, *Nature* **2009**, *459*, 820.

[15] X. Li, X. Wang, L. Zhang, S. Lee, H. Dai, *Science* **2008**, *319*, 1229-1232.

[16] B. Dubertret, T. Heine, M. Terrones, *Acc. Chem. Res.* **2015**, *48*, 1-2.

[17] Y. L. Huang, Y. Chen, W. Zhang, S. Y. Quek, C.-H. Chen, L.-J. Li, W.-T. Hsu, W.-H. Chang, Y. J. Zheng, W. Chen, *Nat. Commun.* **2015**, *6*, 6298.

[18] A. Castellanos-Gomez, *J. Phys. Chem. Lett.* **2015**, *6*, 4280-4291.

[19] K. K. Kim, A. Hsu, X. Jia, S. M. Kim, Y. Shi, M. Hofmann, D. Nezich, J. F. Rodriguez-Nieva, M. Dresselhaus, T. Palacios, *Nano Lett.* **2011**, *12*, 161-166.

[20] F. Xia, H. Wang, D. Xiao, M. Dubey, A. Ramasubramaniam, *Nat. Photon.* **2014**, *8*, 899.

[21] M. Dresselhaus, G. Dresselhaus, *Adv. Phys.* **1981**, *30*, 139-326.

[22] R. Liu, D. Wu, X. Feng, K. Müllen, *J. Am. Chem. Soc.* **2011**, *133*, 15221-15223.

[23] aA. N. Obraztsov, *Nat. Nanotechnol.* **2009**, *4*, 212-213; bW. Zhang, J. K. Huang, C. H. Chen, Y. H. Chang, Y. J. Cheng, L. J. Li, *Adv. Mater.* **2013**, *25*, 3456-3461.

[24] M. Yi, Z. Shen, *J. Mater. Chem. A* **2015**, *3*, 11700-11715.

[25] K. S. Novoselov, A. K. Geim, S. V. Morozov, D. Jiang, Y. Zhang, S. V. Dubonos, I. V. Grigorieva, A. A. Firsov, *science* **2004**, *306*, 666-669.

[26] B. Radisavljevic, A. Radenovic, J. Brivio, V. Giacometti, A. Kis, *Nat. Nanotechnol.* **2011**, *6*, 147.

[27] Y. Cui, R. Xin, Z. Yu, Y. Pan, Z.-Y. Ong, X. Wei, J. Wang, H. Nan, Z. Ni, Y. Wu, T. Chen, Y. Shi, B. Wang, G. Zhang, Y.-W. Zhang, X. Wang, *Adv. Mater.* **2015**, *27*, 5230-5234.

[28] D.-M. Tang, D. G. Kvashnin, S. Najmaei, Y. Bando, K. Kimoto, P. Koskinen, P. M. Ajayan, B. I. Yakobson, P. B. Sorokin, J. Lou, D. Golberg, *Nat. Commun.* **2014**, *5*, 3631.

[29] V. Leon, M. Quintana, M. A. Herrero, J. L. G. Fierro, A. d. l. Hoz, M. Prato, E. Vazquez, *Chem. Commun.* **2011**, *47*, 10936-10938.

[30] W. Zhao, M. Fang, F. Wu, H. Wu, L. Wang, G. Chen, *J. Mater. Chem.* **2010**, *20*, 5817-5819.

[31] C. Teng, D. Xie, J. Wang, Z. Yang, G. Ren, Y. Zhu, *Adv. Funct. Mater.* **2017**, *27*, 1700240-n/a.

[32] V. León, A. M. Rodriguez, P. Prieto, M. Prato, E. Vázquez, *ACS Nano* **2014**, *8*, 563-571.

[33] I.-Y. Jeon, Y.-R. Shin, G.-J. Sohn, H.-J. Choi, S.-Y. Bae, J. Mahmood, S.-M. Jung, J.-M. Seo, M.-J. Kim, D. Wook Chang, L. Dai, J.-B. Baek, *Proc. Natl. Acad. Sci. U. S. A.* **2012**, *109*, 5588-5593.

[34] D. Lee, B. Lee, K. H. Park, H. J. Ryu, S. Jeon, S. H. Hong, *Nano Lett.* **2015**, *15*, 1238-1244.

[35] W. Huang, Y. Lin, S. Taylor, J. Gaillard, A. M. Rao, Y.-P. Sun, *Nano Lett.* **2002**, *2*, 231-234.

[36] J. N. Coleman, *Adv. Funct. Mater.* **2009**, *19*, 3680-3695.

[37] J. N. Coleman, *Acc. Chem. Res.* **2013**, *46*, 14-22.

[38] J. Chen, W. Shi, D. Fang, T. Wang, J. Huang, Q. Li, M. Jiang, L. Liu, Q. Li, L. Dong, Q. Wang, C. Xiong, *Carbon* **2015**, *94*, 405-411.

[39] U. Halim, C. R. Zheng, Y. Chen, Z. Lin, S. Jiang, R. Cheng, Y. Huang, X. Duan, *Nat. Commun.* **2013**, *4*, 2213.

[40] M. Yi, Z. Shen, S. Ma, X. Zhang, *J. Nanopart. Res.* **2012**, *14*, 1003.

[41] M. Lotya, Y. Hernandez, P. J. King, R. J. Smith, V. Nicolosi, L. S. Karlsson, F. M. Blighe, S. De, Z. Wang, I. T. McGovern, G. S. Duesberg, J. N. Coleman, *J. Am. Chem. Soc.* **2009**, *131*, 3611-3620.

[42] A. A. Green, M. C. Hersam, *Nano Lett.* **2009**, *9*, 4031-4036.

[43] K.-G. Zhou, N.-N. Mao, H.-X. Wang, Y. Peng, H.-L. Zhang, *Angew. Chem. Int. Ed.* **2011**, *50*, 10839-10842.

[44] S. Ida, D. Shiga, M. Koinuma, Y. Matsumoto, *J. Am. Chem. Soc.* **2008**, *130*, 14038-14039.

[45] Z. Guo, H. Zhang, S. Lu, Z. Wang, S. Tang, J. Shao, Z. Sun, H. Xie, H. Wang, X.-F. Yu, P. K. Chu, *Adv. Funct. Mater.* **2015**, *25*, 6996-7002.

[46] R. J. Smith, P. J. King, M. Lotya, C. Wirtz, U. Khan, S. De, A. O'Neill, G. S. Duesberg, J. C. Grunlan, G. Moriarty, J. Chen, J. Wang, A. I. Minett, V. Nicolosi, J. N. Coleman, *Adv. Mater.* **2011**, *23*, 3944-3948.

[47] H. Andrew, B. B. John, G. Ian, G. K. Adam, M. S. Beata, M. Ghulam, T. Andrew, J. L. David, O. B. Paul, N. C. Jonathan, *2D Mater.* **2017**, *4*, 025054.

[48] M. V. Bracamonte, G. I. Lacconi, S. E. Urreta, L. E. F. Foa Torres, *J. Phys. Chem. C* **2014**, *118*, 15455-15459.

[49] Y. Hernandez, V. Nicolosi, M. Lotya, F. M. Blighe, Z. Sun, S. De, I. T. McGovern, B. Holland, M. Byrne, Y. K. Gun'Ko, J. J. Boland, P. Niraj, G. Duesberg, S. Krishnamurthy, R. Goodhue, J. Hutchison, V. Scardaci, A. C. Ferrari, J. N. Coleman, *Nat. Nanotechnol.* **2008**, *3*, 563-568.

[50] K. R. Paton, E. Varrla, C. Backes, R. J. Smith, U. Khan, A. O’Neill, C. Boland, M. Lotya, O. M. Istrate, P. King, T. Higgins, S. Barwich, P. May, P. Puczkarski, I. Ahmed, M. Moebius, H. Pettersson, E. Long, J. Coelho, S. E. O’Brien, E. K. McGuire, B. M. Sanchez, G. S. Duesberg, N. McEvoy, T. J. Pennycook, C. Downing, A. Crossley, V. Nicolosi, J. N. Coleman, *Nat Mater* **2014**, *13*, 624-630.

[51] A. Ciesielski, S. Haar, M. El Gemayel, H. Yang, J. Clough, G. Melinte, M. Gobbi, E. Orgiu, M. V. Nardi, G. Ligorio, V. Palermo, N. Koch, O. Ersen, C. Casiraghi, P. Samorì, *Angew. Chem. Int. Ed.* **2014**, *53*, 10355-10361.

[52] W. B. McNamara, Y. T. Didenko, K. S. Suslick, *Nature* **1999**, *401*, 772-775.

[53] W. S. Hummers, R. E. Offeman, *J. Am. Chem. Soc.* **1958**, *80*, 1339-1339.

[54] D. R. Dreyer, A. D. Todd, C. W. Bielawski, *Chem. Soc. Rev.* **2014**, *43*, 5288-5301.

[55] E. J. C. Amieva, J. López-Barroso, A. L. Martínez-Hernández, C. Velasco-Santos, in *Recent Advances in Graphene Research* (Ed.: P. K. Nayak), InTech, Rijeka, **2016**, p. Ch. 12.

[56] S. Pei, H.-M. Cheng, *Carbon* **2012**, *50*, 3210-3228.

[57] J. Zhang, H. Yang, G. Shen, P. Cheng, J. Zhang, S. Guo, *Chem. Commun.* **2010**, *46*, 1112-1114.

[58] C. Gómez-Navarro, J. C. Meyer, R. S. Sundaram, A. Chuvilin, S. Kurasch, M. Burghard, K. Kern, U. Kaiser, *Nano Lett.* **2010**, *10*, 1144-1148.

[59] S. Stankovich, D. A. Dikin, R. D. Piner, K. A. Kohlhaas, A. Kleinhammes, Y. Jia, Y. Wu, S. T. Nguyen, R. S. Ruoff, *Carbon* **2007**, *45*, 1558-1565.

[60] D. Yang, A. Velamakanni, G. Bozoklu, S. Park, M. Stoller, R. D. Piner, S. Stankovich, I. Jung, D. A. Field, C. A. Ventrice, R. S. Ruoff, *Carbon* **2009**, *47*, 145-152.

[61] S. Pei, J. Zhao, J. Du, W. Ren, H.-M. Cheng, *Carbon* **2010**, *48*, 4466-4474.

[62] H. Feng, R. Cheng, X. Zhao, X. Duan, J. Li, *Nat. Commun.* **2013**, *4*, 1539.

[63] X. Wang, I. Kholmanov, H. Chou, R. S. Ruoff, *ACS Nano* **2015**, *9*, 8737-8743.

[64] M. Zhou, Y. Wang, Y. Zhai, J. Zhai, W. Ren, F. Wang, S. Dong, *Chem. Eur. J.* **2009**, *15*, 6116-6120.

[65] H. A. Becerril, J. Mao, Z. Liu, R. M. Stoltenberg, Z. Bao, Y. Chen, *ACS Nano* **2008**, *2*, 463-470.

[66] X. Wang, L. Zhi, K. Müllen, *Nano Lett.* **2008**, *8*, 323-327.

[67] X. Li, H. Wang, J. T. Robinson, H. Sanchez, G. Diankov, H. Dai, *J. Am. Chem. Soc.* **2009**, *131*, 15939-15944.

[68] G. Xin, T. Yao, H. Sun, S. M. Scott, D. Shao, G. Wang, J. Lian, *Science* **2015**, *349*, 1083-1087.

[69] D. Voiry, J. Yang, J. Kupferberg, R. Fullon, C. Lee, H. Y. Jeong, H. S. Shin, M. Chhowalla, *Science* **2016**, *353*, 1413-1416.

[70] B. Butz, C. Dolle, C. E. Halbig, E. Spiecker, S. Eigler, *Angew. Chem. Int. Ed.* **2016**, *55*, 15771-15774.

[71] S. Eigler, M. Enzelberger-Heim, S. Grimm, P. Hofmann, W. Kroener, A. Geworski, C. Dotzer, M. Röckert, J. Xiao, C. Papp, O. Lytken, H.-P. Steinrück, P. Müller, A. Hirsch, *Adv. Mater.* **2013**, *25*, 3583-3587.

[72] C. Gómez-Navarro, R. T. Weitz, A. M. Bittner, M. Scolari, A. Mews, M. Burghard, K. Kern, *Nano Lett.* **2007**, *7*, 3499-3503.

[73] K. H. Park, D. Lee, J. Kim, J. Song, Y. M. Lee, H.-T. Kim, J.-K. Park, *Nano Lett.* **2014**, *14*, 4306-4313.

[74] G. Bepete, E. Anglaret, L. Ortolani, V. Morandi, K. Huang, A. Pénicaud, C. Drummond, *Nat. Chem.* **2017**, *9*, 347-352.

[75] C.-J. Shih, A. Vijayaraghavan, R. Krishnan, R. Sharma, J.-H. Han, M.-H. Ham, Z. Jin, S. Lin, G. Paulus, N. Forest Reuel, Q. H. Wang, D. Blankschtein, M. S Strano, *Nat. Nanotechnol.* **2011**, *6*, 439-445.

[76] X. Geng, Y. Guo, D. Li, W. Li, C. Zhu, X. Wei, M. Chen, S. Gao, S. Qiu, Y. Gong, L. Wu, M. Long, M. Sun, G. Pan, L. Liu, *Sci. Rep.* **2013**, *3*, 1134.

[77] N. I. Kovtyukhova, Y. Wang, A. Berkdemir, R. Cruz-Silva, M. Terrones, V. H. Crespi, T. E. Mallouk, *Nat. Chem.* **2014**, *6*, 957-963.

[78] H. S. S. Ramakrishna Matte, A. Gomathi, A. K. Manna, D. J. Late, R. Datta, S. K. Pati, C. N. R. Rao, *Angew. Chem. Int. Ed.* **2010**, *49*, 4059-4062.

[79] Z. Zeng, Z. Yin, X. Huang, H. Li, Q. He, G. Lu, F. Boey, H. Zhang, *Angew. Chem. Int. Ed.* **2011**, *50*, 11093-11097.

[80] Z. Zeng, T. Sun, J. Zhu, X. Huang, Z. Yin, G. Lu, Z. Fan, Q. Yan, H. H. Hng, H. Zhang, *Angew. Chem. Int. Ed.* **2012**, *51*, 9052-9056.

[81] X. Li, X. Hao, M. Zhao, Y. Wu, J. Yang, Y. Tian, G. Qian, *Adv. Mater.* **2013**, *25*, 2200-2204.

[82] J. Xu, L. Zhang, R. Shi, Y. Zhu, *J. Mater. Chem. A* **2013**, *1*, 14766-14772.

[83] Q. Wang, D. O’Hare, *Chem. Rev.* **2012**, *112*, 4124-4155.

[84] H. Shioyama, R. Fujii, *Carbon* **1987**, *25*, 771-774.

[85] C. T. J. Low, F. C. Walsh, M. H. Chakrabarti, M. A. Hashim, M. A. Hussain, *Carbon* **2013**, *54*, 1-21.

[86] K. Parvez, S. Yang, X. Feng, K. Müllen, *Synth. Met.* **2015**, *210*, 123-132.

[87] S. Yang, M. R. Lohe, K. Müllen, X. Feng, *Adv. Mater.* **2016**, *28*, 6213-6221.

[88] C.-Y. Su, A.-Y. Lu, Y. Xu, F.-R. Chen, A. N. Khlobystov, L.-J. Li, *ACS Nano* **2011**, *5*, 2332-2339.

[89] K. Parvez, R. Li, S. R. Puniredd, Y. Hernandez, F. Hinkel, S. Wang, X. Feng, K. Müllen, *ACS Nano* **2013**, *7*, 3598-3606.

[90] K. S. Rao, J. Sentilnathan, H.-W. Cho, J.-J. Wu, M. Yoshimura, *Adv. Funct. Mater.* **2015**, *25*, 298-305.

[91] C.-H. Chen, S.-W. Yang, M.-C. Chuang, W.-Y. Woon, C.-Y. Su, *Nanoscale* **2015**, *7*, 15362-15373.

[92] J. M. Munuera, J. I. Paredes, M. Enterría, A. Pagán, S. Villar-Rodil, M. F. R. Pereira, J. I. Martins, J. L. Figueiredo, J. L. Cenis, A. Martínez-Alonso, J. M. D. Tascón, *ACS Appl. Mater. Interfaces* **2017**, *9*, 24085-24099.

[93] A. M. Abdelkader, I. A. Kinloch, R. A. W. Dryfe, *ACS Appl. Mater. Interfaces* **2014**, *6*, 1632-1639.

[94] A. J. Cooper, N. R. Wilson, I. A. Kinloch, R. A. W. Dryfe, *Carbon* **2014**, *66*, 340-350.

[95] Z. Y. Xia, G. Giambastiani, C. Christodoulou, M. V. Nardi, N. Koch, E. Treossi, V. Bellani, S. Pezzini, F. Corticelli, V. Morandi, A. Zanelli, V. Palermo, *ChemPlusChem* **2014**, *79*, 439-446.

[96] C. Backes, T. M. Higgins, A. Kelly, C. Boland, A. Harvey, D. Hanlon, J. N. Coleman, *Chem. Mater.* **2017**, *29*, 243-255.

[97] H. Li, J. Wu, X. Huang, G. Lu, J. Yang, X. Lu, Q. Xiong, H. Zhang, *ACS Nano* **2013**, *7*, 10344-10353.

[98] P. Blake, E. W. Hill, A. H. C. Neto, K. S. Novoselov, D. Jiang, R. Yang, T. J. Booth, A. K. Geim, *Appl. Phys. Lett.* **2007**, *91*, 063124.

[99] D. G. Matei, N.-E. Weber, S. Kurasch, S. Wundrack, M. Woszczyna, M. Grothe, T. Weimann, F. Ahlers, R. Stosch, U. Kaiser, A. Turchanin, *Adv. Mater.* **2013**, *25*, 4146-4151.

[100] W. Norimatsu, M. Kusunoki, *Chem. Phys. Lett.* **2009**, *468*, 52-56.

[101] C. Vallés, C. Drummond, H. Saadaoui, C. A. Furtado, M. He, O. Roubeau, L. Ortolani, M. Monthioux, A. Pénicaud, *J. Am. Chem. Soc.* **2008**, *130*, 15802-15804.

[102] H. Wang, Y. Wang, X. Cao, M. Feng, G. Lan, *J. Raman Spectrosc.* **2009**, *40*, 1791-1796.

[103] A. C. Ferrari, D. M. Basko, *Nat. Nanotechnol.* **2013**, *8*, 235.

[104] H. J. Kim, S.-M. Lee, Y.-S. Oh, Y.-H. Yang, Y. S. Lim, D. H. Yoon, C. Lee, J.-Y. Kim, R. S. Ruoff, *Sci. Rep.* **2014**, *4*, 5176.

[105] N. G. Shang, P. Papakonstantinou, S. Sharma, G. Lubarsky, M. Li, D. W. McNeill, A. J. Quinn, W. Zhou, R. Blackley, *Chem. Commun.* **2012**, *48*, 1877-1879.

[106] T. Susi, T. Pichler, P. Ayala, *Beilstein J. Nanotechnol.* **2015**, *6*, 177-192.

[107] K. N. Kudin, B. Ozbas, H. C. Schniepp, R. K. Prud'homme, I. A. Aksay, R. Car, *Nano Lett.* **2008**, *8*, 36-41.

[108] R. Dharmendar, F. R. Leonard, D. C. Gary, K. B. Sanjay, *J. Phys. D: Appl. Phys.* **2011**, *44*, 313001.

[109] I. Meric, M. Y. Han, A. F. Young, B. Ozyilmaz, P. Kim, K. L. Shepard, *Nat. Nanotechnol.* **2008**, *3*, 654.

[110] R. M. Jacobberger, B. Kiraly, M. Fortin-Deschenes, P. L. Levesque, K. M. McElhinny, G. J. Brady, R. Rojas Delgado, S. Singha Roy, A. Mannix, M. G. Lagally, P. G. Evans, P. Desjardins, R. Martel, M. C. Hersam, N. P. Guisinger, M. S. Arnold, *Nat. Commun.* **2015**, *6*, 8006.

[111] N. C. S. Vieira, J. Borme, J. G. Machado, F. Cerqueira, P. P. Freitas, V. Zucolotto, N. M. R. Peres, P. Alpuim, *J. Phys. Condens. Matter* **2016**, *28*, 085302.

[112] T. Feng, D. Xie, Y. Lin, H. Tian, H. Zhao, T. Ren, H. Zhu, *Appl. Phys. Lett.* **2012**, *101*, 253505.

[113] K. I. Bolotin, K. J. Sikes, Z. Jiang, M. Klima, G. Fudenberg, J. Hone, P. Kim, H. L. Stormer, *Solid State Commun.* **2008**, *146*, 351-355.

[114] L. Banszerus, M. Schmitz, S. Engels, J. Dauber, M. Oellers, F. Haupt, K. Watanabe, T. Taniguchi, B. Beschoten, C. Stampfer, *Sci. Adv.* **2015**, *1*, e1500222.

[115] J. Yang, J.-W. Kim, H. S. Shin, *Adv. Mater.* **2012**, *24*, 2299-2303.

[116] Y. Xu, J. Liu, *Small* **2016**, *12*, 1400-1419.

[117] B. H. R. Suryanto, X. Lu, C. Zhao, *J. Mater. Chem. A* **2013**, *1*, 12726-12731.

[118] J. Geng, H.-T. Jung, *J. Phys. Chem. C* **2010**, *114*, 8227-8234.

[119] I. N. Kholmanov, S. H. Domingues, H. Chou, X. Wang, C. Tan, J.-Y. Kim, H. Li, R. Piner, A. J. G. Zarbin, R. S. Ruoff, *ACS Nano* **2013**, *7*, 1811-1816.

[120] Q. Zheng, W. H. Ip, X. Lin, N. Yousefi, K. K. Yeung, Z. Li, J.-K. Kim, *ACS Nano* **2011**, *5*, 6039-6051.

[121] Z. Liu, K. Parvez, R. Li, R. Dong, X. Feng, K. Müllen, *Adv. Mater.* **2015**, *27*, 669-675.

[122] D. Konios, C. Petridis, G. Kakavelakis, M. Sygletou, K. Savva, E. Stratakis, E. Kymakis, *Adv. Funct. Mater.* **2015**, *25*, 2213-2221.

[123] S. H. Domingues, I. N. Kholmanov, T. Kim, J. Kim, C. Tan, H. Chou, Z. A. Alieva, R. Piner, A. J. G. Zarbin, R. S. Ruoff, *Carbon* **2013**, *63*, 454-459.

[124] A. G. Ricciardulli, S. Yang, X. Feng, P. W. M. Blom, *ACS Appl. Mater. Interfaces* **2017**, *9*, 25412-25417.

[125] C. Zhang, B. Anasori, A. Seral-Ascaso, S.-H. Park, N. McEvoy, A. Shmeliov, G. S. Duesberg, J. N. Coleman, Y. Gogotsi, V. Nicolosi, *Adv. Mater.* **2017**, *29*, 1702678-n/a.

[126] J. Li, S. Sollami Delekta, P. Zhang, S. Yang, M. R. Lohe, X. Zhuang, X. Feng, M. Östling, *ACS Nano* **2017**, *11*, 8249-8256.

[127] K. Arapov, R. Abbel, G. de With, H. Friedrich, *Faraday Discuss.* **2014**, *173*, 323-336.

[128] J. Li, F. Ye, S. Vaziri, M. Muhammed, M. C. Lemme, M. Östling, *Adv. Mater.* **2013**, *25*, 3985-3992.

[129] A. Capasso, A. E. Del Rio Castillo, H. Sun, A. Ansaldo, V. Pellegrini, F. Bonaccorso, *Solid State Commun.* **2015**, *224*, 53-63.

[130] Z. Liu, Z.-S. Wu, S. Yang, R. Dong, X. Feng, K. Müllen, *Adv. Mater.* **2016**, *28*, 2217-2222.

[131] G. Hu, T. Albrow-Owen, X. Jin, A. Ali, Y. Hu, R. C. T. Howe, K. Shehzad, Z. Yang, X. Zhu, R. I. Woodward, T.-C. Wu, H. Jussila, J.-B. Wu, P. Peng, P.-H. Tan, Z. Sun, E. J. R. Kelleher, M. Zhang, Y. Xu, T. Hasan, *Nat. Commun.* **2017**, *8*, 278.

[132] T.-Y. Kim, J. Ha, K. Cho, J. Pak, J. Seo, J. Park, J.-K. Kim, S. Chung, Y. Hong, T. Lee, *ACS Nano* **2017**, *11*, 10273-10280.

[133] D. McManus, S. Vranic, F. Withers, V. Sanchez-Romaguera, M. Macucci, H. Yang, R. Sorrentino, K. Parvez, S.-K. Son, G. Iannaccone, K. Kostarelos, G. Fiori, C.

Casiraghi, *Nat. Nanotechnol.* **2017**, *12*, 343.

[134] Y. Meng, K. Wang, Y. Zhang, Z. Wei, *Adv. Mater.* **2013**, *25*, 6985-6990.

[135] Z.-S. Wu, Z. Liu, K. Parvez, X. Feng, K. Müllen, *Adv. Mater.* **2015**, *27*, 3669-3675.

[136] D. Yu, K. Goh, H. Wang, L. Wei, W. Jiang, Q. Zhang, L. Dai, Y. Chen, *Nat. Nanotechnol.* **2014**, *9*, 555.

[137] Z.-S. Wu, K. Parvez, S. Li, S. Yang, Z. Liu, S. Liu, X. Feng, K. Müllen, *Adv. Mater.* **2015**, *27*, 4054-4061.

[138] R. Liu, L. Wan, S. Liu, L. Pan, D. Wu, D. Zhao, *Adv. Funct. Mater.* **2015**, *25*, 526-533.

[139] Z.-S. Wu, K. Parvez, A. Winter, H. Vieker, X. Liu, S. Han, A. Turchanin, X. Feng, K. Müllen, *Adv. Mater.* **2014**, *26*, 4552-4558.

[140] W. Zhang, Y. Zeng, N. Xiao, H. H. Hng, Q. Yan, *J. Mater. Chem.* **2012**, *22*, 8455-8461.

[141] W. Wei, G. Wang, S. Yang, X. Feng, K. Müllen, *J. Am. Chem. Soc.* **2015**, *137*, 5576-5581.

[142] L. Zhang, H. Huang, H. Yin, Y. Xia, J. Luo, C. Liang, Y. Gan, X. Tao, W. Zhang, *J. Mater. Chem. A* **2015**, *3*, 16513-16519.

[143] B. Lung-Hao Hu, F.-Y. Wu, C.-T. Lin, A. N. Khlobystov, L.-J. Li, *Nat. Commun.* **2013**, *4*, 1687.

Chapter 2

Organic Radical-Assisted Electrochemical Exfoliation for the Scalable Production of High-Quality Graphene

Keywords: graphene, electrochemical exfoliation, radical scavenger, graphene ink

ToC graphic

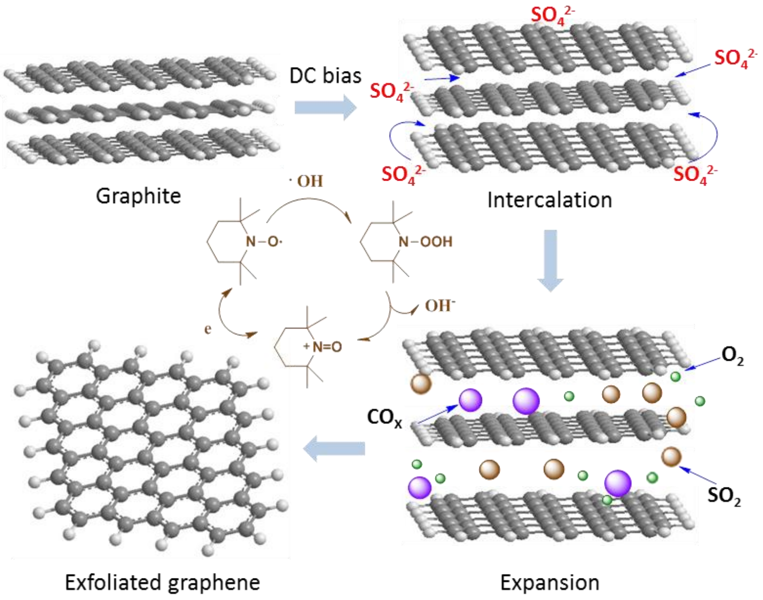

Published in:

Journal of the American Chemical Society

Reprinted with permission from (*J. Am. Chem. Soc.*, **2015**, *137*, 13927-13932)

INTRODUCTION

The exceptional electronic, thermal, optical and mechanical properties of graphene render it a remarkable candidate for the next generation of electronic and optoelectronic devices.[1] Consequently, techniques for the scalable production of high-quality, solution-processable graphene are needed. Among the numerous protocols employed to date, the exfoliation of bulk graphite is most common for harvesting graphene sheets on a large scale because of its low process complexity and costs. Direct exfoliation in the solid state (e.g., scotch-tape cleavage,[2] ball milling [3,4]) or in a liquid phase (e.g., liquid phase sonication,[5-7] shear force exfoliation[8]), also known as physical exfoliation, provides feasible means for producing graphene with a low number of defects, although in an insufficient yield (< 5 %) and/or with small flake sizes (< 1 μm). In comparison, chemical exfoliation, which generally relies on Hummers' method, offers a wide range of flexibility for the production of graphene oxide (GO) and related materials because of the potential scalability, impressive conversion efficiency (~100 %), and superior processability. Unfortunately, the unique physical properties of graphene are seriously compromised and cannot be sufficiently recovered, even upon reduction, because of the appreciable fraction of oxygen groups and defects that are left behind. These oxygen groups restrict its usage in fine applications.[9,10]

Electrochemical exfoliation has recently emerged as a promising strategy for producing graphene on an industrial scale with high efficiency, at low cost and in an environmentally friendly manner.[11] Either cathodic or anodic potentials are able to drive guest ions into graphitic layers, which promotes the structural deformation of a graphite working electrode.[12,13] Cationic intercalation (mainly in organic electrolytes) does not involve oxidizing conditions, and therefore avoids the decoration of the final products with oxygen containing groups. Unfortunately, in most cases, the produced graphene is in the form of a few layers, and its further isolation requires prolonged sonication (> 10 h) or other multistep treatments (e.g., microwave irradiation).[14-16] Anionic intercalation (primarily in aqueous electrolytes) is less time demanding and can take less than one hour. However, the graphene produced is generally decorated with functional oxygen groups that occur due to the positive potentials used, especially with acidic electrolytes (e.g., sulfuric acid[17,18]). It is noteworthy that the strong oxidation can be partially alleviated by using aqueous sulfonic salts as electrolytes.[19] Nevertheless, the radicals (e.g., HO·) generated from water electrolysis will unavoidably disrupt the graphitic structure during the exfoliation process.[11,18,20,21] Therefore, it is highly desirable to eliminate these radicals to ultimately improve the quality of the graphene.

In this study, the electrochemical exfoliation of graphene is carried out in the presence of a series of antioxidants (such as ascorbic acid, gallic acid, hydrazine, sodium borohydride, hydrogen iodide and (2,2,6,6-tetramethylpiperidin-1-yl)oxyl (TEMPO)) in a neutral aqueous electrolyte (ammonium sulfate) to suppress the radical attack from water electrolysis. Remarkably, using TEMPO, the electrochemically exfoliated graphene (EG) produced is of exceptionally high quality, and the process gives high exfoliation efficiencies. TEMPO is an inexpensive compound, and it has been widely used to terminate chain growth in controlled free radical polymerization.[22-24] Specifically, the produced EG exhibits large lateral sizes (ranging from 5 μm to 10 μm), outstanding hole mobilities (~ 405 $cm^2 V^{-1} s^{-1}$), very low Raman I_D/I_G ratios (below 0.1) and extremely high carbon to oxygen (C/O) ratios (25.3). Moreover, the throughput can be readily increased through continuous production (~15.1 grams per hour in laboratory tests). In addition, such high-quality EG still shows great processability in various solvents, such as *N*,*N*-dimethylforamide (DMF), to form concentrated stable dispersions (6.0 mg mL^{-1}). This graphene ink allows for the fabrication of flexible conductive films and supercapacitors. A 20-nm-thick graphene film exhibits a sheet resistance as low as 3.91 kΩ sq^{-1}, decreasing further to 0.51 kΩ sq^{-1} upon doping with HNO_3. An assembled graphene paper supercapacitor demonstrates a high area capability of 11.5 mF cm^{-2} (at a scan rate of 2 mV s^{-1}). The electrochemically exfoliated high-quality graphene will be useful in applications that involve hybrid composites, conductive or mechanical additives, and energy storage and conversion devices, among others.

RESULTS AND DISCUSSION

Electrochemical Exfoliation. Graphite exfoliation was conducted in a home-built setup that used rolled graphite foils as working electrodes and platinum foils as counter electrodes (**Figure 1a**). An aqueous solution containing ammonium sulfate with a range of reducing agents (e.g., ascorbic acid, gallic acid, hydrazine monohydrate, sodium borohydride ($NaBH_4$), hydrogen iodide, TEMPO; chemical structures shown in **Figure S1**) was tested as an electrolyte. Before exfoliation, the graphite foil was pretreated by alternately soaking it in liquid nitrogen and absolute ethanol. During this process, violent nitrogen evolution and ethanol solidification promoted the expansion of the graphite foils. The dilation was extremely rapid (within 10 s) and yielded a drastic volume increase at the graphite boundary (~10 times) (**Figure S2**), which facilitated the expansion of the graphite layers, as did the following anion intercalation steps. When the graphite anodes were immersed in the electrolyte, by applying a static bias of 10 V, they detached into small pieces in less than 10 s, spreading on top of the electrolyte and/or on the bottom of the electrochemical cell. After filtration and copious washing, these exfoliated graphene sheets were collected and then dispersed in DMF via mild sonication. The concentration of graphene dispersion was measured by filtration method. The dispersion (~0.3 mg mL^{-1}) was stable for two weeks without apparent aggregation (**Figure 1b**). The total exfoliation yield was calculated using the mass ratio of dried graphene powder and the starting graphite precursor. Among the reductants, gallic acid and hydrogen iodide were not stable after turning on the electrical voltage. Hydrazine promoted exfoliation in very limited yield (less than 10 wt%). The addition of ascorbic acid, sodium borohydride or TEMPO into conventional ammonium sulfate electrolyte does not change the efficiency of graphite exfoliation. Especially, a high yield of 75 wt% has been achieved with the use of TEMPO. It is worth noting that to maintain a constant concentration of sodium borohydride, it should be added successively because its hydrolysis occurs spontaneously during the exfoliation process.

$$BH_4^- + 2\, H_2O \rightarrow BO_2^- + 4\, H_2\ (\Delta H < 0)$$

Moreover, depending on the size of the graphite foil and the volume of the electrolyte, the throughput can be easily scaled up to tens of grams. For instance, a mid-sized electrochemical cell was tested in continuous exfoliation with two graphite foils (A4 size, ca. 30 cm×20 cm, **Figure 1c**), which enabled the production of ~15.1 grams of graphene per hour (**Figure 1d**).

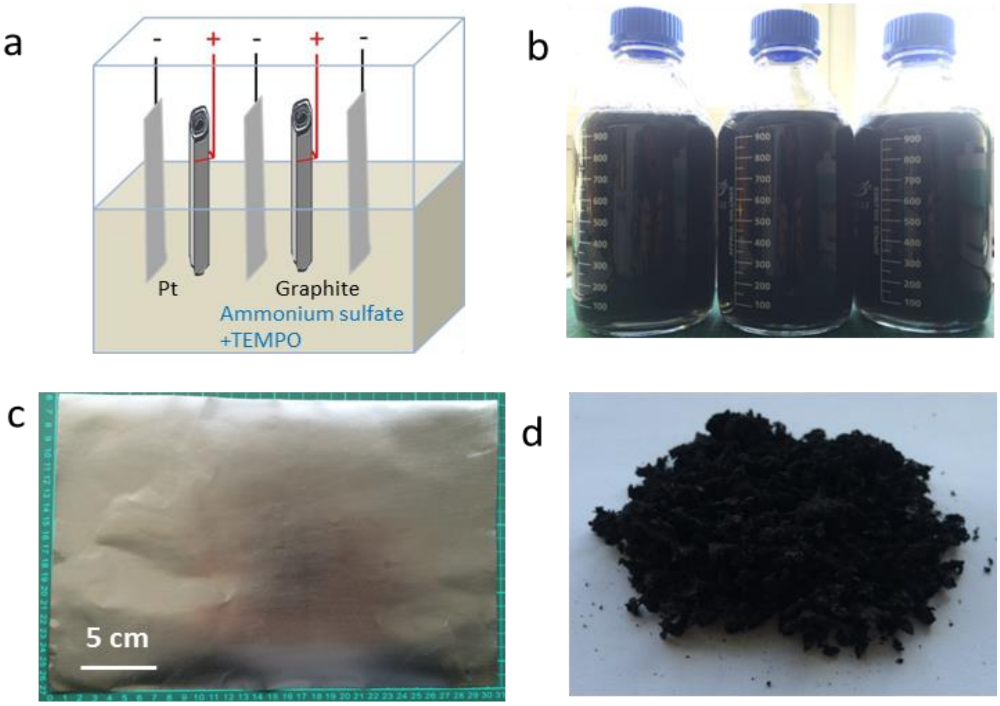

Figure 1. Electrochemical exfoliation of graphite: (a) schematic illustration of an electrochemical cell, (b) stable graphene-DMF dispersions prepared from radical-assisted electrochemical exfoliation, (c) A piece of A4-sized graphite foil, (d) dried graphene powder (~15.1 g).

Morphological Elucidation. When a voltage was applied, the morphology of the graphite changed abruptly within a few seconds at both the surface and the boundaries

(**Figure S3**); this behavior was independent of the type of reducing agents employed in the electrolyte. Typically, the as-received graphite foil possesses a smooth surface and a clean edge. After 5 s of exfoliation, cracks, bulges and crumbles were observed both on the surface and at the boundaries. After 10 s, the surface exhibited more irregular and rougher microstructures, including a network of ripples. The visible gas evolution led to the swelling of the graphite layers, which caused an obvious expansion at the edges. After 30 s, the surface was altered to a curled morphology that consisted of thin, wrinkled, tissue-like structures. The edge of the graphite foil expanded to a size almost 10 times that of its initial state. After 60 s, a notably high number of graphene sheets had left the anode and spread into the electrolyte.

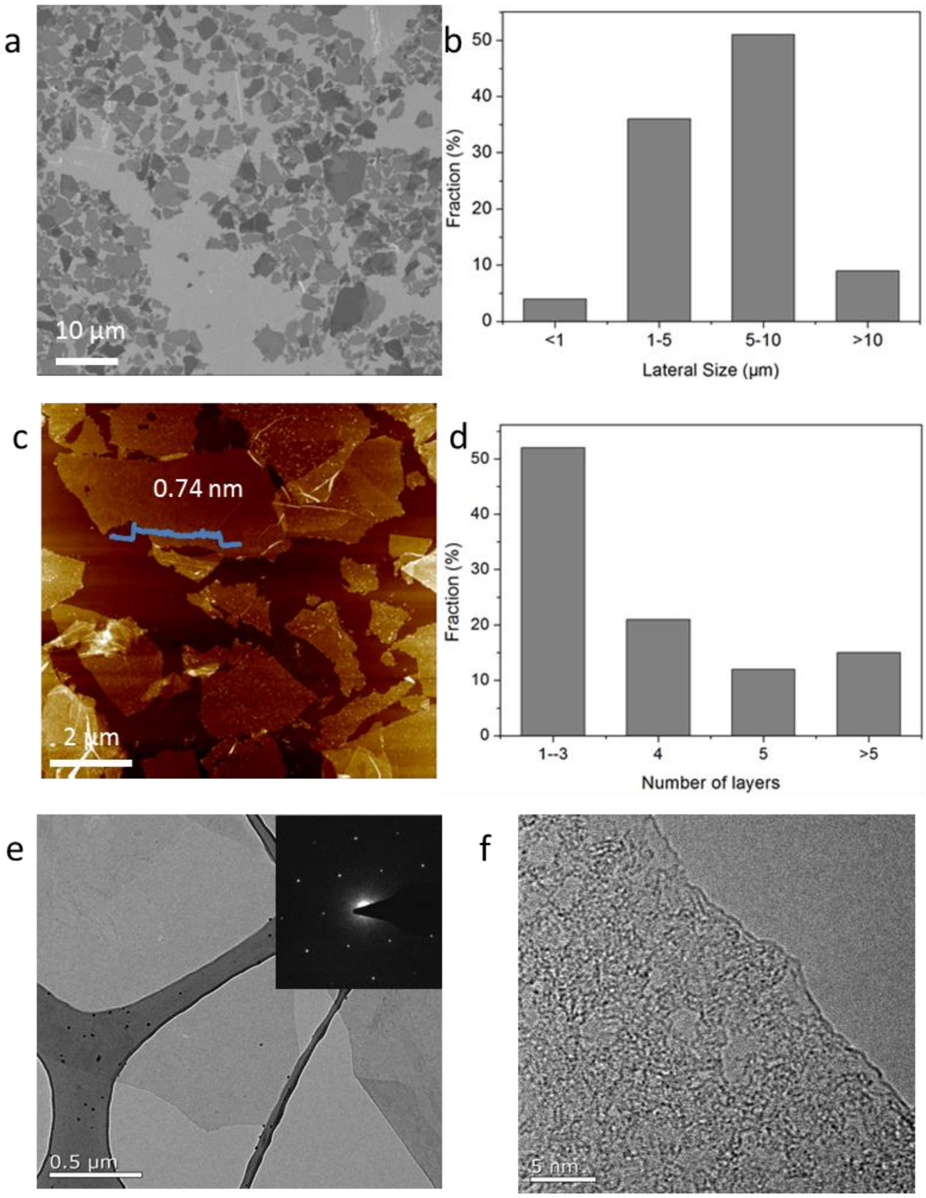

Figure 2. Morphology of exfoliated graphene: (a) SEM image of a large area of graphene on a Si/SiO_2 substrate, (b) statistical lateral size distribution determined by SEM, (c) AFM image of exfoliated graphene on SiO_2, (d) statistical height profile analysis determined by AFM, (e) typical TEM image of a graphene sheet (inset: SAED pattern), (f) high-resolution TEM at the edge of a single-layer graphene sheet.

The exfoliated graphene sheets were then transferred onto a Si/SiO_2 substrate using the Langmuir-Blodgett method. The scanning electron microscopy (SEM) image displayed in **Figure 2a** provides unambiguous evidence for the uniform coverage of the SiO_2 surface with assemblies of graphene sheets (hundreds of μm^2 in size). The statistical analysis of 150 sheets revealed that the predominant lateral size distribution was between 5 and 10 μm and that approximately 10 % of the graphene sheets were larger than 10 μm (**Figure 2b**). The number of layers per sheet was estimated using atomic force microscopy (AFM). The thickness of the single-layer graphene sheets (0.74 nm) was in accordance with that of pristine graphene on a Si wafer (**Figure 2c**).[25] Bilayer (1.32 nm) and trilayer (2.01 nm) sheets were also detected (**Figure S4**). A histogram of the thickness of 100 graphene sheets obtained by cross-sectional analysis displays that approximately 52 % of the sampled graphene sheets are between 1 and 3 layers thick (23 % monolayers, 29 % bilayers and trilayers) (**Figure 2d**). The decreased yield of 1-3 layered graphene is ascribed to the re-aggregation of the sheets that occurs during the exfoliation process and/or sample preparation. Transmission electron microscopy (TEM) reveals that the graphene sheets typically feature some overlapping regions. This partial stacking results from the heating process that occurs during sample preparation, which is widely used to evaporate solvents.[26] The selected-area electron diffraction (SAED) image at the central part of the graphene sheet identifies the high-quality crystalline structure evidenced by the typical six-fold symmetric diffraction patterns (**Figure 2e**).[27] A high-resolution TEM (HR-TEM) analysis of the flake edges reveals the well-defined structure of a single-layer graphene sheet (**Figure 2f**).

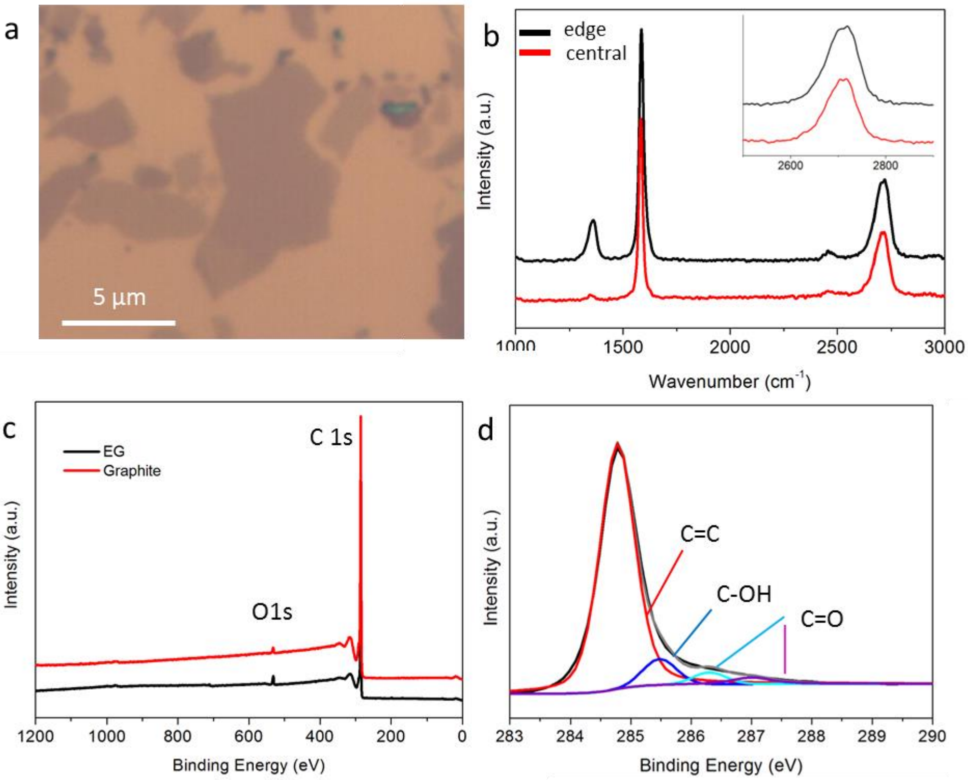

Figure 3. Structural characterization of exfoliated graphene: (a) representative EG sheets visualized by optical microscope, (b) representative Raman spectra from both the edge and the central plane of an EG sheet (532 nm laser excitation), (c) XPS survey spectra of graphite and EG, (d) high-resolution C 1s spectrum measured on a thin EG film.

Structural Investigation. EG flakes supported on Si/SiO$_2$ substrate can be visualized by optical microscope (**Figure 3a**). This is important for Raman to capture spectra from different EG positions. As shown in **Figure 3b**, **Figure S5a** and **Figure S5b**, a typical Raman spectrum (532 nm laser excitation) exhibits three main bands: one at 1353 cm^{-1} (D band), which is associated with the breathing mode of the sp^3 carbon atoms; one at 1582 cm^{-1} (G band), which corresponds to the in-plane vibrations of the graphene lattice; and one at 2705 cm^{-1} (2D band), which is an overtone of the D band.8 It has been well accepted that the intensity ratio of the D band to the G band (I_D/I_G) is associated with the content of defects. EG sheets that were prepared using ascorbic acid and sodium borohydride exhibited relatively low I_D/I_G ratios (0.23 and 0.15, respectively). Remarkably, using TEMPO, the EG sheets show only a slight bulge at the position of D band and exhibit an I_D/I_G ratio below 0.1, which suggests that they have a very low defect density on the basal plane. Because edges act as "defects" during the Raman scattering process, the I_D/I_G ratio at the edge (0.17) is generally higher than that at the center of the plane.[28] The relatively low intensity of the 2D band indicates that few-layer graphene (2-4 layers) is present, which could be due to the re-aggregation or folding of the samples during their preparation (this hypothesis could be confirmed by AFM characterization).[8]

X-ray photoelectron spectroscopy (XPS) provided insight into the chemical composition of the exfoliated graphene (**Figure 3c**, **Figure S5c** and **Figure S5d**): only 6.6 % and 8.4 % atomic oxygen content was detected in EG samples prepared with $NaBH_4$ and ascorbic acid, respectively. Remarkably, EG prepared using TEMPO exhibited the lowest oxygen content (as low as 3.8 %). This value is only slightly higher than that of the pristine graphite precursor (1.7 %). Thus, the C/O ratio of the graphene sample is 25.3, which is much greater than the C/O ratios of the graphene samples prepared using other wet-chemical methods (**Table S1**, Supporting Information). According to the high-resolution spectrum of C1s (**Figure 3d**), a sharp peak located at a binding energy (BE) of 284.6 eV corresponds to the sp^2 carbons (graphitic C=C species),[29,30] and the other peaks at 285.4 eV, 286.5 eV and 287.2 eV are assigned to the sp3 carbons (C-OH),[31,32] and the oxygen-carbon groups (C-O-C, C=O),[32] respectively. Carboxylic groups (O-C=O) were not detected at 290.2 eV.[19]

Exfoliation Mechanism. In general, the efficient intercalation of electrolyte into graphite interlayer and the subsequent gas eruption are the key factors governing graphite exfoliation (**Figure 4**).

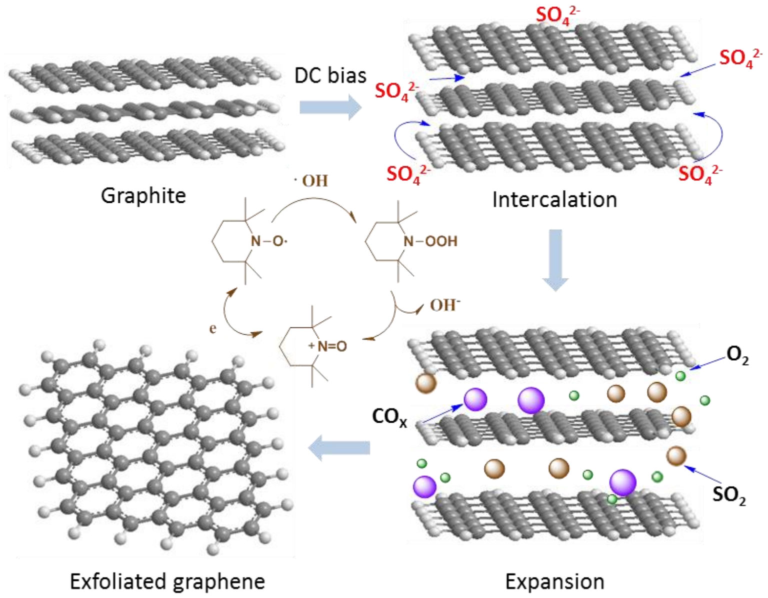

Figure 4. Mechanism of radical assisted electrochemical exfoliation. The exfoliation process includes two stages, intercalation and expansion. TEMPO acts as a radical-eliminating agent, defending against the attack of oxidative radicals; the intercalation of sulfate ions lead to exfoliation.

The intercalation process preferentially opens up the grain boundary, edge sites and other intrinsic defects where van der Waals interactions are weak, promoting gas evolution at the corresponding sites. Afterwards, the large volume expansion on a microscopic scale enables efficient exfoliation. It is well known that, in dilute or moderately concentrated salt solutions, water splitting takes place at a standard potential of 1.23 V, generating oxygen gas at the anode. Nevertheless, the high anodic potential (e.g. 10 V) discharges water into active intermediates, such as hydroxyl radicals, at the graphite interfaces.[33]

$H_2O \rightarrow 2\,H^+ + 2e^- + 1/2\,O_2$

$H_2O \rightarrow H^+ + e^- + HO\cdot$

$HO\cdot \rightarrow H^+ + e^- + O\cdot$

In the meantime, hydroxyl radicals (HO·) start to corrode the graphite electrode at the edges which is necessary to open the boundaries such that the sulfate ions are able to intercalate. However, these radicals are non-selective and highly active, and they cause the continuous oxidization of the graphite from the edges to the central plane.[20,21,34] By using TEMPO, the extent of damage in graphene lattice, which is possibly caused by radical attack, could in principle be very low. And extensive graphite oxidation or structural disruption is not crucial for complete and fast exfoliation. The following exfoliation mechanism is proposed.

In the presence of the TEMPO radical, the reactive hydroxyl radical ($HO\cdot$) will likely react immediately with the surrounding TEMPO radicals (nitroxides) to form metastable intermediates (e.g., TEMPO-OH), which are eventually converted to oxoammonium cations. [35]

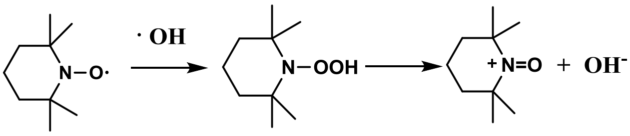

The oxoammonium cations will be electrochemically reduced at the cathode, forming pristine TEMPO radicals.

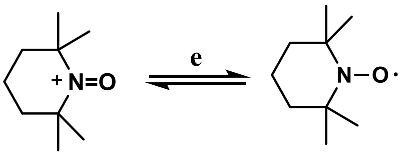

UV-vis spectroscopy was carried out in order to monitor the stability of TEMPO under high potential. As shown in **Figure S6**, TEMPO exhibits a distinctive UV absorbance maximum at 425 nm. After 10 min, the intensity of band decays slightly. When it comes to 60 min, the concentration of TEMPO decreases dramatically owing to its electrochemical decomposition at air/water interfaces.[36]

The elimination of these radicals undoubtedly will prevent the graphite anode from excess-oxidation. Moreover, the high complexity of electrochemical reactions results in the violent evolution of various gaseous species (such as CO_x, SO_2 and O_2),[19] which will significantly weaken the van der Waals interactions and move the weakly bonded graphite layers apart.

To test this hypothesis, various adding amounts of TEMPO were investigated for graphite exfoliation (**Figure S7**). In all cases, the ammonium sulfate concentration was fixed at 0.1 M. The exfoliation efficiency of graphite gradually decreased with the increasing TEMPO concentration. When it ranged from 0.5 to 2 mg mL^{-1}, the exfoliation yields did not change (~70 wt%). However, when the concentration of TEMPO was increased to 8 mg mL^{-1}, the yield dropped to ~45 wt%. This result strongly confirms that oxidation at the boundaries (by radical attack) is crucial for the next step in the process (the intercalation of the sulfate ions). When most of the radicals are eliminated, the exfoliation yield is expected to be quite low.

Notably, we found that the addition of TEMPO decreased the defects present in the exfoliated graphene prepared using other aqueous electrolyte systems (**Figure S8**). For instance, with the use of TEMPO, the I_D/I_G ratio of the exfoliated graphene dropped from 0.47 to 0.28 for potassium sulfate (K_2SO_4) as aqueous electrolyte and from 0.58 to 0.32 for sodium sulfate (Na_2SO_4). Thus, the effective control of the I_D/I_G ratio is consistent with the proposed radical-eliminating hypothesis.

Electrical Properties. The electrical properties of both single EG layers and continuous thin films (tens of nanometers thick) were evaluated using field-effect transistor and sheet resistance measurements, respectively. **Figure 5a** shows the SEM images of an as-prepared device containing a graphene sheet in the channel. An AFM image (**Figure 5b**) confirms that the EG flake assembled in the device is a monolayer. The mobility extracted from the transfer curves is ~405 cm^2 V^{-1} s^{-1}, which is substantially greater than that of reduced graphene oxide (123 cm^2 V^{-1} s^{-1})[37] and electrochemically exfoliated graphene in sulfuric acid (233 cm^2 V^{-1} s^{-1})[18] or ammonium sulfate aqueous solution (310 cm^2 V^{-1} s^{-1})[19] (detailed comparison is listed in **Table S2** and **Table S3, Supporting Information**). The sheet resistance (*Rs*), measured from the two-terminal I-V traces, is 1.91 kΩ sq^{-1}. This value is comparable to some undoped

CVD-grown graphene samples.[38] Continuous graphene films were prepared by filtering a dilute graphene dispersion and then mechanically compressing it. The thickness of the

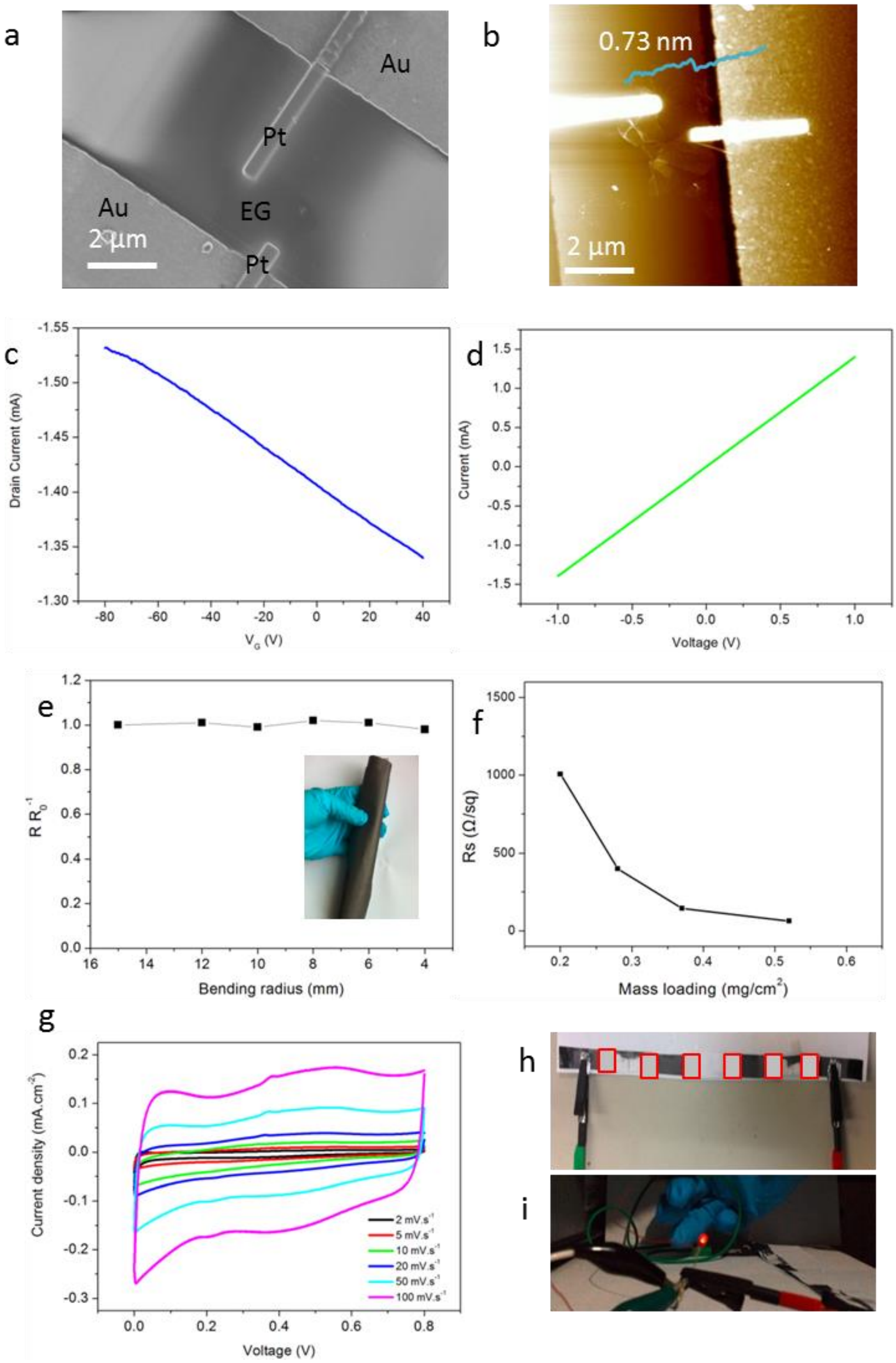

Figure 5. Electrical properties of EG. (a) SEM and (b) AFM images of an as-prepared FET device. (c) Transfer curve and (d) current-voltage (I-V) curves of a FET device based on single-layer graphene. (e) The alternation of sheet resistance with the change

of bending radius (inset: photograph of a rolled graphene paper). (f) Relationship between the resistance and graphene mass loading. (g) Cyclic voltammetry curves of the supercapacitors (graphene mass loading 0.52 mg cm^{-2}) at scan rates between 2 and 100 mV s^{-1}. (h,i) Photographs of the as-made connected supercapacitor and the moment when the LED lit up.

film could be easily adjusted by tuning the volume and concentration of the starting dispersion. The transparency was monitored by UV spectroscopy at 550 nm. Thin graphene films (10 nm) exhibited a transparency of 85 %, which is comparable to that of commercial ITO glass (90 % in the visible region) (**Figure S9**).[39] The *Rs* was measured after the samples were annealed at a low temperature (200 °C) overnight to remove any residual solvents. The average value recorded by a four-probe system was 9.47 kΩ sq^{-1} and 3.91 kΩ sq^{-1} for films with a thickness of 10 nm and 20 nm, respectively. Because nitric acid (HNO_3) is effective for p-doping graphene films,[40] after treatment with HNO_3 (65 %, 2 hours), the doped EG films displayed Rs values of 1.10 and 0.51 kΩ sq^{-1}, respectively, and maintained their optical transparency. The high transparencies of these conductive EG films compared well with those of graphene films that were made from the thermal intercalation-exfoliation approach or via the thermal reduction of graphene oxide.[9,41] To explore the application of such high-quality graphene in printable flexible electronics, a concentrated dispersion of EG in DMF (6.0 mg mL^{-1}), as known as graphene ink, was freshly prepared and deposited on a commercial A4 paper by brush painting (**Figure S10a**). The resulting graphene paper (**Figure S10b**) displayed outstanding flexibility because it could be bent arbitrarily without breaking (**Figure 5e**). A bending test of the graphene paper also demonstrated that the electrical conductivity remained nearly the same when the radius was reduced from 15 mm to 4 mm. Moreover, the resistance of the graphene paper varied with different graphene loading. **Figure 5f** shows that the resistance dropped from 980 Ω sq^{-1} to 15 Ω sq^{-1} with an increase of the EG mass loading from 0.21 mg cm^{-2} to 0.52 mg cm^{-2}, respectively. This superior conductivity at high loading is comparable to that of carbon nanotube paper.[42]

In view of such controllable mass loading, the graphene paper holds great promise for the fabrication of flexible solid-state supercapacitors. In this case, the paper serves as a flexible substrate, and its porous structure allows for the diffusion of electrolyte ions, thus avoiding the use of any binders or additives. Towards this end, two graphene papers (mass loading: 0.52 mg cm^{-2}) were integrated together with a layer of solidified conductive gel (poly(vinyl alcohol)/sulfuric acid) to assemble an all-solid-state supercapacitor. In a cyclic voltammetry test, this flexible graphene paper-based supercapacitor showed typical double-layer capacitive behavior at various scan rates (**Figure 5g**). The calculated capacitance per geometric area was 11.5 mF cm^{-2} (scan rate: 2 mV s^{-1}), which is much higher than that of reduced graphene oxide (rGO)-cellulose paper supercapacitors (7.6 mF cm^{-2}).[43] The residual oxygen-containing groups and defects on rGO are major barriers to high electrochemical performance. To examine the possible practical applications, six small paper supercapacitors (active area: 2 cm^2 × 6) were connected in series (**Figure S10C**), and the assembled device had the capability to light up a red light-emitting diode (LED) at 2.5 V, as shown in **Figure 5h** and **5i**.

CONCLUSION

We have developed a controllable electrochemical approach for graphite exfoliation with the assistance of antioxidants. Among them, TEMPO was found to promote exfoliation, which led to graphene exhibiting superior quality in high yield. The exfoliated graphene sheets are large in size, and they have remarkably high hole mobilities (~405 cm^2 V^{-1} s^{-1}) and high carbon to oxygen (C/O) ratios (25.3). The process used to prepare such graphene samples is superior to other wet-chemical approaches. Moreover, the high solution-processability of graphene opens up ample opportunities for the fabrication of graphene-based thin film electrodes. Given that all of the reagents employed in this exfoliation system are commercially available and inexpensive and that the process is extremely fast, compatible to scale-up and free of polluting by-products, our method holds great promise to support the realization of an industrial graphene market.

ASSOCIATED CONTENT

Supporting Information. Experimental details; chemical structure of reducing agents in this work, morphological changes of graphite during exfoliation process, additional AFM; Raman spectra of exfoliated graphene, UV-vis spectra of electrolyte; Comparison of wet-chemical methods for graphite exfoliation.

ACKNOWLEDGMENT

This work was financially supported by the ERC Grant on NANOGRAPH and 2DMATER, EC Marie Curie ITN Project GENIUS and IC- ICT FET-Proactive MoQuas, as well as the EC under Graphene Flagship (No. CNECT-ICT-604391), the FET project UPGRADE (project no. 309056), the ANR through the LabEx project, BMBF INSOLCELL project, the International Center for Frontier Research in Chemistry (icFRC). The authors thank Dr. [redacted] for HR-TEM measurement. [redacted] would like to thank China scholarship council (CSC) for financial support.

Reference

(1) Gwon, H.; Kim, H.-S.; Lee, K. U.; Seo, D.-H.; Park, Y. C.; Lee, Y.-S.; Ahn, B. T.; Kang, K. *Energy Environ. Sci.* **2011**, *4*, 1277.

(2) Novoselov, K. S.; Geim, A. K.; Morozov, S. V.; Jiang, D.; Zhang, Y.; Dubonos, S. V.; Grigorieva, I. V.; Firsov, A. A. *Science* **2004**, *306*, 666.

(3) León, V.; Rodriguez, A. M.; Prieto, P.; Prato, M.; Vázquez, E. *ACS Nano* **2014**, *8*, 563.

(4) Jeon, I.-Y.; Shin, Y.-R.; Sohn, G.-J.; Choi, H.-J.; Bae, S.-Y.; Mahmood, J.; Jung, S.-M.; Seo, J.-M.; Kim, M.-J.; Wook Chang, D.; Dai, L.; Baek, J.-B. *Proc. Natl. Acad. Sci. USA* **2012**, *109*, 5588.

(5) Hernandez, Y.; Nicolosi, V.; Lotya, M.; Blighe, F. M.; Sun, Z.; De, S.; McGovern, I. T.; Holland, B.; Byrne, M.; Gun'Ko, Y. K.; Boland, J. J.; Niraj, P.; Duesberg, G.; Krishnamurthy, S.; Goodhue, R.; Hutchison, J.; Scardaci, V.; Ferrari, A. C.; Coleman, J. N. *Nat. Nanotechnol.* **2008**, *3*, 563.

(6) Lotya, M.; Hernandez, Y.; King, P. J.; Smith, R. J.; Nicolosi, V.; Karlsson, L. S.; Blighe, F. M.; De, S.; Wang, Z.; McGovern, I. T.; Duesberg, G. S.; Coleman, J. N. *J. Am. Chem. Soc.* **2009**, *131*, 3611.

(7) Coleman, J. N. *Acc. Chem. Res.* **2013**, *46*, 14.

(8) Paton, K. R.; Varrla, E.; Backes, C.; Smith, R. J.; Khan, U.; O'Neill, A.; Boland, C.; Lotya, M.; Istrate, O. M.; King, P.; Higgins, T.; Barwich, S.; May, P.; Puczkarski, P.; Ahmed, I.; Moebius, M.; Pettersson, H.; Long, E.; Coelho, J.; O'Brien, S. E.; McGuire, E. K.; Sanchez, B. M.; Duesberg, G. S.; McEvoy, N.; Pennycook, T. J.; Downing, C.; Crossley, A.; Nicolosi, V.; Coleman, J. N. *Nat. Mater.* **2014**, *13*, 624.

(9) Li, D.; Muller, M. B.; Gilje, S.; Kaner, R. B.; Wallace, G. G. *Nat. Nanotechnol.* **2008**, *3*, 101.

(10) Dreyer, D. R.; Park, S.; Bielawski, C. W.; Ruoff, R. S. *Chem. Soc. Rev.* **2010**, *39*, 228.

(11) Low, C. T. J.; Walsh, F. C.; Chakrabarti, M. H.; Hashim, M. A.; Hussain, M. A. *Carbon* **2013**, *54*, 1.

(12) Xia, Z. Y.; Giambastiani, G.; Christodoulou, C.; Nardi, M. V.; Koch, N.; Treossi, E.; Bellani, V.; Pezzini, S.; Corticelli, F.; Morandi, V.; Zanelli, A.; Palermo, V. *ChemPlusChem* **2014**, *79*, 439.

(13) Xia, Z. Y.; Pezzini, S.; Treossi, E.; Giambastiani, G.; Corticelli, F.; Morandi, V.; Zanelli, A.; Bellani, V.; Palermo, V. *Adv. Funct. Mater.* **2013**, *23*, 4684.

(14) Cooper, A. J.; Wilson, N. R.; Kinloch, I. A.; Dryfe, R. A. W. *Carbon* **2014**, *66*, 340.

(15) Wang, J.; Manga, K. K.; Bao, Q.; Loh, K. P. *J. Am. Chem. Soc.* **2011**, *133*, 8888.

(16) Zhong, Y. L.; Swager, T. M. *J. Am. Chem. Soc.* **2012**, *134*, 17896.

(17) Su, C.-Y.; Lu, A.-Y.; Xu, Y.; Chen, F.-R.; Khlobystov, A. N.; Li, L.-J. *ACS Nano* **2011**, *5*, 2332.

(18) Parvez, K.; Li, R.; Puniredd, S. R.; Hernandez, Y.; Hinkel, F.; Wang, S.; Feng, X.; Müllen, K. *ACS Nano* **2013**, *7*, 3598.

(19) Parvez, K.; Wu, Z.-S.; Li, R.; Liu, X.; Graf, R.; Feng, X.; Müllen, K. *J. Am. Chem. Soc.* **2014**, *136*, 6083.

(20) Wei, D.; Grande, L.; Chundi, V.; White, R.; Bower, C.; Andrew, P.; Ryhanen, T. *Chem. Commun.* **2012**, *48*, 1239.

(21) Lu, J.; Yang, J.-x.; Wang, J.; Lim, A.; Wang, S.; Loh, K. P. *ACS Nano* **2009**, *3*, 2367.

(22) Ohno, K.; Tsujii, Y.; Fukuda, T. *Macromolecules* **1997**, *30*, 2503.

(23) Zaremski, M. Y.; Plutalova, A. V.; Garina, E. S.; Lachinov, M. B.; Golubev, V. B. *Macromolecules* **1999**, *32*, 6359.

(24) Veregin, R. P. N.; Odell, P. G.; Michalak, L. M.; Georges, M. K. *Macromolecules* **1996**, *29*, 4161.

(25) Cheng, Z.; Zhou, Q.; Wang, C.; Li, Q.; Wang, C.; Fang, Y. *Nano Lett.* **2011**, *11*, 767.

(26) Ciesielski, A.; Haar, S.; El Gemayel, M.; Yang, H.; Clough, J.; Melinte, G.; Gobbi, M.; Orgiu, E.; Nardi, M. V.; Ligorio, G.; Palermo, V.; Koch, N.; Ersen, O.; Casiraghi, C.; Samorì, P. *Angew. Chem. Int. Ed.* **2014**, *53*, 10355.

(27) Geng, D.; Wu, B.; Guo, Y.; Huang, L.; Xue, Y.; Chen, J.; Yu, G.; Jiang, L.; Hu, W.; Liu, Y. *Proc. Natl. Acad. Sci. USA* **2012**, *109*, 7992.

(28) Dresselhaus, M. S.; Jorio, A.; Hofmann, M.; Dresselhaus, G.; Saito, R. *Nano Lett.* **2010**, *10*, 751.

(29) Park, K. H.; Lee, D.; Kim, J.; Song, J.; Lee, Y. M.; Kim, H.-T.; Park, J.-K. *Nano Lett.* **2014**, *14*, 4306.

(30) Park, K. H.; Kim, B. H.; Song, S. H.; Kwon, J.; Kong, B. S.; Kang, K.; Jeon, S. *Nano Lett.* **2012**, *12*, 2871.

(31) Kovtyukhova, N. I.; Wang, Y.; Berkdemir, A.; Cruz-Silva, R.; Terrones, M.; Crespi, V. H.; Mallouk, T. E. *Nat. Chem.* **2014**, *6*, 957.

(32) Zhang, L.; Zhang, Z.; He, C.; Dai, L.; Liu, J.; Wang, L. *ACS Nano* **2014**, *8*, 6663.

(33) Bergmann, M. E. H.; Rollin, J. *Catal. Today* **2007**, *124*, 198.

(34) Rao, K. S.; Sentilnathan, J.; Cho, H.-W.; Wu, J.-J.; Yoshimura, M. *Adv. Funct. Mater.* **2015**, *25*, 298.

(35) Samuni, A.; Goldstein, S.; Russo, A.; Mitchell, J. B.; Krishna, M. C.; Neta, P. *J. Am. Chem. Soc.* **2002**, *124*, 8719.

(36) Glandut, N.; Malec, A. D.; Mirkin, M. V.; Majda, M. *J. Phys. Chem. B* **2006**, *110*, 6101.

(37) Feng, H.; Cheng, R.; Zhao, X.; Duan, X.; Li, J. *Nat. Commun.* **2013**, *4*, 1539.

(38) Kholmanov, I. N.; Magnuson, C. W.; Aliev, A. E.; Li, H.; Zhang, B.; Suk, J. W.; Zhang, L. L.; Peng, E.; Mousavi, S. H.; Khanikaev, A. B.; Piner, R.; Shvets, G.; Ruoff, R. S. *Nano Lett.* **2012**, *12*, 5679.

(39) You, Y. Z.; Kim, Y. S.; Choi, D. H.; Jang, H. S.; Lee, J. H.; Kim, D. *Mater. Chem. Phys.* **2008**, *107*, 444.

(40) Bae, S.; Kim, H.; Lee, Y.; Xu, X.; Park, J.-S.; Zheng, Y.; Balakrishnan, J.; Lei, T.; Ri Kim, H.; Song, Y. I.; Kim, Y.-J.; Kim, K. S.; Ozyilmaz, B.; Ahn, J.-H.; Hong, B. H.; Iijima, S. *Nat. Nanotechnol.* **2010**, *5*, 574.

(41) Li, X.; Zhang, G.; Bai, X.; Sun, X.; Wang, X.; Wang, E.; Dai, H. *Nat. Nanotechnol.* **2008**, *3*, 538.

(42) Hu, L.; Choi, J. W.; Yang, Y.; Jeong, S.; La Mantia, F.; Cui, L.-F.; Cui, Y. *Proc. Natl. Acad. Sci. USA* **2009**, *106*, 21490.

(43) Weng, Z.; Su, Y.; Wang, D.-W.; Li, F.; Du, J.; Cheng, H.-M. *Adv. Energy Mater.* **2011**, *1*, 917.

Supporting Information

Organic Radical-Assisted Electrochemical Exfoliation for the Scalable Production of High-Quality Graphene

Experimental Section

Graphite Exfoliation. Typically, graphite exfoliation was performed in a two-electrode system, whereby graphite foils were used as working anodes and platinum foils as counter electrodes. Commercial graphite foil (Alfa Aesar) was pre-treated with liquid nitrogen and ethanol to trigger a modest expansion (put into liquid nitrogen for 30 s, quickly picked up and transferred into absolute ethanol, and finally dried in an oven). To avoid short circuits (connections between the graphite and Pt foils) during exfoliation, graphite foils were rolled like rods. The Pt foils were placed parallel to the graphite electrodes at a fixed distance of 2 cm. The electrolyte for the graphite exfoliation was prepared by dispersing ammonium sulfate crystals (0.05 M, 0.660 g) and TEMPO ((2,2,6,6-tetramethylpiperidin-1-yl)oxyl) (50 mg) in 50 mL of deionized (DI) water. In control experiments, ascorbic acid (50 mg), sodium borohydride (50 mg), gallic acid (50 mg), hydrazine monohydrate (50 mg) or hydrogen iodide (50 mg) was added to 50 mL of ammonium sulfate aqueous electrolyte (0.1 M), instead of TEMPO. A short sonication step (5 min, in an ice bath) was required to make a well-dispersed electrolyte. When the electrodes were immersed in the electrolyte, a static potential of 10 V was applied to start the electrochemical exfoliation process. When the exfoliation was complete, the suspended graphene sheets were collected with a 0.2 μm Polytetrafluoroethylene (PTFE) membrane filter and washed alternatively with DI water and ethanol by vacuum filtration. The washing process was repeated three times to clear any chemical residues. Later, the dark-gray product was dispersed in *N,N*-dimethylformamide (DMF) via mild sonication (15 min, in an ice bath). This homogeneous suspension sat overnight to remove un-exfoliated flakes and large particles. Then, the supernatant was taken out for further measurement and ultimately device fabrication.

Instrumentation. SEM images were obtained using a field-emission scanning electron microscope (Gemini 1530 LEO) with an accelerating voltage of 10 keV. HR-TEM and SAED were performed using a transmission electron microscope (Philips Tecnai F20). AFM characterization was carried out on a Veeco Nanoscope-IIIa - Multimode Picoforce (Digital Instruments). Raman spectroscopy was accomplished with a Bruker RFS 100/S spectrometer (laser wavelength 532 nm). XPS analyses were carried out on a Thermo Scientific K-Alpha X-ray photoelectron spectrometer with a basic chamber pressure of between ~10^{-8} – 10^{-9} mbar and with an Al anode as the X-ray source (x-ray radiation of 1496 eV). Spot sizes of 400 μm were used. Survey spectra were recorded with an average of 10 scans, a pass energy of 200.00 eV and a step size of 1 eV. High-resolution spectra were taken with an average of 10 scans with a pass energy of 50.00 eV and a step size of 0.1 eV. The sheet resistances of the EG films were measured with a four-point probe system using a Keithley 2700 multimeter (probe spacing: 0.635 mm, Rs=4.532 V/I).UV-vis spectroscopy was performed on Perkin Elmer Lambda 900 spectrometer.

Devices for Field Effect Transistor (FET). Thin electrochemically exfoliated graphene (EG) films for FET measurements were prepared using the Langmuir-Blodgett (LB) assembly method. A LB trough was equipped with two movable Teflon barriers, a pressure measurement sensor and a dipper, necessary to transfer the film onto a solid substrate. Deionized water was added as the supporting sub-phase, 1.5 mL of the EG dispersion in a 1:3 DMF/chloroform mixture was carefully dropped onto the water surface using a glass syringe. A small piece of filter paper was immersed into water to monitor the surface pressure during the compression of the EG film on the water surface when the two opposing barriers were moved towards each other. The target surface tension was set to 20 mN m^{-1}. By vertical dip-coating, an EG thin film was transferred onto a Si/SiO_2 wafer (with an oxide layer of 300 nm). The samples were carefully washed with DI water, then annealed at 200 °C for 30 min under vacuum to remove any residual solvents. To make single EG flake-based FETs, a thin platinum layer (200 nm) was deposited by focused ion beam lithography to connect the isolated flakes to the Au source/drain electrodes. The hole carrier mobility was calculated from the linear regime of the transfer curves with this equation:

$$\mu = \frac{L}{WC_iV_d} \times \frac{\Delta I_d}{\Delta V_g}$$

(where C_i is the dielectric capacitance (11 nF cm^{-2}, *J. Am. Chem. Soc.*, **2014**, 136, 6083), L is the channel length and W is the channel width).

The sheet resistance (Rs) of a single EG sheet was obtained on the same device, and the value was calculated using the following equation:

$$R_s = R \bullet \frac{W}{L}$$

(where R is the resistance at 0.5 V, L is the channel length, and W is the width of a single EG sheet).

All of the device tests were carried out inside a glove box filled with inert gas using a Keithley SCS 4200 semiconductor system.

Graphene Paper for Flexible Supercapacitors. EG powder (600 mg) was dispersed in 100 mL DMF (concentration of 6 mg mL^{-1}) by ice-bath sonication for 30 min. The black dispersion was painted on a commercial A4-size printing paper using a paintbrush. After this EG-coated paper was dried in an oven, a second layer was painted. The painting and drying process was repeated several times to achieve sufficient mass loading (0.20 - 0.50 mg cm^{-2}).The sheet resistance of the graphene paper was recorded using a four-point probe system. To make devices for supercapacitors, a polyvinyl alcohol (PVA)/H_2SO_4 gel was uniformly coated onto the graphene paper (1 cm×3 cm, EG loading ~0.5 mg cm^{-2}), then left to stand for 24 hours. Afterward, two pieces of graphene paper were stacked (active area 1 cm×1 cm) without a separator or current collector. To excite the LED light, six small devices were connected in a row. These all-solid-state flexible supercapacitors were eventually used for electrochemical characterization. The area capacitance value was obtained from the cyclic voltammetry data using the following equation:

$$C_{area} = \frac{1}{v(V_f - V_i)A}\int_{V_i}^{V_f} I(V)dV$$

(where C_{area} is the area capacitance based on graphene electrode (F cm^{-2}), v is the scan rate (V s^{-1}), V_f and V_i are the intergration potential limits of the voltammetric curve, $I(V)$ is the voltammetric discharge current (A), and A is the active area (cm^2) of the devices).

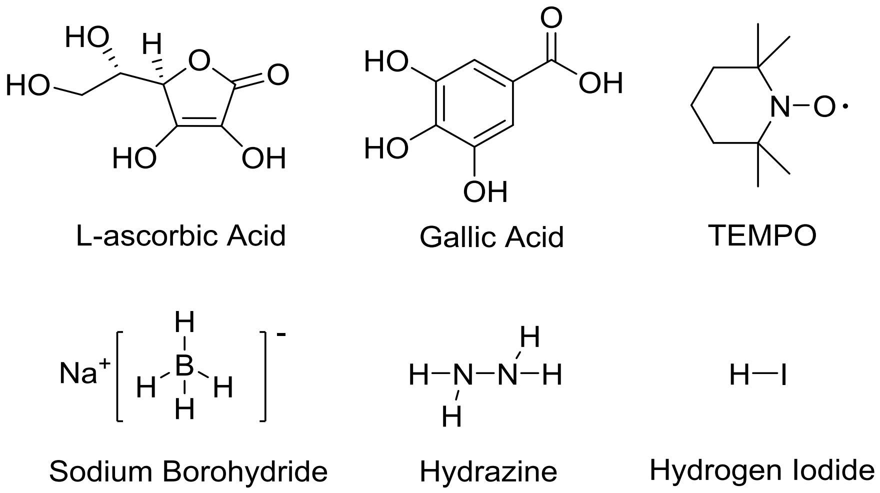

Figure S1 Chemical structures of the reducing agents used in this work

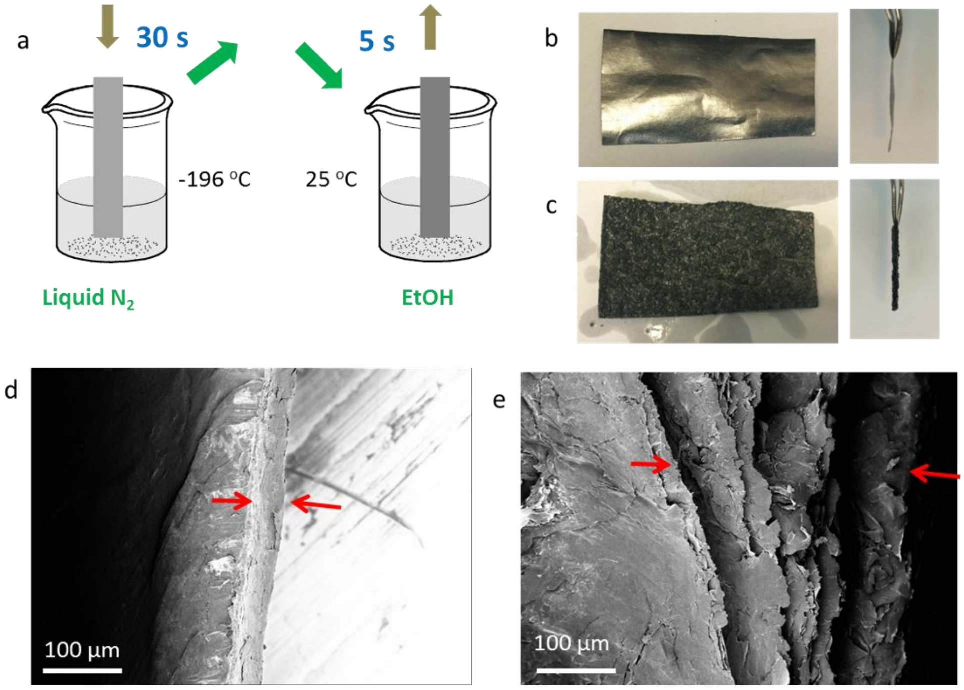

Figure S2 Pretreatment of graphite precursor. (a) Illustration of the alternating soaking process. (b) As-received commercial graphite foil (front view and side view). (c) The graphite foil, after treatment with liquid nitrogen and ethanol, showing a macroscopic wrinkle surface and expanded edges (front view and side view). (d, e) SEM images of the edge of the commercial graphite before and after treatment.

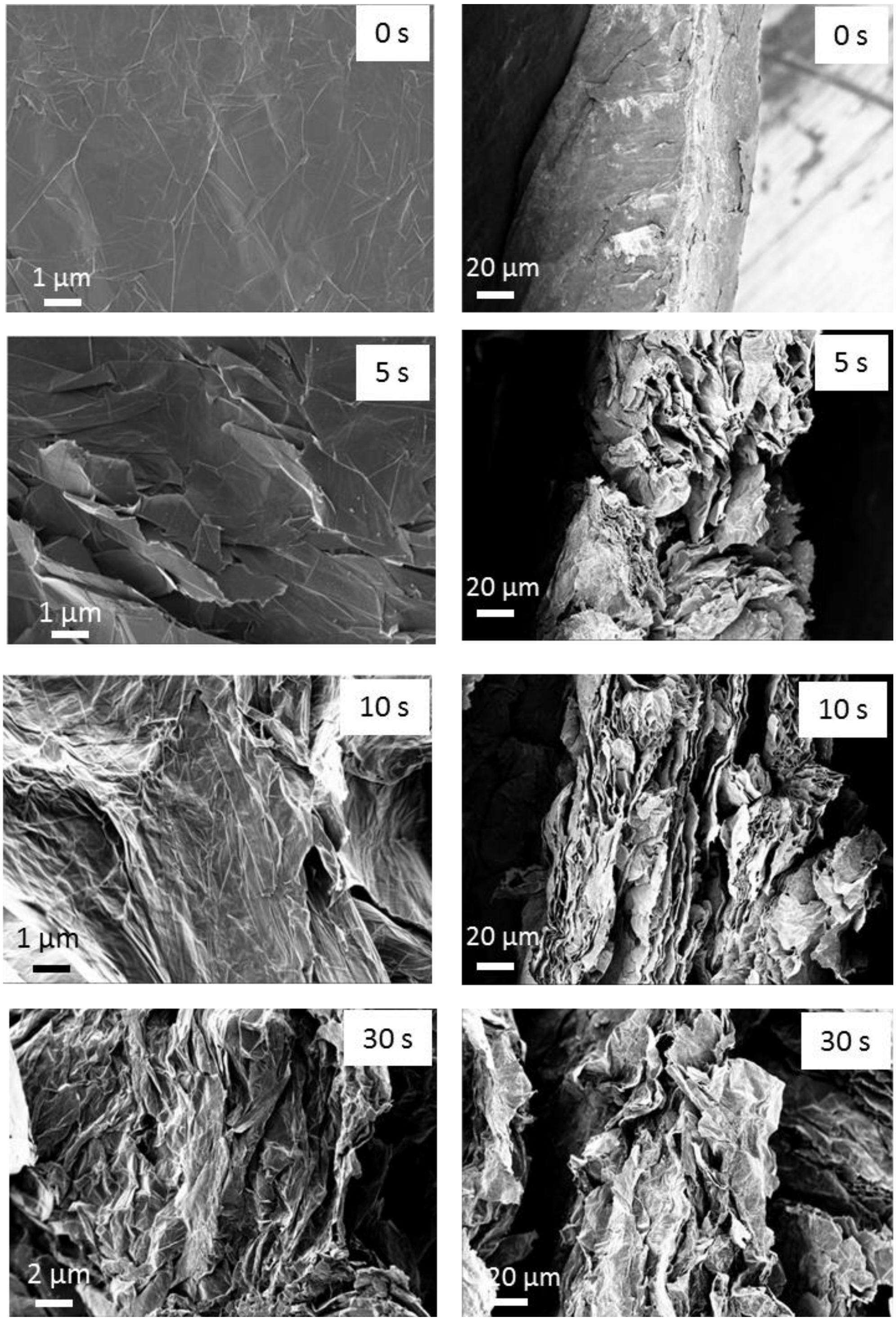

Figure S3 SEM images the surface (left) and the edge (right) of a graphite foil after applying a voltage of 10 V for various lengths of time (0 s, 5 s, 10 s and 30 s).

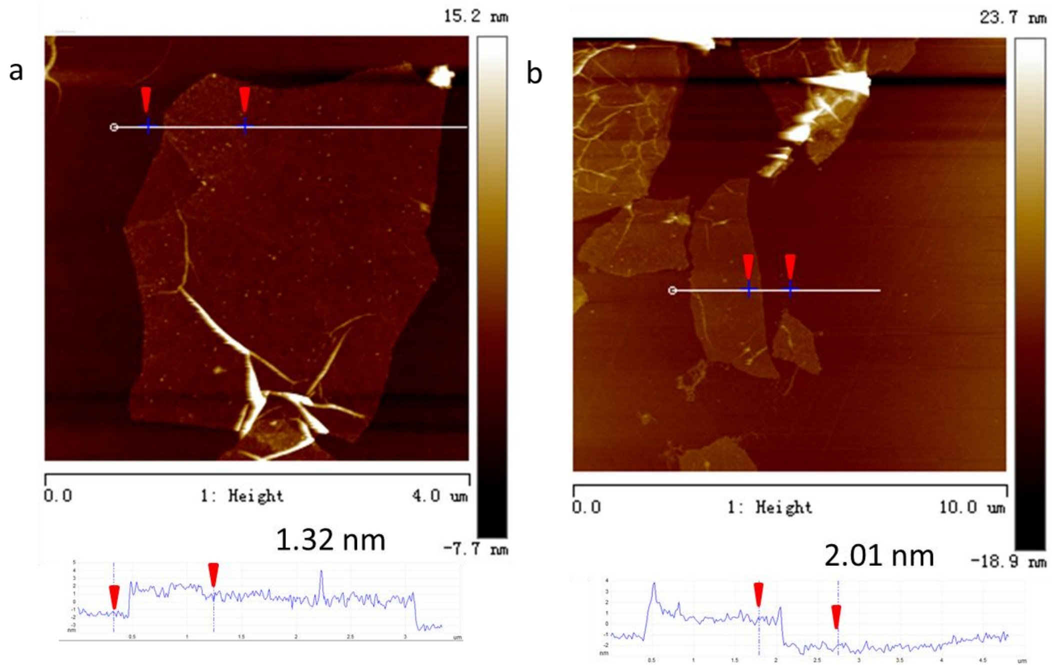

Figure S4 Typical AFM images of (**a**) bilayer and (**b**) trilayer exfoliated graphene.

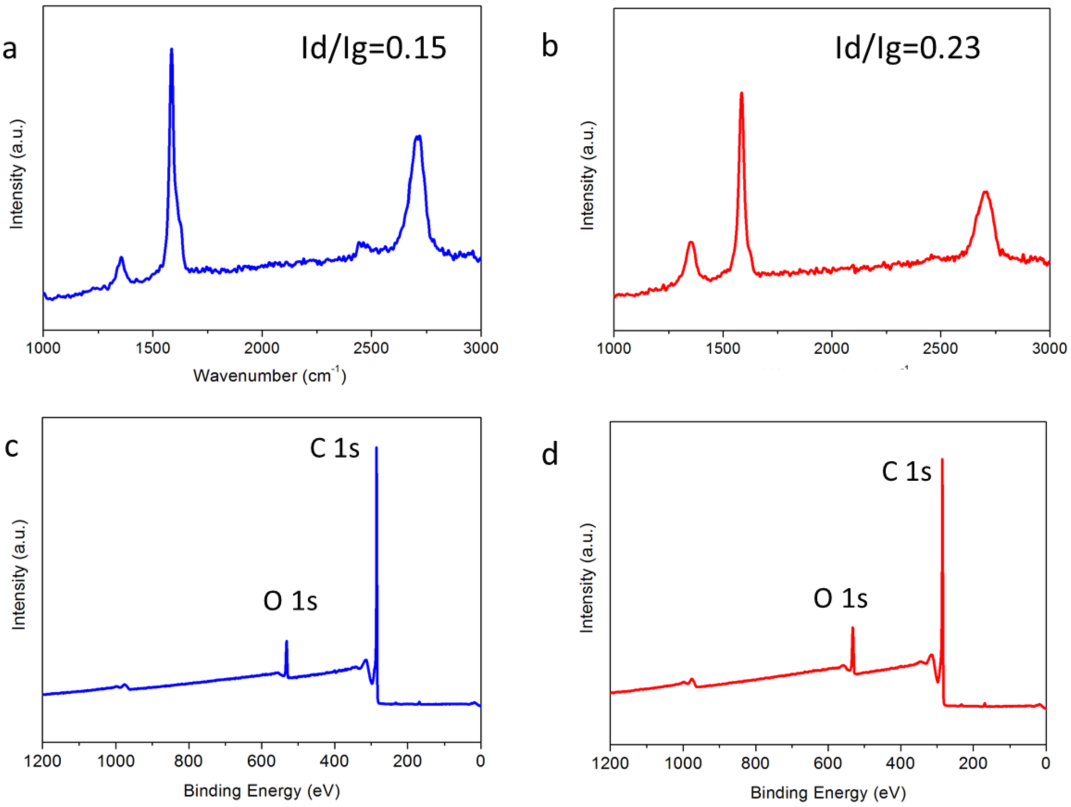

Figure S5 Typical Raman spectra of (a) EG made from sodium borohydride (EG-sodium borohydride) and (b) EG made from ascorbic acid (EG-ascorbic acid), respectively (532 nm laser excitation). XPS survey spectra of (c) EG-sodium borohydride and (d) EG-ascorbic acid.

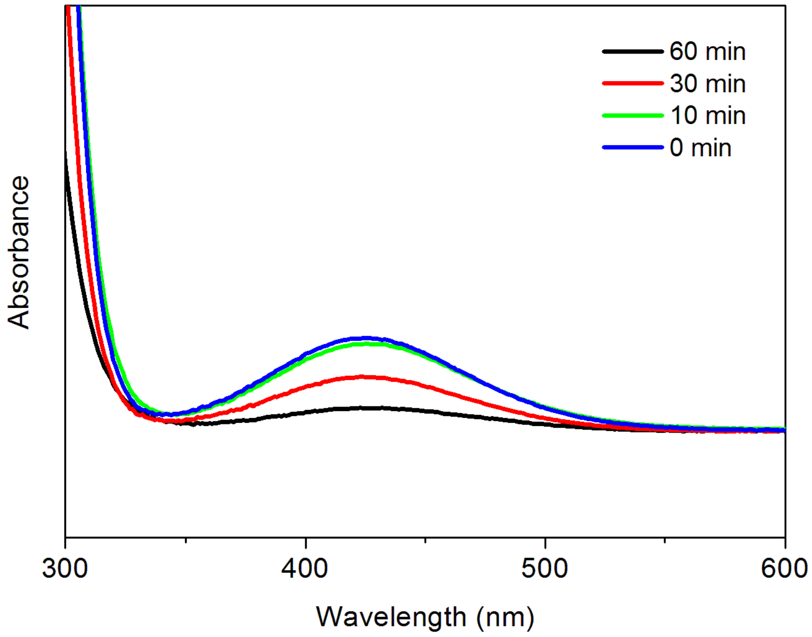

Figure S6 UV-vis spectra of 1 mg mL^{-1} TEMPO in 0.1 M ammonium sulfate aqueous solution after applying a static voltage of 10 V for 0 min, 10 min, 30 min and 60 min (Platinum foils were used as working electrode and counter electrode).

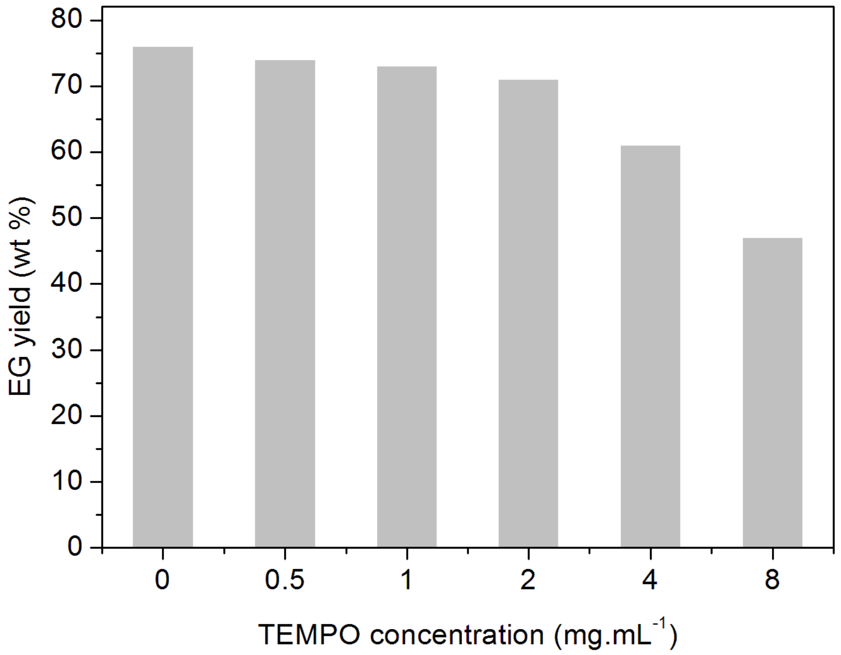

Figure S7 The relationship between exfoliation yield (wt%) and TEMPO concentration.

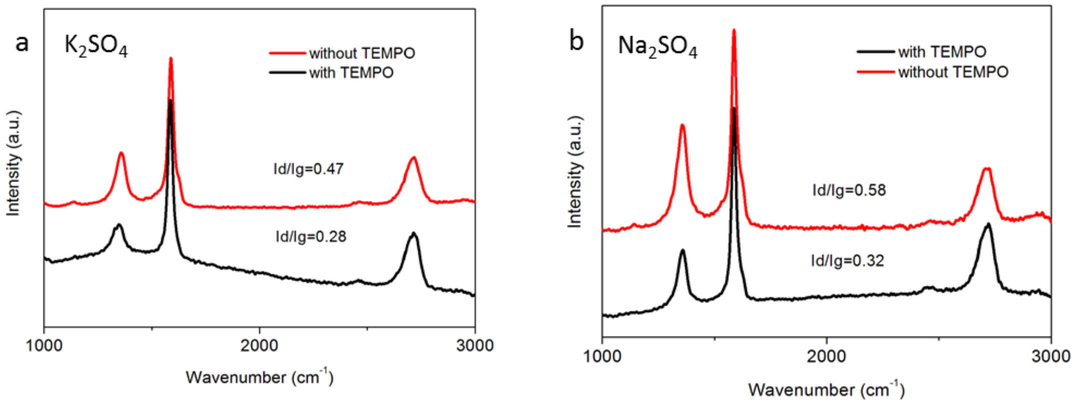

Figure S8 Raman spectra of exfoliated graphene made from aqueous electrolytes with or without the addition of TEMPO. (a) 0.1 M potassium sulfate electrolyte, (b) 0.1 M sodium sulfate electrolyte.

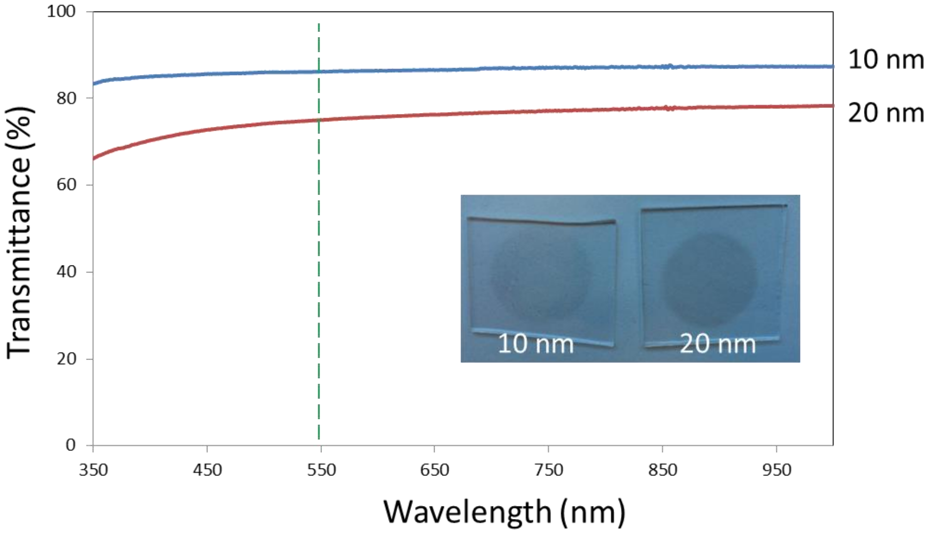

Figure S9 UV spectroscopy of thin EG layers (10 nm and 20 nm) on glass substrates (the inset shows optical pictures of these thin films).

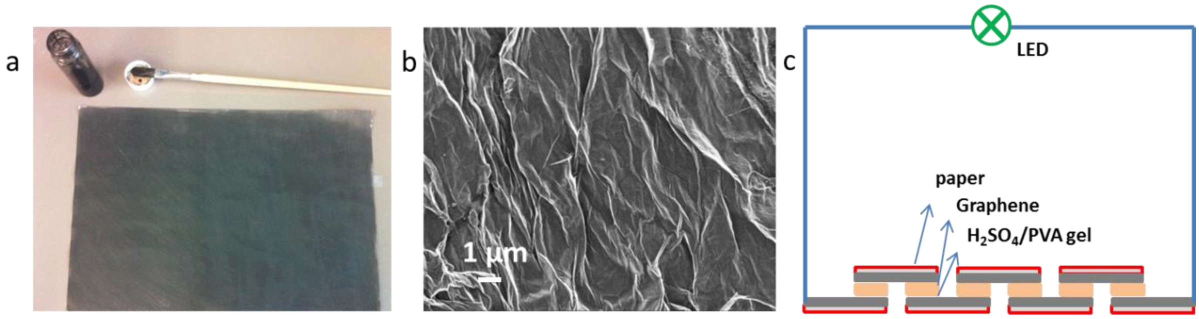

Figure S10 (a) Photographs of graphene ink and a graphene paper after brush-painting. (b) SEM image of a graphene paper. (c) Schematic connection of six graphene paper-based supercapacitors.

Table S1 Summary of the carbon/oxygen ratios of various graphene products

Graphene products	**Approaches**	**C/O ratio**	**Ref**
Reduced graphene oxide (rGO)	Reduce GO with hydrazine hydrate	10.3	*Carbon*, **2007**, *45*, 1558
rGO	Reduce GO with 150 mM $NaBH_4$ solution, 2 h	8.6	*Adv. Funct. Mater.* **2009**, *19*, 1987
rGO	Reduce GO with Vitamin C	12.5	*J. Phys. Chem. C* **2010**, *114*, 6426
rGO	Reduced GO with hydrazine monohydrate (95 ˚C, 3 h)	15.1	*Nanotechnology* **2011**, *22, 055705*
rGO	Reduce GO with 55 % HI solution	14.9	*Carbon* **2010**, *48*, 4466
rGO	Reduce GO in Na/NH_3 system	16.6	*Nat. Commun.* **2013**, *4*, 1539
Exfoliated graphene	Electrochemical exfoliation in 0.1 M H_2SO_4	12.3	*ACS Nano* **2013**, *7*, 3598
Exfoliated graphene	Electrochemical exfoliation in 0.1 M $(NH_4)_2SO_4$	17.2	*J. Am. Chem. Soc.* **2014**, *136*, 6083
Exfoliated graphene	Electrochemical exfoliation in glycine-bisulfate solution	8.8	*Adv. Funct. Mater.* **2015**, *25*, 298
Exfoliated graphene	Electrochemical exfoliation in 0.01 M surfactant (SDS) and 0.15 M Na_2SO_4	6.7 (400 ºC annealed)	*Langmuir* **2013**, *29*, *13307*
Exfoliated graphene	Electrochemical exfoliation in 0.1 M $(NH_4)_2SO_4$ with 1 mg mL^{-1} TEMPO	25.3	This work

Table S2 Summary of the hole mobility values of various graphene sheets

Graphene sheets	**Approaches**	**Hole mobility of sheets ($cm^2\ V^{-1}\ s^{-1}$)**	**Ref**
Reduced graphene oxide (rGO)	Reduced GO by hydrazine vapor	43.5	*Adv. Mater.* **2012** *24*, 2299
rGO	Reduce GO in Na/NH_3 system	123	*Nat. Commun.* **2013** *4*, 1539
rGO	Reduce GO by thermal annealing (1000 °C)	365	*Nano Lett.* **2010**, *10*, 92
Exfoliated graphene	Electrochemical exfoliation in 0.1 M H_2SO_4	233	*ACS Nano* **2013**, *7*, 3598
Exfoliated graphene	Electrochemical exfoliation in H_2SO_4 and KOH mixture	5.5-17	*ACS Nano* **2011**, *5*, 2332
Exfoliated graphene	Electrochemical exfoliation in 0.1 M $(NH_4)_2SO_4$	310	*J. Am. Chem. Soc.* **2014**, *136*, 6083
Exfoliated graphene	Electrochemical exfoliation in 0.1 M $(NH_4)_2SO_4$ with 1 mg mL^{-1} TEMPO	405	This work

Table S3 Comparison of wet-chemical approaches for graphite exfoliation

Methods	**Total yield**	**Yield of 1-3 layer graphene**	**Oxygen content (wt%)**	**C/O ratio**	**I_D/I_G (Raman)**	**Hole Mobility (cm^2 $V^{-1}s^{-1}$)**	**Rs of a single sheet (kΩ/sq)**	**Applications**	**Ref**
Reduced graphene oxide in Na-liquid NH_3	100 %	--	5.6 %	17	>1	123	--	supercapacitor	*Nat. Commun.* **2013**, *4*, 1539.
Reduced graphene oxide with hydrazine	100 %	--	--	--	1.66	43.55	--	Field-effect Transistor	*Adv. Mater.* **2012**, *24*, 2299
Microwave irradiation in ionic liquids	93 %	95 %	3.2 %	30	0.14	--	--	Graphene gel	*Nat. Chem.* **2015**, *7*, 730
Shear exfoliation	< 5 %	--	--	--	0.17-0.37	---	--	Reinforcement of polymer	*Nat. Mater.* **2014**, *13*, 624
Electrochemical Exfoliation (EE) in glycine-bisulfate solution	--	--	11 %	8.8	0.70	--	--	Reduction Catalysis	*Adv. Funct. Mater.* **2015**, *25*, 298
EE in 0.1 M sulfuric acid	~60 %	~80 %	7.5 %	12.3	0.40	233	4.8	Organic Electronics	*ACS Nano* **2013**, *7*, 3598
EE in 0.1 M sulfate salts in water	~75 %	~85 %	5.5 %	17.2	0.25	310	1.96	Flexible film Supercapacitor	*J. Am. Chem. Soc.* **2014**, *136*, 6083
EE in 0.1 M ammonium sulfate with TEMPO	~75 %	~52 %	3.8 %	25.3	< 0.1	405	1.91	Graphene ink Conductive film Supercapacitor	This work

Chapter 3

Ultrafast Delamination of Graphite into High-Quality Graphene Using Alternating Currents

Keywords: Graphene, Electrochemical exfoliation, Lithium-ion battery, Field effect transistor

ToC Graphic

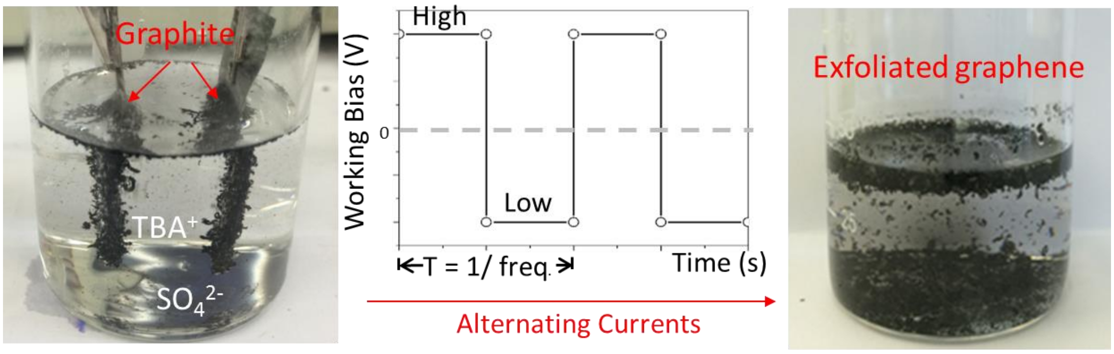

A great alternative: A facile, cost-effective and highly efficient strategy has been developed to delaminate graphite into high-quality graphene by means of alternating currents. This procedure shows great potential to bridge the gap between laboratory-scale research and commercial applications.

Published in:

Angewandte Chemie International Edition

Reprinted with permission from (*Angew. Chem. Int. Ed.*, **2017**, *56*, 6669-6675)

Global progress in graphene research is expected to unlock a new era in the next generation of electronics. However, the development of scalable and cost-effective production of high quality graphene is required in order to offer a commercial prospect to this "wonder material". Thanks to the cheap and abundant graphite resource, graphene can be produced at low cost. The exfoliation of graphite, consequently, represents a reliable strategy to extend the outstanding features of individual graphene flakes to a macroscopic scale.

Graphene layers have been successfully detached from the parent graphite crystal by mechanical force in solid state[1] or in liquid phase.[2] Especially, wet-chemical approaches have been extensively studied because of the ease of synthesis and potential solution processability.[3] The chemical routes (e.g. Hummer's method) allow for the large-scale production of graphene oxide (GO) with high yield of nearly 100 %, based on the weight ratio between dispersed graphitic material to starting graphite flakes.[4] However, even through the use of harsh reduction processes, the residual oxide groups along with diverse structural defects radically affect the electronic features of the reduced GO flakes.[5] Beyond that, liquid–phase sonication of graphite in organic solvents (e.g. *N*-methyl-2-pyrrolidone) provides graphene flakes with much fewer defects.[6] Nevertheless, these methods require long-lasting agitation (e.g. 24 hours), giving low exfoliation yields (less than 1 %) and limited sheet sizes (below 1 μm).[7] Although higher exfoliation yield (~3 %) and production rate (1.44 g h^{-1}) have been achieved by means of shear exfoliation process in liquids,[8] such method remains premature for industrial applications.

Alternatively, when graphite is used as working electrode in an electrochemical cell, an electric current drives the migration of ions or charged molecules into graphite interlayer spacings and pushes graphene layers apart.[9] Electrochemical exfoliation is particularly facile, low-cost, eco-friendly yet efficient.[10] It occurs at either anode (in dilute aqueous solution of ionic liquids,[11] mineral acids[12] or inorganic salts[13]) or cathode (in organic solvents containing lithium salts[14] or quaternary ammonium salts[15]), but not both. Anodic exfoliation gives excellent production rate (exceeding 10 g h^{-1}), thin-layer (e.g. monolayer and bi-/tri-layer) graphene flakes with high yield (~70 %) and large lateral size (5 μm in average).[13a] However, the obtained graphene inevitably contains a certain amount of oxygen groups, resulting from the attack of oxygen-containing radicals (HO·, O·) by water splitting.[12a] On the other hand, cathodic exfoliation, which benefits from reduction potential, guarantees pristine graphene sheets but mainly with thick layers (>5 layers) and relatively low production rate (0.5-2 g h^{-1}),[16] due to insufficient ion intercalation. In spite of the remarkable progress in this field, a well-suited exfoliation method in terms of ultrahigh efficiency, outstanding graphene quality and excellent scalability is still missing.

Herein, we demonstrate a novel scalable exfoliation protocol using alternating current (AC) in aqueous solution of organic sulfate salts, producing high-quality graphene with outstanding yield (~80 %). For the first time, dual intercalation/exfoliation has been achieved at both electrodes simultaneously, enabling ultrahigh production rate (exceeding 20 g h^{-1} in laboratory trials). Over 75 % of thin flakes are 1-3 layer thick and exhibit lateral sizes ranging from 1 to 5 μm. In addition, the switch of voltage polarity facilitates *in-situ* reduction during the exfoliation process, suppresses structural damage and/or residual contamination from anodic oxidation, thereby providing graphene sheets with low defect density (I_D/I_G<0.2 in Raman spectra). Field-effect mobility measured on a single graphene flake is as high as 430 cm^2 V^{-1} s^{-1}. More importantly, exfoliated graphene with excellent solution dispersibility paves the way to fabricating hybrid composites and conductive films. As a proof-of-concept, we demonstrate that graphene-wrapped commercial $LiFePO_4$ particles reveal remarkable cycling stability in lithium-ion battery, delivering a high capacity of 167 mAh g^{-1} at 1 C rate after 500 cycles.

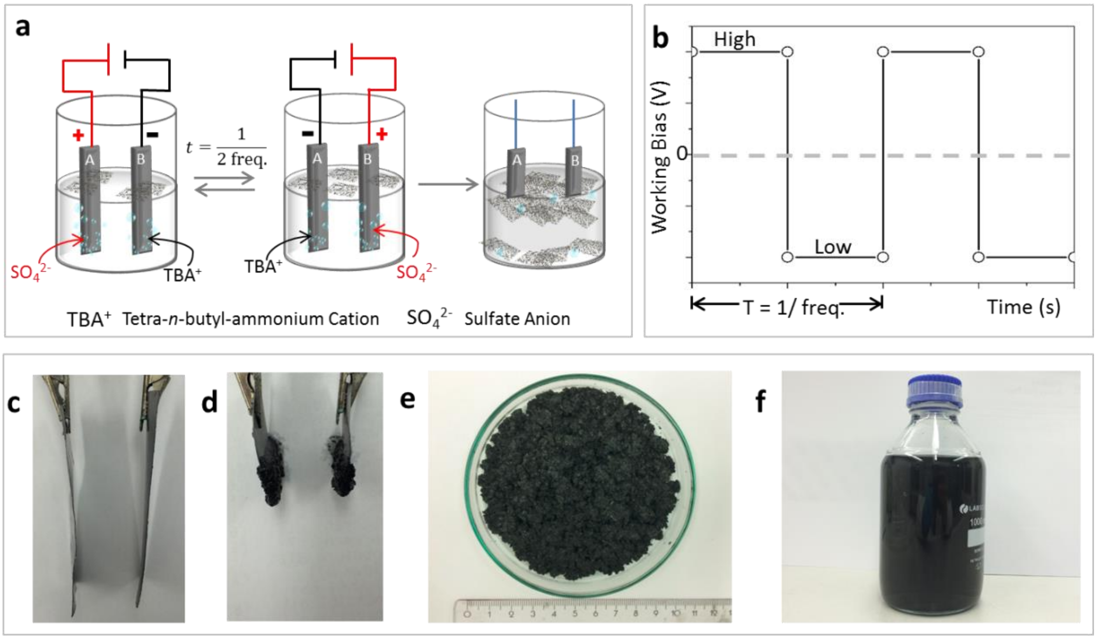

Figure 1. a) Scheme of graphite exfoliation *via* alternating current in aqueous solution of TBA·HSO$_4$; b) The curves of working bias at anode, in which the polarity changes from positive to negative every 0.5 T; c, d) Optical images of graphite foil before and after exfoliation; e) Mass production of EG in 15 min; f) Stable EG dispersion in DMF (0.10 mg mL^{-1}).

The experimental strategy is illustrated in **Figure 1a**. The exfoliation process was conducted in an electrochemical system, consisting of two graphite foils as anode and cathode, tetra-*n*-butyl-ammonium bisulfate (TBA·HSO$_4$) aqueous solution (0.1 M, pH=1.8) as conductive media, respectively. The electrolyte was calibrated with sodium hydroxide (NaOH) solution to nearly neutral condition (pH=6.5).

$HSO_4^- \rightarrow H^+ + SO_4^{2-}$; $HSO_4^- + OH^- \rightarrow H_2O + SO_4^{2-}$

We used a homemade setup to output alternating current with tunable frequency (from 0.01 Hz to 20 Hz) (**Fig. 1b, Fig. S1**). The polarity of voltage was switched every few seconds to facilitate the intercalation of quaternary ammonium cations and sulfate anions into graphite electrodes. Graphite foils at both electrodes dissolved quickly once an alternating current (± 10 V, 0.1 Hz) was applied, accompanied with violent eruption of bubbles. Eventually, graphite foils immersed inside the electrolyte would be entirely exfoliated (**Fig. 1c, 1d**). The suspended exfoliated graphene (EG) flakes on top of the electrolyte were collected by vacuum filtration. Repeated washing with water/ethanol was performed to eliminate the residue salts. To show the potential for large-scale production, five groups of graphite foils (10 pieces) were used in a laboratory trial, producing 5.50 gram EG flakes within 15 min, with a high yield up to 80 % (**Fig. 1e**). The production rate was translated to 22.0 g h^{-1}. It is worth noting that the scalable production of EG relies on the size of graphite foils and the volume of electrochemical cell. The throughput can thus be easily increased to a higher level by setup engineering. Afterwards, graphene sheets were directly dispersed in *N*,*N*-dimethylformamide (DMF) without surfactant stabilization, affording a homogeneous dispersion (0.10 mg mL^{-1}), stable for at least 4 weeks without agglomeration (**Fig. 1f**).

Two types of organic bisulfates (i.e $TBA·HSO_4$ and $TMA·HSO_4$ (tetra-methyl-ammonium bisulfate)) were investigated at ± 10 V with different current frequencies spanning from 0.05 Hz to 0.25 Hz. Although the cationic diameter of TBA^+ (0.83 nm) was larger than that of TMA^+ (0.56 nm),[15] the former ion was found to be more efficient for the exfoliation. The possible explanation is that the flexibility of alkyl groups enables a flattened TBA^+ conformation (0.47 nm, the vertical diameter), the size of which is comparable to the distance of graphitic interlayers (0.33 nm).[17] TBA^+ permits the production of EG with lower oxygen content than that from TMA^+. For example, as shown in **Fig. S2**, when f=0.25 Hz was applied, the resultant EG from TBA^+ exhibited 5.4 atom % oxygen, based on X-ray photoelectron spectroscopy (XPS), whilst EG from TMA^+ delivered much higher oxygen content (10.1 atom %) under the same condition. When f=0.1 Hz was applied, the oxygen level decreased to 7.1 atom % for TMA^+, and 4.5 atom % for TBA^+, respectively. Moreover, the working bias had great impact on the properties of the achieved EG. For example, when it changed from ±6 V to ±12 V at f=0.1 Hz, the concentration of EG dispersion and the defect density of EG (i.e. I_D/I_G ratio by Raman spectroscopy) respectively decreased from 0.20 to 0.08 mg mL^{-1}, and from 0.81 to 0.15 (**Fig. S3**).

Therefore, a moderate potential of ±10 V was applied for graphite exfoliation.

To explore the mechanism of the exfoliation process, we have compared alternating current (AC) with conventional direct current (DC) in the solution of organic bisulfate salt ($TBA \cdot HSO_4$) (**Fig. S4**). When DC was applied, graphite delamination occurred at anode and cathode, however, the efficiency at the cathode was much inferior to that at the anode. By applying an AC, the efficiency at both electrodes was greatly increased, indicating that the working bias had great impact on ion diffusion as well as their intercalation behavior. Despite this, dual exfoliation was not observed in other aqueous electrolytes. For instance, in ammonium sulfate ($(NH_4)_2SO_4$) solution, the exfoliation took place only at the graphite anode. The positively charged counterpart (NH_4^+) did not show any apparent effects at the cathode; thus the overall efficiency could be hardly improved, even upon switching the potential.

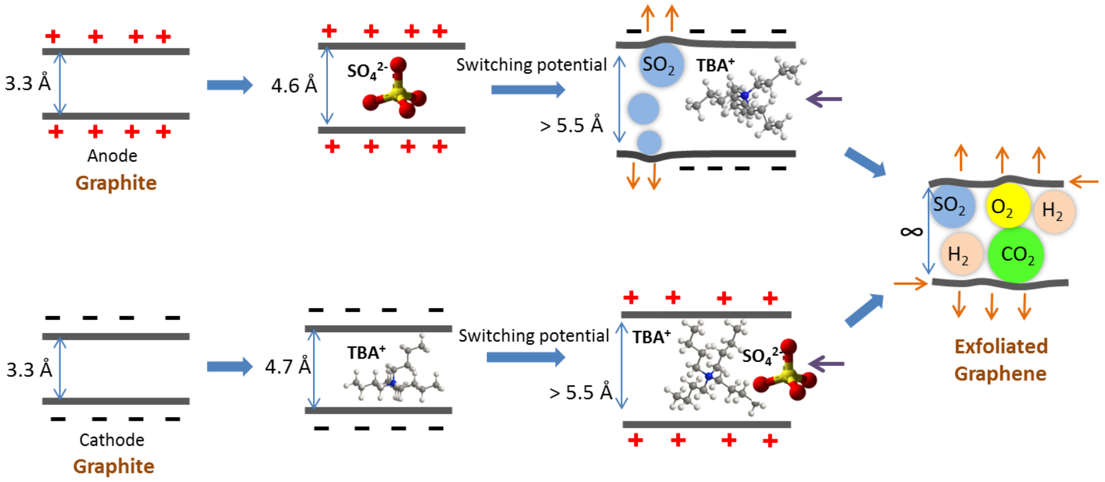

Scheme 1. Proposed mechanism for graphite exfoliation when applied with alternating currents.

Based on the previous studies,[12-13] the intercalation of guest ions expands the interlayer distance of graphite and overcomes van der Waals interaction. It is therefore a significant step in the entire exfoliation process. In the electrochemical cell, the ion intercalation is driven by electric field. By alternating currents, graphite anode and cathode undergo two distinct intercalation routes (**Scheme 1**). We propose:

Since water splitting occurs at a voltage of +1.23 V (*vs.* SCE), initially at the anode, high potential (+10 V) triggers countless oxygen-containing radicals (HO· and O·) at the interface between graphite foil and water:[18]

$H_2O \rightarrow HO\cdot + H^+ + e^- \rightarrow O\cdot + 2\ H^+ + 2\ e^-$

These radicals in turn attack the boundaries or intrinsic defects in graphite, opening the edges, promoting the subsequent intercalation, however, inevitably introducing oxide groups. Afterwards, the migration of sulfate anions causes an increasing *d*-spacing distance (0.46 nm, the diameter of sulfate anion[19]). When the anodic potential switches from positive to negative, the intercalated sulfate anions will be reduced into gas bubbles:

$SO_4^{2-} + 2\ e^- + 4\ H^+ \rightarrow SO_2 + 2\ H_2O$

Gas eruption inside graphite results in large forces,[4] which further increase the distance between two neighbouring layers. Meanwhile, TBA^+ cations are supposed to intercalate inside the graphitic layers.

$TBA^+ + e^- \rightarrow TBA$ (liquid)

Although they do not contribute to the formation of bubbles, the enhanced intercalation of TBA^+ indeed improves the exfoliation yield, owing to its relatively large size (4.7 Å -8.9 Å, varying with its conformation[17]), which helps to overcome the interlayer Van der Waals forces. The force fades quickly once the interlayer distance of graphite exceeds 5.5 Å.[20] More importantly, the negative potential is able to kick out previously attached oxygen-containing functionalities by electrochemical reduction,[21] which is, to a great extent, favourable to improve the quality of exfoliated graphene flakes.

At the cathode side, at the beginning, the intercalation of TBA^+ cations is not as effective as the anodic intercalation of sulfate anions because only the flattened conformation (4.7 Å) is able to accommodate inside graphitic layers. However, when the working bias shifts to positive values, due to the intercalation of sulfate ions, expanded graphite interlayer spacing is able to host tetrahedral conformation of TBA^+

cations, which facilitate a maximum gallery expansion of 8.9 Å.[17]

Once both anode and cathode are expanded to a large extent, the complex electrochemical reactions at the liquid/solid interface generate massive bubbles (O_2, H_2, SO_2, CO_2).[22a] The species of gases have been confirmed by infrared gas analysis (**Fig. S5**). The interplay between chemical reactions and mechanical deformation eventually peels off graphene layers from parent electrodes.[22b]

$2\,H_2O \rightarrow O_2 + 4\,H^+ + 4\,e^-$

$2\,H_2O + 2\,e^- \rightarrow H_2 + 2\,OH^-$

$C_x + 2\,H_2O \rightarrow C_{x-1} + CO_2 + 4\,H^+ + 4\,e^-$

The dissolution of graphite electrodes was confirmed by optical microscopy. In **Fig. S6a**, at a selected area of graphite foil, the exfoliation initiated at the boundaries, spreading to the central parts. The exfoliation speed was very high; apparent cracks at the edges were observed in less than 10 seconds. Within 40 seconds, the majority of graphite foils collapsed and broke down into small pieces. The cross-sectional views from SEM images (**Fig. S6b-S6c**) clearly identified the morphological changes at the graphite anode and cathode separately. In the first 5 seconds, the cathode was less expanded than the anode because the intercalation of TBA^+ cations was not so efficient as that of sulfate anions. From 5 to 10 s, the polarity of electrodes was switched, the subsequent migration of TBA^+ cations and sulfate anions were boosted at the previously activated graphite electrodes, leading to obvious expansion at both cathode and anode. After applying AC for 15 s, graphite foils transformed into loosely-packed layers with porous structure, resulting in exfoliated graphene sheets.

The exfoliated graphene flakes were subsequently transferred onto Si/SiO_2 substrates by the Langmuir-Blodgett method from dispersion. **Figure 2a** shows the scanning electron microscope (SEM) images of EG flakes. The nanosheets, with a broad size distribution, covered uniformly the Si/SiO_2 wafer. Based on the analysis of 100 flakes, over 70 % of the lateral dimensions are between 1 and 5 µm (**Fig. 2b**) and over 10 % of flakes are larger than 5 µm. Statistical analysis on 464 flakes reveals an average flake area of 5.1 µm^2 (**Fig. S7**). Topographical tapping-mode atomic force microscopy (AFM) images provide evidence of thin flakes (**Fig. 2c**). The topographical profile revealed that the thickness of an EG flake amounts to 0.72 nm, which is consistent with the thickness of single-layer graphene on silicon wafer.[23] Interestingly, the height at the flake edge was found to be 0.95 nm, higher than that of the flake basal plane, possibly due to the presence of oxygen moieties. A thickness histogram of 20 randomly selected flakes demonstrates that 75 % of the flakes range from monolayer to trilayers, providing an unambiguous evidence for the highly efficient nature of our exfoliation process (**Fig. 2d**). Selected area electron diffraction (SAED) from transmission electron microscopy (TEM) image (**Fig. 2e**) exhibits a typical hexagonal symmetric pattern. The diffraction at the (210) plane is stronger than that at the (110) plane, suggesting a bilayer graphene flake with high crystallinity.[24] A representative Raman spectrum (**Fig. 2f**, excited by a 532 nm laser) was collected from the central

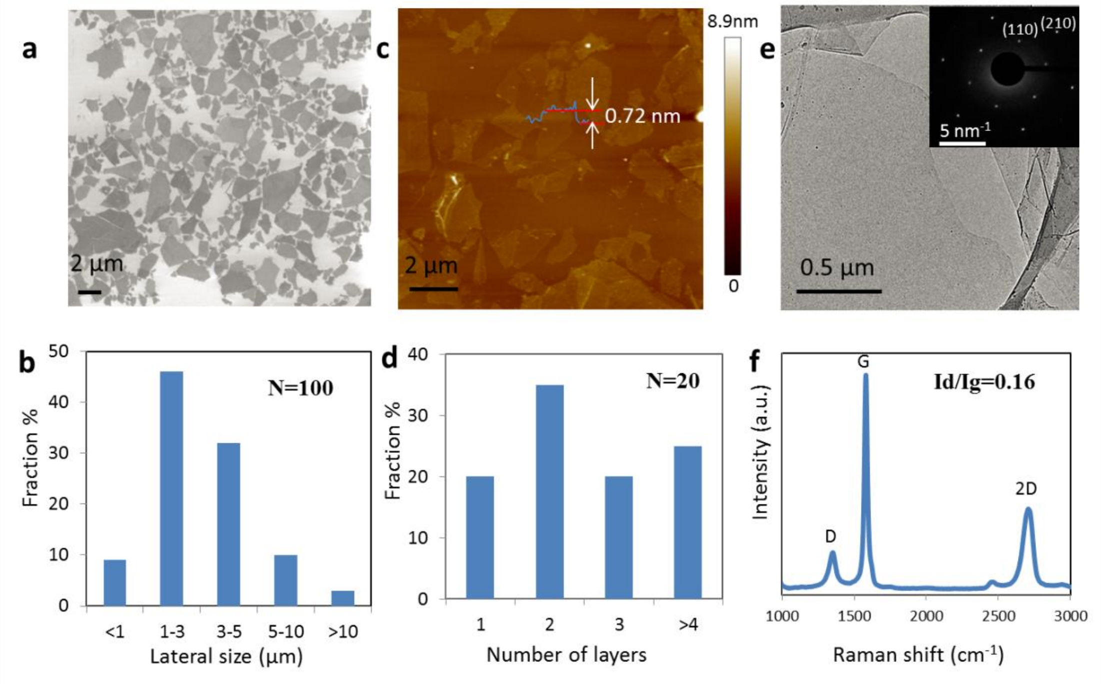

Figure 2. a) SEM image of EG sheets on Si/SiO$_2$ wafer; b) statistical calculation of flake sizes from SEM image; c,d) AFM image of EG flakes and the corresponding height profile distribution; e) TEM image of a EG flake and its SAED pattern; f) Raman spectrum of EG (excited by 532 nm laser).

part of an EG flake. It exhibits three major bands, including D band at 1350 cm^{-1}, G band at 1580 cm^{-1} and a symmetric 2D band at 2700 cm^{-1}, in which the D band was caused by defects (boundaries or functional groups). The low value of I_D/I_G ratio (0.16) reveals a low level of disorders or defects at in-plane region of EG sheets. This value is much smaller than that of graphene materials based on GO (generally exceeding 1)[25] and anodic exfoliated graphene from aqueous electrolytes (0.25-0.95).[12-13]

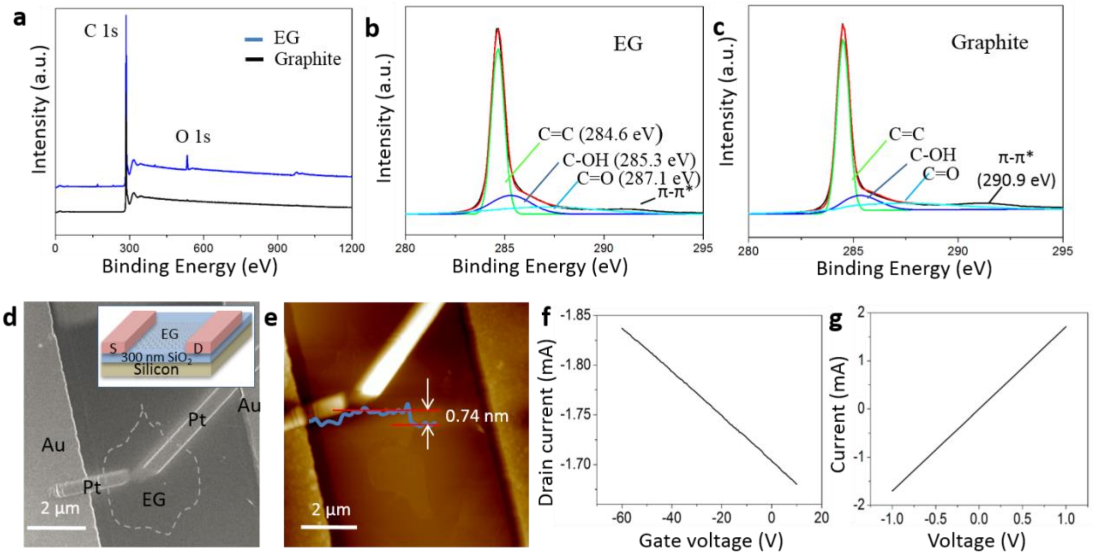

Figure 3. a) XPS survey of EG powder and graphite foil; High resolution C1s spectrum of (b) EG and (c) graphite, respectively; d,e) SEM (insert: geometry) and AFM of fabricated FET device; f) Transfer curve and g) current-voltage (*I*-*V*) curve of a monolayer EG flake.

X-ray photoelectron spectroscopy (XPS) and Elemental analysis (EA) were performed to reveal the chemical composition of EG (**Fig. 3a-3c, Table S1**). Based on results from XPS, the oxygen content of the EG powder was evaluated to be 4.5 atom %, thus being higher than that of the graphite precursor (1.8 atom % oxygen). Electrochemical exfoliation usually introduces oxygen to the edges and grain boundaries of EG flakes, mainly in the form of hydroxyl and epoxy groups.[13a] The atomic ratio of carbon and oxygen (C/O) in this work is calculated to be 21.2, which is higher than our previous reports,[12b, 13a] The high-resolution C 1s peak is fitted into three peaks at 284.6 eV, 285.3 eV and 287.1 eV, corresponding to the C=C, C-OH, C=O bonds, respectively.[26] The peak related to the π-π* transition (shake-up) (290.9 eV) is well visible after exfoliation, indicating that the conjugated aromatic structure is preserved.[27] Epoxy groups (C-O-C) and carboxyl groups (-C(O)-O) are absent, most possibly due to the electrochemical reduction in the exfoliation process[28] (the conversion reactions are proposed in **Fig. S8**). As an important benefit, the periodically switched potential indeed helps to protect EG against excessive oxidation by introducing destructive epoxy groups.

Field-effect transistor (FET) devices were fabricated to reveal the electronic property of EG. **Figure 3d** reports the SEM image of as-prepared FET device on the Si/SiO_2 wafer. The isolated EG flake in the channel is connected by a lithographed Pt wire to gold source/drain electrodes. AFM and thickness analysis (**Fig. 3e**) confirm a monolayer flake. According to the transfer curve (**Fig. 3f**) and I-V curve (**Fig. 3g**), the individual EG sheet possesses a remarkably high hole mobility of 430 cm^2 V^{-1} s^{-1} and a sheet resistance of 1.98 kΩ sq^{-1}. In addition, EG flakes with various thickness have been examined (**Table S2**). Thanks to fast exfoliation as well as electrochemical reduction, the average hole mobility based on a single EG flake in this work is obviously higher than that of chemically reduced GO (0.001-123 cm^2 V^{-1} s^{-1})[29] and electrochemically exfoliated graphene by direct current (233-405 cm^2 V^{-1} s^{-1})[12b, 13] (**Table S3**). Moreover, profiting from the excellent solution-processability of EG, a graphene thin film on a glass substrate was prepared by a simple filtration-transfer method. Graphene film with 10 nm thickness provides a low mean sheet resistance of 1.56 kΩ sq^{-1} (with conductivity of 640 S cm^{-1}). After doping by nitric acid (65 %) at ambient condition, the value further drops down to 0.92 kΩ sq^{-1} (with conductivity of 1087 S cm^{-1}). This value is much lower than that of reduced GO film (3.2 kΩ sq^{-1}) at similar thickness.[30] Combined with good processability in solutions, the exfoliated graphene has shown promising applications such as transparent conductive electrodes in optoelectronics.[31]

To illustrate the potential use of the developed EG in batteries, we simply mixed an EG dispersion with commercially available cathode material (lithium iron phosphate, $LiFePO_4$) in DMF under a sonication bath. The surface of $LiFePO_4$ particles was homogeneously coated with a thin layer of EG (**Fig. S9**). After filtration, EG-wrapped $LiFePO_4$ particles (EG-LFP) with low mass loading of EG (2.0 wt%) were used as cathode in half-cells, in which a lithium foil was assembled as the anode. The voltage profile of EG-LFP with 1 C (1 C=170 mA g^{-1}) (**Fig. 4a**) revealed a capacity of

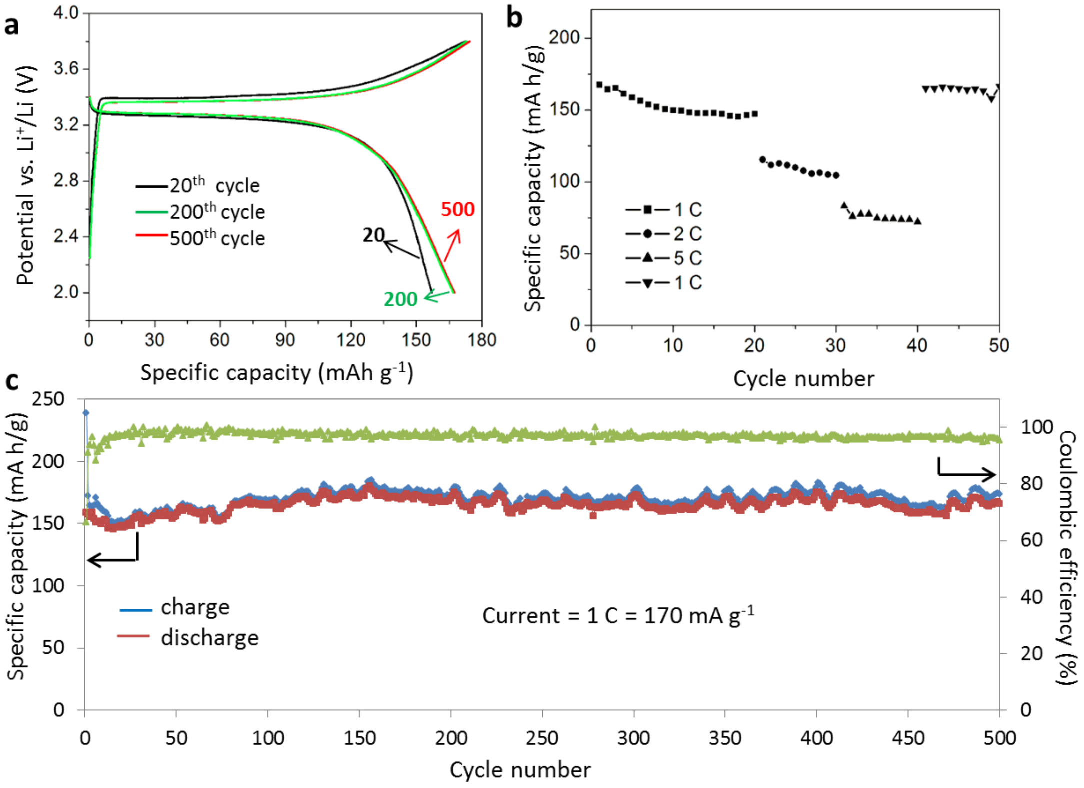

Figure 4. a) The voltage profile for the 20th, 200th and 500th cycle of charging and discharging (at a current rate of 1 C) of EG-$LiFePO_4$ hybrid; b) the discharge rate capability at various charge/discharge rates; c) cycling performance of EG-$LiFePO_4$ hybrid upon prolonged 500 cycles and its Coulombic efficiency at 1 C.

157 mAh g^{-1} at the 20th cycle. After the activation of active material ($LiFePO_4$ = $FePO_4$ + Li^+ + e^-),[32] the capacity was further increased to 167 mAh g^{-1} at 200th cycle, which was stable till the 500th cycle. **Fig. 4b** shows the discharge rate capability at

different charging/discharging rates ranging from 1 C to 5 C. The capacity faded at a high discharging current, however, ~50 % of capacity was still retained at 5 C. Once the discharging rate reverted to 1 C, the capacity of EG-LFP was reached again at ~165 mAh g^{-1}. In particular, EG-LFP demonstrated excellent cycling stability at 1 C rate (**Fig. 4c**). The average Coulombic efficiency was calculated to be 99.3 %. A high discharging capacity of 167 mAh g^{-1} was obtained after 500 cycles. This value is approaching the theoretical capacity of $LiFePO_4$ (170 mAh g^{-1}). The superior performance of EG-LFP results from high-quality graphene, which significantly improves the electron transfer during the cycling process, even though a very low weight percentage of graphene (2.0 wt%) has been used. In contrast, other methods to coat $LiFePO_4$ particles, such as atomic carbon layer depositing[33] and core-shell carbon encapsulation,[34] generally need expensive equipments or multiple synthetic steps but enable similar cycling capacities (150-168 mAh g^{-1}).

In summary, we have developed a facile, simple and fast strategy to exfoliate graphite by alternating current to achieve high exfoliation efficiency (80 % total yield, 75 % of the graphene are 1-3 layers) and ultrahigh production capacity (over 20 gram per hour in a lab test). The exfoliated graphene owns large flakes, low degree of defects and a remarkable hole mobility up to 430 $cm^2 V^{-1} s^{-1}$. This straightforward method provides EG dispersion with excellent processability, which is favourable for the fabrication of conducting films and integrated hybrids. The high-quality solution-processable EG also holds great promise for a wide spectrum of applications, such as inkjet printing, solar cells, catalysis and composites.

Experimental Section

Details of experiments including graphene synthesis, device fabrication and additional characterization are listed in supporting information.

Acknowledgements

The authors gratefully acknowledge financial support by ERC Grant on 2D MATER and UPGreen, EC under Graphene Flagship (No. CNECT-ICT-604391). The Marie Sklodowska-Curie ETN projects SYNCHRONICS (GA 643238), the Agence Nationale de la Recherche through the LabEx project Chemistry of Complex Systems (ANR-10-LABX-0026_CSC), and the International Center for Frontier Research in Chemistry (icFRC). The authors thank Dr. [redacted] and Dr. [redacted] (Lebniz Institute for Solid State and Materials Research) for insightful discussions; Dr. [redacted] (Fraunhofer-Institut für Werkstoff- und Strahltechnik) and [redacted] (TU Dresden) for FT-IR gas analysis. [redacted] would like to acknowledge financial support from China Scholarship Council (CSC).

Reference

[1] a) K. S. Novoselov, A. K. Geim, S. V. Morozov, D. Jiang, Y. Zhang, S. V. Dubonos, I. V. Grigorieva, A. A. Firsov, *Science* **2004**, *306*, 666-669; b) V. Leon, M. Quintana, M. A. Herrero, J. L. G. Fierro, A. d. l. Hoz, M. Prato, E. Vazquez, *Chem. Commun.* **2011**, *47*, 10936-10938.

[2] a) Z. Y. Xia, S. Pezzini, E. Treossi, G. Giambastiani, F. Corticelli, V. Morandi, A. Zanelli, V. Bellani, V. Palermo, *Adv. Funct. Mater.* **2013**, *23*, 4684-4693; b) A. Ciesielski, P. Samori, *Chem. Soc. Rev.* **2014**, *43*, 381-398.

[3] D. Voiry, J. Yang, J. Kupferberg, R. Fullon, C. Lee, H. Y. Jeong, H. S. Shin, M. Chhowalla, *Science* **2016**, *353*, 1413-1416.

[4] A. M. Dimiev, G. Ceriotti, A. Metzger, N. D. Kim, J. M. Tour, *ACS Nano* **2016**, *10*, 274-279.

[5] C. Gómez-Navarro, R. T. Weitz, A. M. Bittner, M. Scolari, A. Mews, M. Burghard, K. Kern, *Nano Lett.* **2007**, *7*, 3499-3503.

[6] a) F. Bonaccorso, A. Bartolotta, J. N. Coleman, C. Backes, *Adv. Mater.* **2016**, *28*, 6136-6166; b) A. Ciesielski, S. Haar, M. El Gemayel, H. Yang, J. Clough, G. Melinte, M. Gobbi, E. Orgiu, M. V. Nardi, G. Ligorio, V. Palermo, N. Koch, O. Ersen, C. Casiraghi, P. Samorì, *Angew. Chem. Int. Ed.* **2014**, *53*, 10355-10361.

[7] J. N. Coleman, *Acc. Chem. Res.* **2013**, *46*, 14-22.

[8] K. R. Paton, E. Varrla, C. Backes, R. J. Smith, U. Khan, A. O’Neill, C. Boland, M. Lotya, O. M. Istrate, P. King, T. Higgins, S. Barwich, P. May, P. Puczkarski, I. Ahmed, M. Moebius, H. Pettersson, E. Long, J. Coelho, S. E. O’Brien, E. K. McGuire, B. M. Sanchez, G. S. Duesberg, N. McEvoy, T. J. Pennycook, C. Downing, A. Crossley, V. Nicolosi, J. N. Coleman, *Nat. Mater.* **2014**, *13*, 624-630.

[9] C. T. J. Low, F. C. Walsh, M. H. Chakrabarti, M. A. Hashim, M. A. Hussain, *Carbon* **2013**, *54*, 1-21.

[10] S. Yang, M. R. Lohe, K. Müllen, X. Feng, *Adv. Mater.* **2016**, *28*, 6213-6221.

[11] X. Wang, P. F. Fulvio, G. A. Baker, G. M. Veith, R. R. Unocic, S. M. Mahurin, M. Chi, S. Dai, *Chem. Commun.* **2010**, *46*, 4487-4489.

[12] a) K. S. Rao, J. Sentilnathan, H.-W. Cho, J.-J. Wu, M. Yoshimura, *Adv. Funct. Mater.* **2015**, *25*, 298-305; b) K. Parvez, R. Li, S. R. Puniredd, Y. Hernandez, F. Hinkel, S. Wang, X. Feng, K. Müllen, *ACS Nano* **2013**, *7*, 3598-3606.

[13] a) K. Parvez, Z.-S. Wu, R. Li, X. Liu, R. Graf, X. Feng, K. Müllen, *J. Am. Chem. Soc.* **2014**, *136*, 6083-6091; b) S. Yang, S. Brüller, Z.-S. Wu, Z. Liu, K. Parvez, R. Dong, F. Richard, P. Samorì, X. Feng, K. Müllen, *J. Am. Chem. Soc.* **2015**, *137*, 13927-13932.

[14] Z. Zeng, Z. Yin, X. Huang, H. Li, Q. He, G. Lu, F. Boey, H. Zhang, *Angew. Chem. Int. Ed.* **2011**, *50*, 11093-11097.

[15] A. J. Cooper, N. R. Wilson, I. A. Kinloch, R. A. W. Dryfe, *Carbon* **2014**, *66*, 340-350.

[16] A. M. Abdelkader, I. A. Kinloch, R. A. W. Dryfe, *ACS Appl. Mater. Interfaces* **2014**, *6*, 1632-1639.

[17] W. Sirisaksoontorn, A. A. Adenuga, V. T. Remcho, M. M. Lerner, *J. Am. Chem. Soc.* **2011**, *133*, 12436-12438.

[18] X. Feng, X. Wang, W. Cai, S. Qiu, Y. Hu, K. M. Liew, *ACS Appl. Mater. Interfaces* **2016**, *8*, 25552-25562.

[19] M. K. Punith Kumar, M. Nidhi, C. Srivastava, *RSC Adv.* **2015**, *5*, 24846-24852.

[20] L. A. Girifalco, M. Hodak, *Phys. Rev. B* **2002**, *65*, 125404.

[21] X. Wang, I. Kholmanov, H. Chou, R. S. Ruoff, *ACS Nano* **2015**, *9*, 8737-8743.

[22] a) C.-Y. Yang, C.-L. Wu, Y.-H. Lin, L.-H. Tsai, Y.-C. Chi, J.-H. Chang, C.-I. Wu, H.-K. Tsai, D.-P. Tsai, G.-R. Lin, *Opt. Mater. Express* **2013**, *3*, 1893-1905; b) Z. Y. Xia, G. Giambastiani, C. Christodoulou, M. V. Nardi, N. Koch, E. Treossi, V. Bellani, S. Pezzini, F. Corticelli, V. Morandi, A. Zanelli, V. Palermo, *ChemPlusChem*, **2014**, *79*, 439-446.

[23] Z. Cheng, Q. Zhou, C. Wang, Q. Li, C. Wang, Y. Fang, *Nano Lett.* **2011**, *11*,

767-771.

[24] Z. Sun, Z. Yan, J. Yao, E. Beitler, Y. Zhu, J. M. Tour, *Nature* **2010**, *468*, 549-552.

[25] I. K. Moon, J. Lee, R. S. Ruoff, H. Lee, *Nat. Commun.* **2010**, *1*, 73.

[26] M. Matsumoto, Y. Saito, C. Park, T. Fukushima, T. Aida, *Nat. Chem.* **2015**, *7*, 730-736.

[27] A. Ganguly, S. Sharma, P. Papakonstantinou, J. Hamilton, *J. Phys. Chem. C* **2011**, *115*, 17009-17019.

[28] K. Hu, X. Xie, T. Szkopek, M. Cerruti, *Chem. Mater.* **2016**, *28*, 1756-1768.

[29] a) G. Eda, G. Fanchini, M. Chhowalla, *Nat. Nanotech.* **2008**, *3*, 270-274; b) H. Feng, R. Cheng, X. Zhao, X. Duan, J. Li, *Nat. Commun.* **2013**, *4*, 1539.

[30] Z. Yin, S. Sun, T. Salim, S. Wu, X. Huang, Q. He, Y. Lam, H. Zhang, *ACS nano.* **2010**, *4*, 5263-5268.

[31] A. G. Ricciardulli, S. Yang, X. Feng, P. Blom, *ACS Appl. Mater. Interfaces*, **2017**, *9*, 25412-25417.

[32] B. Lung-Hao Hu, F.-Y. Wu, C.-T. Lin, A. N. Khlobystov, L.-J. Li, *Nat. Commun.* **2013**, *4*, 1687.

[33] J. Liu, M. N. Banis, Q. Sun, A. Lushington, R. Li, T-K Sham, X. Sun, *Adv. Mater.* **2014**, *26*, 6472-6477.

[34] S. H. Ha, Y. J. Lee, *Chem. Eur. J.* **2015**, *21*, 2132-2138.

Supporting Information

Ultrafast Delamination of Graphite into High-Quality Graphene Using Alternating Currents

Experimental Section

Graphite Exfoliation. Graphite exfoliation was carried out in a two-electrode system, in which two graphite foils (Alfa Aesar) were used as cathode and anode, respectively. The electrodes were placed in parallel at a fixed distance of 1.5 cm. The electrolyte was prepared by dissolving tetrabutylammonium hydrogensulfate powders (0.005 M, 1.70 g) in 50 mL deionized water. The pH value of the electrolyte was tuned by NaOH solution to nearly 7. An alternating current (±10 V, 0.1 Hz) was used to trigger the exfoliation process, in which anodic working bias switches every 5 seconds from positive (+10 V) to negative (-10 V), and vice versa. To avoid over-heat in the electrolyte, the reactor was put inside an ice bath during the entire exfoliation procedure. For large-scale production, five groups of graphite foils (anode and cathode) were connected alternatively in a row. Once the exfoliation finished, the suspended exfoliated graphene (EG) were collected with a 0.2 μm PTFE membrane filter and washed 3 times by water and 3 times by ethanol to remove any chemical residues. Afterwards, the wet graphene powder was dispersed in *N*,*N*-dimethylformamide (DMF) via mild sonication (30 min, in an ice bath). The un-exfoliated flakes and large particles were eliminated by centrifugation (3000 rpm, 10 min). Then, the supernatant was taken out for further measurement and ultimately device fabrication.

Instrumentation. The morphology of graphene was obtained using scanning electron microscope (SEM, Zeiss Gemini 500), transmission electron microscopy (TEM, Zeiss

Libra 120 kV). AFM characterization was carried out with Veeco Nanoscope-IIIa Multimode Tuna (Digital Instruments). Raman spectroscopy was performed with a Bruker RFS 100/S spectrometer (laser wavelength 532 nm). Elemental analysis was made by a EuroEA Elemental Analyser. XPS analyses were carried out on a Thermo Scientific K-Alpha X-ray photoelectron spectrometer with a basic chamber pressure of between ~10^{-8}–10^{-9} mbar and with an Al anode as the X-ray source (x-ray radiation of 1486.7 eV). Spot sizes of 400 μm were used. Survey spectra were recorded with an average of 10 scans, a pass energy of 200.00 eV and a step size of 1 eV. High-resolution spectra were taken with an average of 10 scans with a pass energy of 50.00 eV and a step size of 0.1 eV. The sheet resistances (R_s) of the EG films were measured with a four-point probe system using a Keithley 2700 multimeter (probe spacing: 0.635 mm, R_s=4.532 V/I).

Devices for Field Effect Transistor (FET). EG flakes for FET measurements were transferred using the Langmuir-Blodgett (LB) assembly method. Deionized water was used as the supporting sub-phase. The mixed solution contains 1.0 mL EG dispersion (in DMF) and 3 mL chloroform (HPLC grade) was carefully dropped onto the water surface using a glass syringe. A small piece of filter paper was used to monitor the surface pressure during the compression of the EG film on the water interface. The target surface tension was set to 20 mN m^{-1}. By vertical dip-coating, an EG thin film was transferred onto a Si/SiO$_2$ wafer (with an oxide layer of 300 nm). The samples were carefully washed with DI water, and annealed at 200 °C for 30 min under vacuum to remove any residual solvents. To make single EG flake-based FETs, a thin platinum layer (100 nm) was deposited by focused ion beam lithography to connect the isolated flakes to the Au source/drain electrodes. The hole carrier mobility was calculated from the linear regime of the transfer curves with this equation:

$$\mu = \frac{L}{WC_iV_d} \times \frac{\Delta I_d}{\Delta V_g}$$

(where C_i is the dielectric capacitance, L and W are the channel length and width between source/drain electrode, respectively).

The sheet resistance of a single EG sheet was obtained on the same device, and the value was calculated using the following equation:

$$R_s = R \bullet \frac{W}{L}$$

(where *R* is the resistance at 0.5 V, *L* and *W* are the channel length and width between source/drain electrode, respectively).

All of the device tests were carried out inside a glove box filled with inert gas using a Keithley SCS 4200 semiconductor system.

Graphene-$LiFePO_4$ hybrids for lithium-ion batteries. $LiFePO_4$ powder (20 mg, particle size < 5 µm, Sigma Aldrich) was grinded for 30 min and suspended in DMF (40 mL) by sonication (1 hour) to give a homogeneous dispersion, then mixed with 8 mL of dilute graphene dispersion (0.05 mg mL^{-1}, in DMF), kept sonication for additional 2 hours. Graphene-wrapped $LiFePO_4$ (EG-LFP) was collected by filtration and dried overnight in vacuum oven (100 ^{o}C) to avoid solvent contamination.

EG-LFP working electrode was prepared by mixing active hybrid material, carbon black (super-P) and polyvinylidene difluoride (PVDF) at a weight ratio of 80:10:10, and coated on an aluminium foil. The pasted foil was dried and punched into dish with diameter of 10 mm, and were further dried at 80 ^{o}C under vacuum (12 h). Coin cells (CR2032 type) were assembled in an argon-filled glove box (O_2<0.1 ppm, H_2O<0.1 ppm) with lithium foil (Sigma Aldrich) as counter electrode and polypropylene as separator. The electrolyte was made of 1 M $LiPF_6$ in ethylene carbonate (EC)/diethyl carbonate (DEC) (3:7 v/v, with 2 wt% vinylene carbonate). All the galvanostatic charge/dischange curves and cycles were tested by a LAND battery system at ambient condition.

Figure S1 Home-made low-frequency generator as power supply for graphite exfoliation. The output voltage can be tuned from -12 V to 12 V, frequency from 0.01 Hz to 20 Hz.

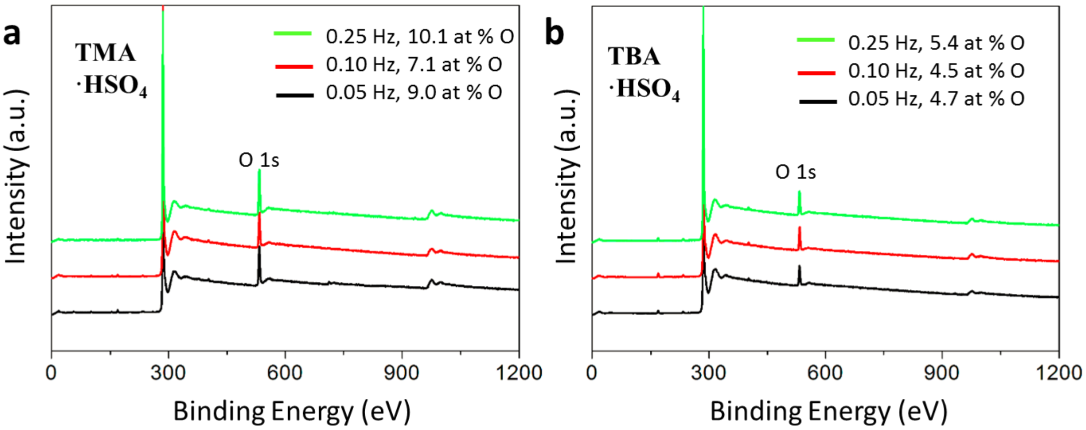

Figure S2 XPS survey of EG powders from alternating current-assisted exfoliation in aqueous solutions of (a) TMA·HSO_4 and (b) TBA·HSO_4. The frequency varies from 0.05 Hz to 0.25 Hz. The working bias is fixed at ±10 V and the concentration of the electrolyte is 0.1 M.

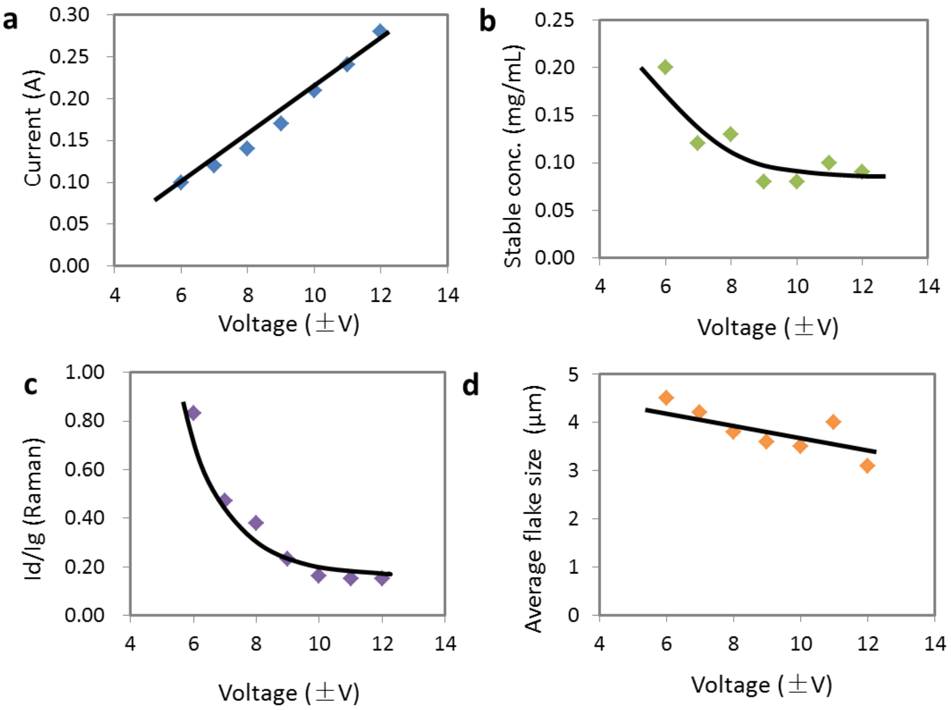

Figure S3 The optimized conditions for graphite exfoliation in solution of TBA·HSO_4 (0.1 M). (a) The current, (b) concentration of stable EG dispersion, (c) the I_d/I_g ratio in Raman spectra, (d) the average flake sizes of EG change as a function of working bias from ±6 V to ±12 V. The current frequency is fixed at 0.1 Hz.

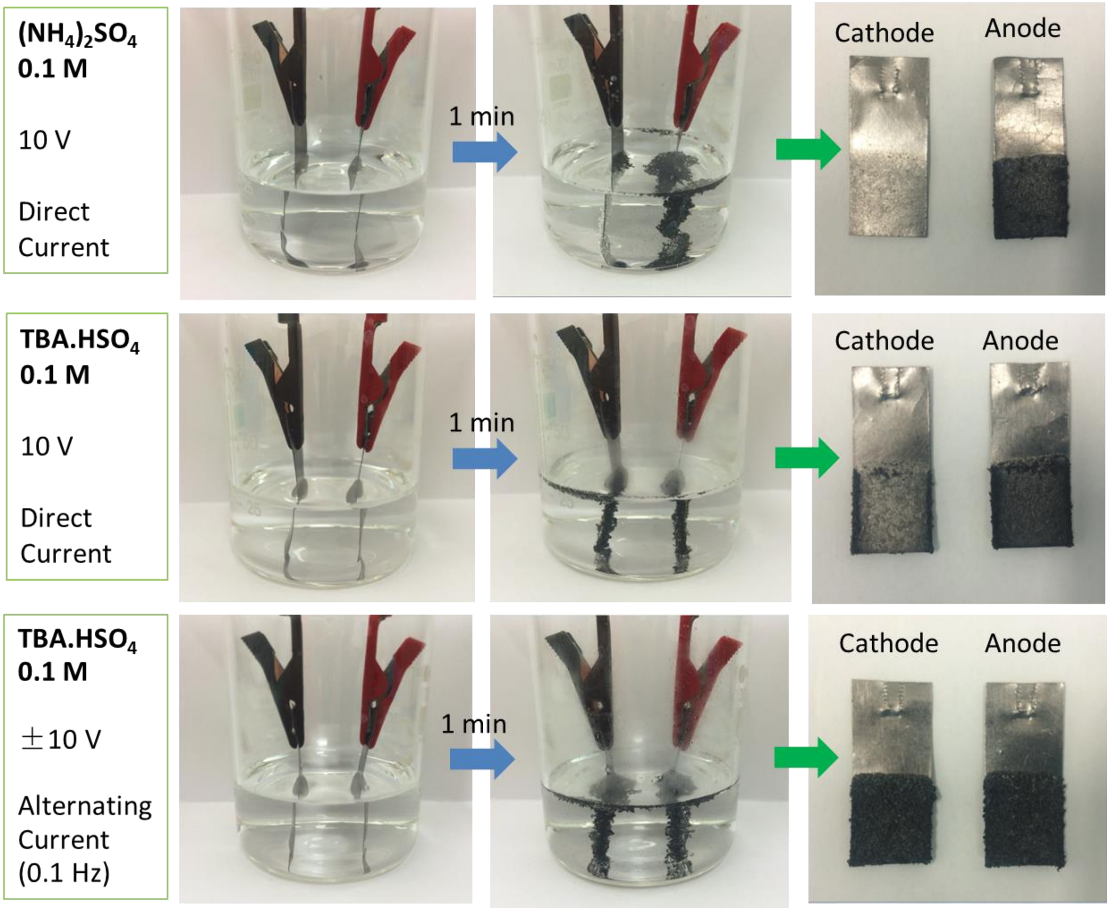

Figure S4 Graphite exfoliation in aqueous solution of inorganic (ammonium) sulfate and organic (TBA) sulfate salts.

Graphite foils serve as anode and cathode in all experiments.

When applying a direct current, graphite exfoliation is observed only at anode in ammonium sulfate solution due to the intercalation of SO_4^{2-} anions. However, both electrodes are expended in the solution of tetra-*n*-butylammonium hydrogensulfate (TBA·HSO_4), corresponding to the intercalation of TBA^+ cations and SO_4^{2-} anions. According to the images, the exfoliation at cathode seems less efficient than that at anode.

In the presence of TBA·HSO_4, alternating currents are able to boost exfoliation at both electrode, as described in the pictures.

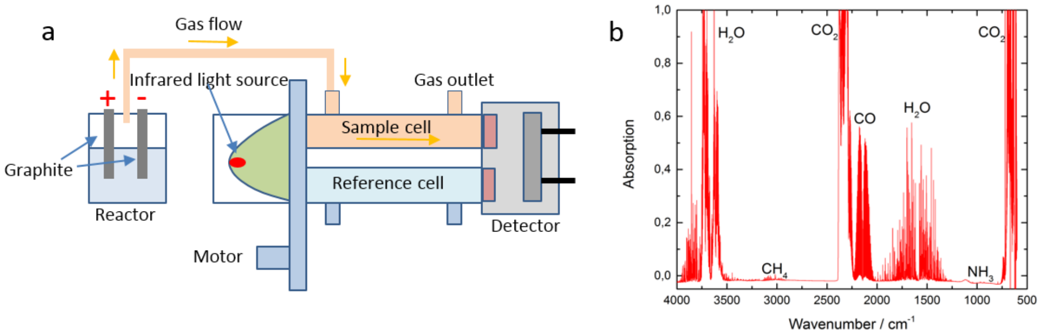

Figure S5 (a) Infrared gas analyzer used to measure the evolved gas from electrochemical cell; (b) IR spectrum of gases present during exfoliation process.

CO_2 and CO were visible in IR spectrum. Since H_2 and O_2 did not have dipole moments, they were not detectable in this system. However, they were surely evolved from water splitting once a high working bias of 10 V was applied. SO_2 was absent in the spectrum, possibly due to its high solubility in water. Additional experiments using a piece of moist universal indicator paper were performed to confirm its presence. Trace amount of CH_4 and NH_3 were also notable, as a result of side reactions. The gas evolution from other electrolytes, such as sulfuric acid and inorganic sulfate solution, showed similar results that CO_2 and CO were the major gas species.

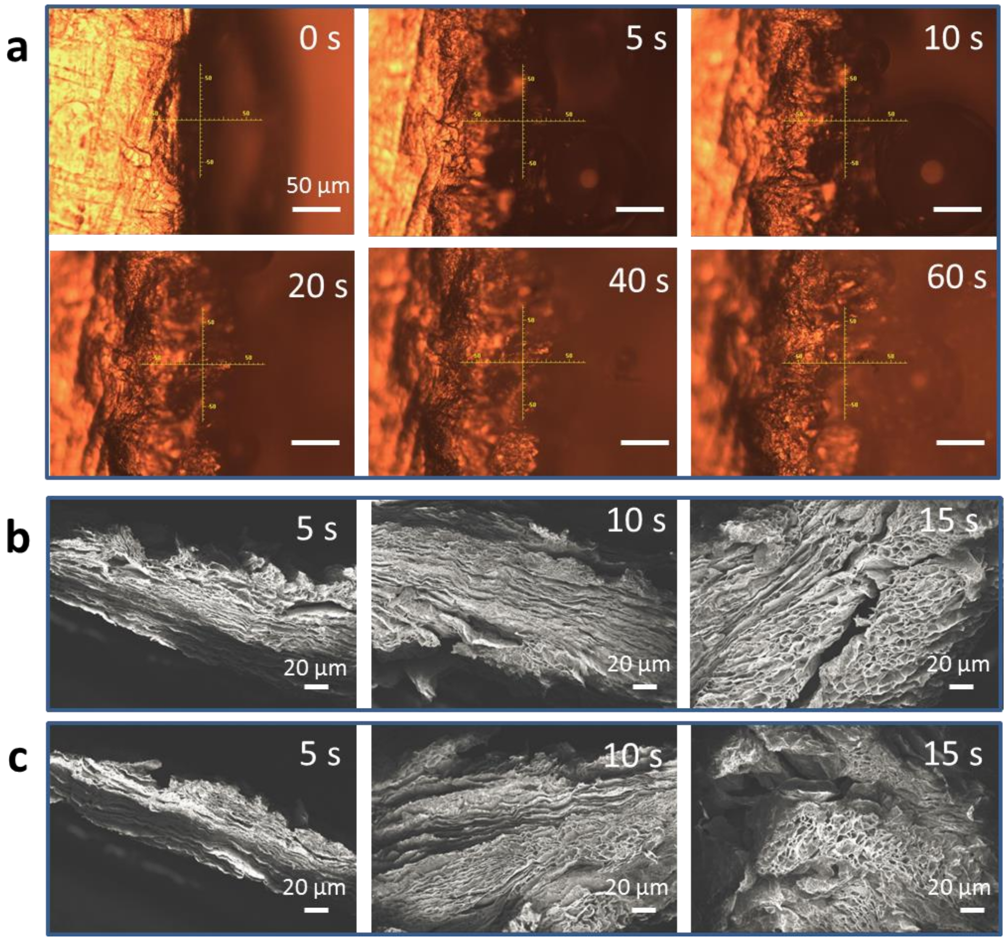

Figure S6 (a) Optical microscopic images captured from the edge of graphite foil, showing structural deformation in the time range of 0-60 s; SEM images of graphite anode (b) and cathode (c) during the exfoliation process.

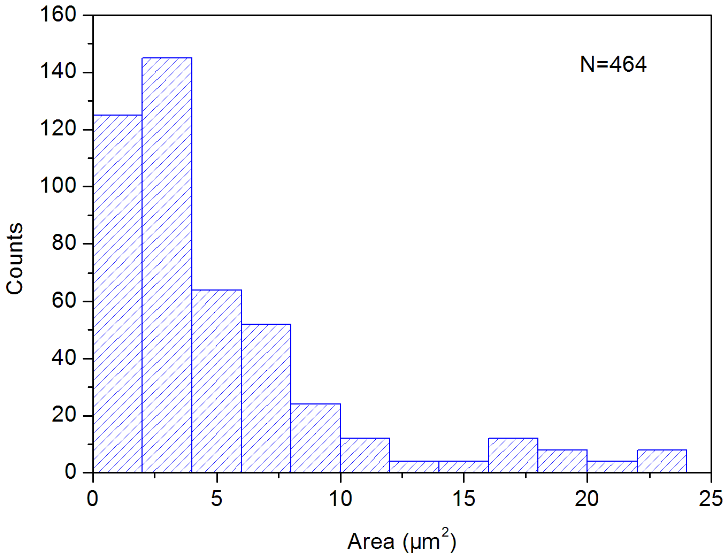

Figure S7 Statistical areal distribution of 464 EG flakes

ImageJ (available from NIH as free software) was performed to obtain the flake area by contrast analysis. Based on statistical calculation of 464 individual EG sheets, over 70 % of EG flakes exhibit areal sizes range from 1 to 5 μm^2. The average area was counted as 5.1 μm^2.

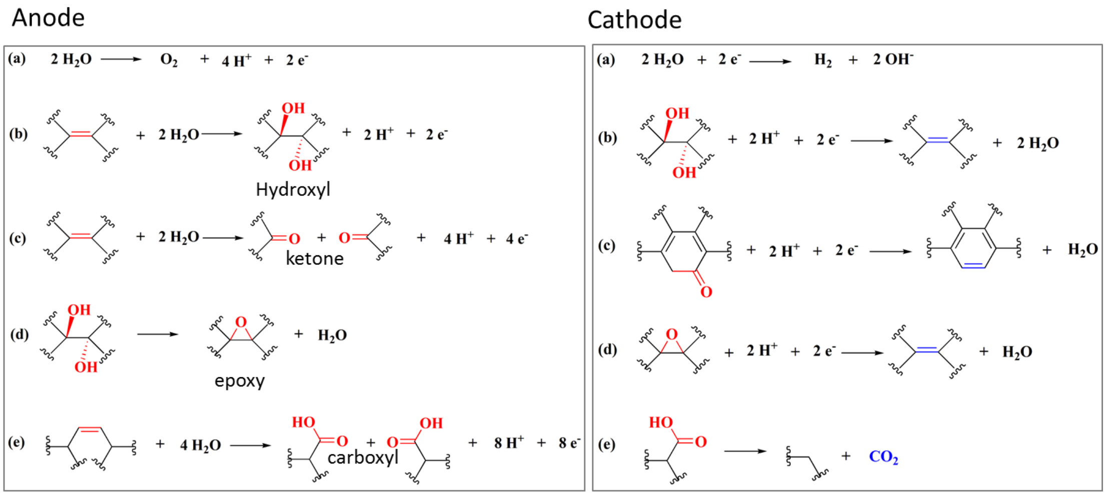

Figure S8 Proposed electrochemical reactions at graphite anode and cathode. At anode, the oxide groups are caused by the attack of oxygen-containing radicals. When anode is switched to cathode, the conjugated aromatic system will be partially restored.

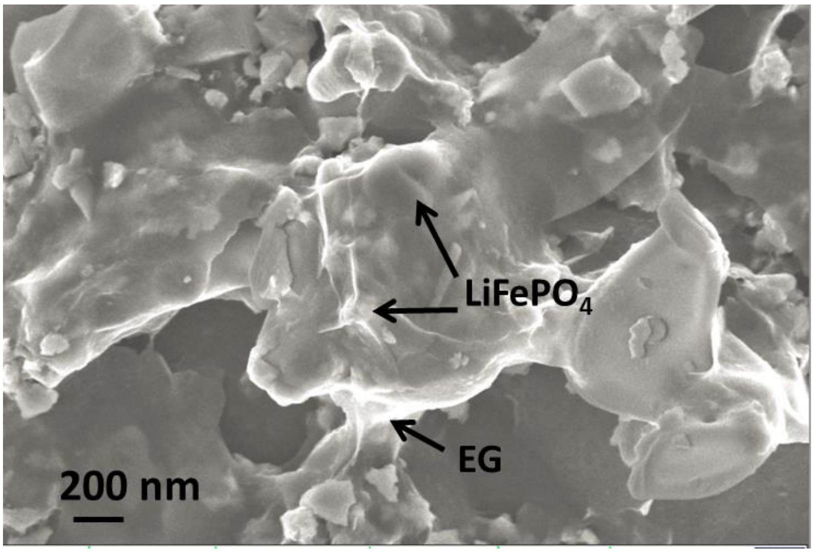

Figure S9 SEM images of EG-wrapped $LiFePO_4$. Graphene layers are uniformly coated on the surface of $LiFePO_4$ particles.

Table S1 EA and XPS data of pristine graphite foil and exfoliated graphene (EG)

Sample	Element	EA	XPS
Graphite	C (at %)	99.57	98.21
	H (at %)	--	N/A
	O (at %)	0.16	1.79
	C/O	622	54.9
EG	C (at %)	95.01	95.50
	H (at %)	0.27	N/A
	O (at %)	4.61	4.50
	C/O	20.6	21.2

N/A: Not applicable

Table S2 FET measurements based on EG flakes with various thickness

EG Flake	Thickness (nm)	Number of layers	Hole mobility ($cm^2 V^{-1} s^{-1}$)
1	1.36	2	274
2	1.42	2	256
3	2.03	3	258
4	0.74	1	430
5	0.80	1	442

Table S3 A brief comparison between our method with other wet-chemical approaches.

Graphene types	**Synthetic methods**	**C/O ratio**	**Id/Ig in Raman**	**Hole mobility ($cm^2\ V^{-1}\ s^{-1}$)**	**Ref.**
Reduced graphene oxide (rGO)	Electrochemical reduction (-6 V, 1 min)	9.26	1.2	N/A	[1]
rGO	Chemical reduction by $Na\text{-}NH_3$, 30 min	16.6	>1	123 (single sheet)	[2]
rGO	Chemical reduction by HI-AcOH, 40 °C, 40 h	11.5	>1	N/A	[3]
rGO	Chemical reduction by Hydrazine vapour, 80 °C, 24 h	N/A	1.75	43.6 (single sheet)	[4]
Electrochemically exfoliated graphene (EEG)	0.5 M Na_2SO_4; 0.5 M H_2SO_4; 0.5 M $LiClO_4$ in water +2 V, 2 min; +10 V till the end	8.8; 8.1; 4.0	0.95; 1.34; 1.00	N/A N/A N/A	[5]
EEG	0.23 M Glycine/H_2SO_4 in water; +3 V, 5 min	8.8	0.7	N/A	[6]
EEG	Mixture of LiCl, Et_3NHCl in DMSO, CV scan from 0 V to -6 V	15.7	0.3	N/A	[7]
EEG	0.1 M H_2SO_4 in water, +10 V, 15 min	12.3	0.4	233 (bilayer flake)	[8]
EEG	0.1 M $(NH_4)_2SO_4$ in water +10 V, 15 min	17.2	0.25	310 (single-layer flake)	[9]
EEG	0.1 M TBA.HSO_4 in water (neutralized by NaOH), ±10 V, 0.1 Hz (alternating current), 15 min	21.2	0.16	430 (single-layer flake)	This work

N/A: not available; AcOH: acetic acid; Et_3NHCl*: triethylamine hydrochloride; DMSO: dimethyl sulfoxide; CV: cyclic voltammetry*

Reference

[1] X. Wang, I. Kholmanov, H. Chou, R. S. Ruoff, *ACS Nano* **2015**, *9*, 8737-8743.

[2] H. Feng, R. Cheng, X. Zhao, X. Duan, J. Li, *Nat. Commun.* **2013**, *4*, 1539.

[3] I. K. Moon, J. Lee, R. S. Ruoff, H. Lee, *Nat. Commun.* **2010**, *1*, 73.

[4] J. Yang, J.-W. Kim, H. S. Shin, *Adv. Mater.* **2012**, *24*, 2299-2303.

[5] A. Ambrosi, M. Pumera, *Chem. Eur. J.* **2016**, *22*, 153-159.

[6] K. S. Rao, J. Sentilnathan, H.-W. Cho, J.-J. Wu, M. Yoshimura, *Adv. Funct. Mater.* **2015**, *25*, 298-305.

[7] A. M. Abdelkader, I. A. Kinloch, R. A. W. Dryfe, *ACS Appl. Mater. Interfaces* **2014**, *6*, 1632-1639.

[8] K. Parvez, R. Li, S. R. Puniredd, Y. Hernandez, F. Hinkel, S. Wang, X. Feng, K. Müllen, *ACS Nano* **2013**, *7*, 3598-3606.

[9] K. Parvez, Z.-S. Wu, R. Li, X. Liu, R. Graf, X. Feng, K. Müllen, *J. Am. Chem. Soc.* **2014**, *136*, 6083-6091.

Chapter 4

Cathodic Delamination of Bulk Black Phosphorus into Defect-Free, High-Mobility, Few-Layered Flakes

Learning from graphite exfoliation, many other two-dimensional (2D) materials, such as boron nitride (BN), transition metal dichalcogenides (TMDs) and black phosphorus (BP), have been exfoliated from their bulk layered counterparts whose layers are assembled together by weak van der Waals forces. The 2D flakes, which usually come with unique physical and chemical properties, have triggered tremendous interests in a broad palette of research fields. However, in contrast to intensive research in graphene, the studies on those 2D flakes are still in their infancy. One of the bottlenecks is the low yield of production. For instance, mechanical exfoliation is able to produce the pristine 2D flakes but only for fundamental research. Other alternatives, like prolonged sonication-assisted exfoliation in solvents, always break the large flakes into small fragments and the production yield is still limited. As presented in previous chapters, electrochemical exfoliation shows remarkable efficiency for large-scale production of graphene materials. It is therefore important to explore its versatility to other conductive layered materials since they follow similar charge transfer and intercalation principles.

In this chapter, we present the first scalable method to produce truly defect-free BP flakes on a macroscopic scale. BP is an interesting material that has a wide range of intrinsic bandgap (0.3-2.0 eV), not covered by any other 2D materials; it exhibit high mobility and high current on/off ratios that are desirable for digital and high frequency electronics. In the past, pristine BP flakes can only be prepared through time-consuming and low-yield scotch-tape cleavage method. How to improve the exfoliation yield becomes a critical concern. Thanks to the intercalation of tetra-*n*-butyl-ammonium (TBA) cations as well as the gas production in our designed electrolyte, the exfoliation yield achieves as high as 78 %, which is much higher than sole cation intercalation (~55 %), according to our experiments. Therefore, this method holds great promise in developing novel BP-based (opto)electronics for which high quality and good processability of BP are required.

4.1 Introduction

Black phosphorus, the most stable allotrope of phosphorus, has recently emerged as a strong competitor to other 2D materials, largely due to its unprecedented electronic band structure, which features a direct bandgap for all thickness.[1] Depending on the number of layers, the bandgap monotonically increases from 0.3 eV in bulk to 2.0 eV for the monolayer,[2] which constitutes a significant advantage with respect to zero-gap graphene and semiconducting TMDs that present relatively large band gaps (1.5-2.5 eV) exclusively in single layers.[3] In addition, BP displays inherent in-plane anisotropy,[4] large charge-carrier mobility[5] and excellent optical/phonon properties,[2b] which sequentially motivate the surge of research on novel electronics and optoelectronics, including logic transistors[6] and broadband photodetectors.[2b, 7]

Inspired by graphite intercalated compounds, inserting guest molecules or ions into layered bulk BP represents a straightforward route to overcome the weak interlayer interaction. However, conventional wet-chemical intercalation processes, which usually involve strong oxidizing agents (e.g. sulfuric acid) to open boundaries by partial oxidation and covalent modification,[8] are destructive to BP flakes as they are chemically unstable.[9] In fact, without gallery expansion, spontaneous intercalation is difficult to occur although BP has relatively large interlayer spacing (d=0.53 nm). To facilitate ion diffusion and then achieve efficient intercalation, it is essential to introduce external driving forces. In this scenario, electrochemical methods, which take advantage of an electric current in conductive medium, are therefore appealing to push charged species into layered compounds in a controllable manner.[10]

In this chapter, we demonstrate a non-oxidative strategy for the delamination of bulk BP using an electrochemical approach. Based on the design of electrolytes, the interlayer spacing of BP crystal has been expanded by incorporating ionic species with various diameters, leading to efficient intercalation/exfoliation process under oxygen-free condition. Once the interlayer distance exceeds 0.80 nm, weak van der Waals interaction becomes negligible.[11] Particularly, the intercalation of tetra-*n*-butyl-ammonium cations, followed by the penetration and reduction of solvated protons, results in high exfoliation yield up to 78 %. The exfoliated flakes exhibit high structural integrity with lateral dimension up to 20.6 μm and mean thickness of 3.7 nm. Bottom-gate and bottom-contact field effect transistors based on few-layer BP flakes demonstrate an average mobility of 195±15 $cm^2 V^{-1} s^{-1}$ and a current on/off ratio of $(1.7\pm0.03)\times10^4$ at 300 K in vacuum, which are further increased to 252±18 $cm^2 V^{-1} s^{-1}$ and $(1.2\pm0.15)\times10^5$ at 143 K, respectively. The excellent electronic properties of the BP flakes obtained by this approach are well comparable to those of mechanically cleaved BP sheets.

4.2 Cathodic delamination of BP in non-aqueous electrolyte

Bulk BP has similar crystal structure to graphite in which the atoms are covalently bonded to form layers, and the layers are connected through weak van der Waals interaction, thus allowing the crystal to cleave along the layer surface by adhesive force or ultrasound-promoted shear force (**Fig. 4.1a**). However, due to the valence shell configuration of phosphorus ($3s^2 3p^3$), bulk BP is composed of puckered orthorhombic layers by sp^3 hybridization (**Fig. 4.1b**). The atomic arrangement displays two inequivalent directions (e.g. zigzag and armchair) within BP lattice (**Fig. 4.1c**). In addition, the lone electron pair on each phosphorus atom makes BP very reactive. The mechanically exfoliated BP flakes undergo fast degradation process on the exposure to ambient conditions through the photo-assisted oxidation reaction with surface-adsorbed water.[12,13] Scanning electron microscope (SEM) images, obtained by Dr. [redacted] with Zeiss Gemini 500, reveal the structure of BP crystal that contains periodic layers with large dimensional sizes (**Fig. 4.1d, 4.1e**).

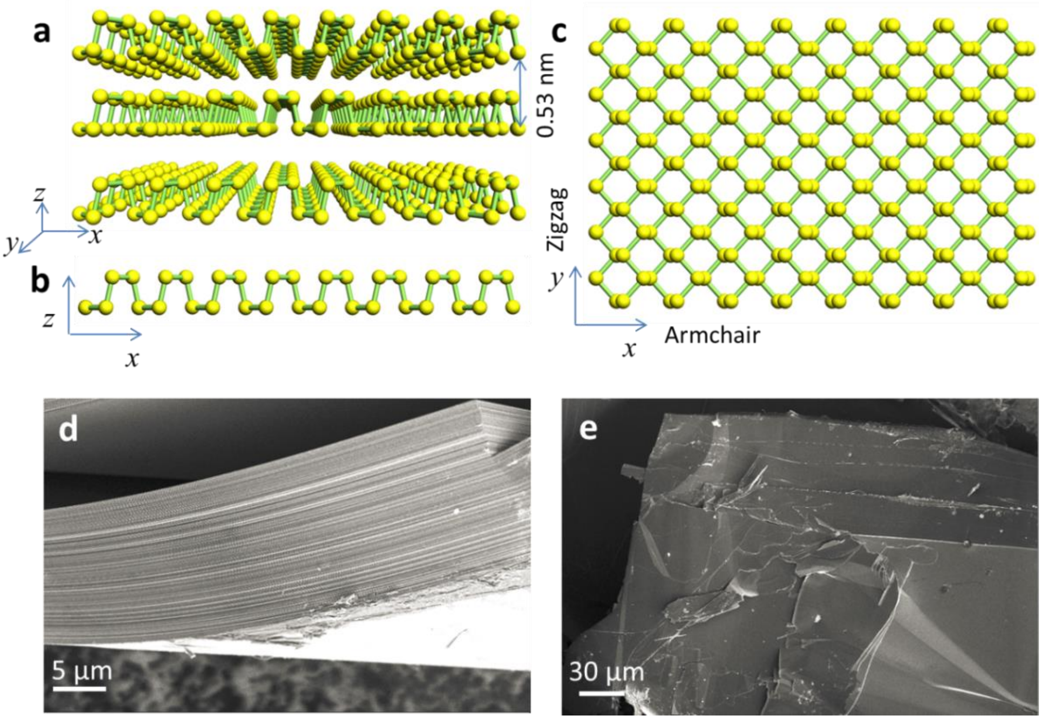

Figure 4.1 Crystal structure of (a) bulk BP and (b, c) an individual monolayer BP flake. (d) Cross-sectional and (e) top-down views of a bulk BP crystal under scanning electron microscope.

Black phosphorus (BP) crystals were purchased from Smart Elements (99.998 % purity) with a room-temperature resistivity of 1.5±0.2 Ω cm. The delamination process was performed using a two-electrode system (**Fig. 4.2a**), in which BP crystal was used as cathode and a piece of platinum foil as anode, respectively. For small batch production, BP crystals with dimension around 5 mm×5 mm×3 mm and weight around 50 mg were used. The electrodes were set in parallel with a constant distance of 2.0 cm. To avoid BP crystal falling off during intercalation process, it was wrapped in a confined space with porous supporting materials (such as Pt gauze or carbon cloth). The whole process shall be kept under the protection of inert gas, either in glove box or under ambient condition but with continuous nitrogen flow into the electrolyte. The electrolyte was made by dissolving inorganic/organic salts into anhydrous, deoxygenated propylene carbonate (PC). The electric current was necessary to drive ionic species into the BP cathode, expand its interlayer distance and ultimately break it down to thin flakes. In order to seek for a suitable intercalating agent, various cations, including Li^+, Na^+ and tetra-alkyl-ammonium (alkyl = methyl, ethyl or *n*-butyl) cations (referred to hereafter as TMA^+, TEA^+ or TBA^+, respectively) were investigated in this system (**Fig. 4.2b**).

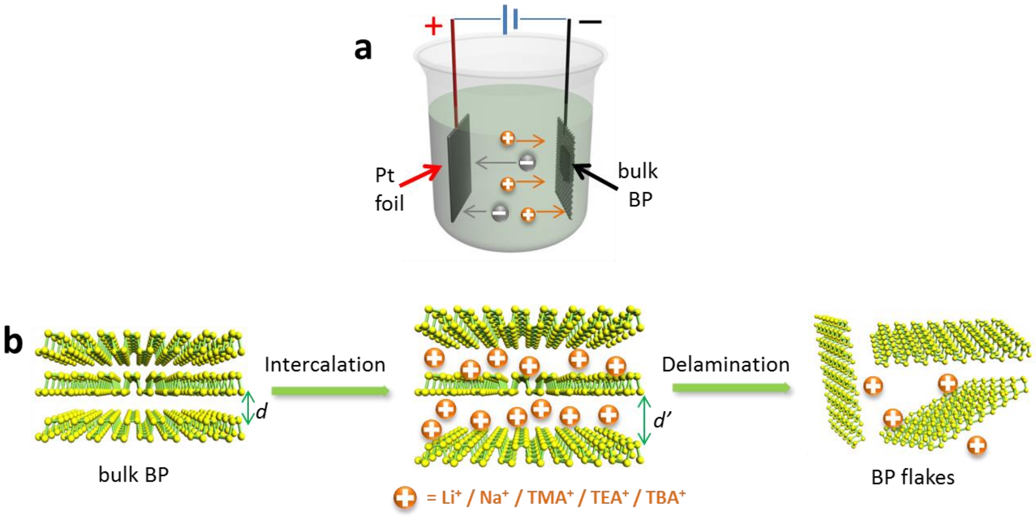

Figure 4.2 (a) Schematic illustration of the reaction cell. (b) Electrochemical delamination procedure of bulk BP crystal in non-aqueous electrolytes.

Alkali ions with small radius (e.g. Li^+ 0.09 nm, Na^+ 0.12 nm) were supposed to migrate inside BP freely, however, they were reduced to alkali metals at low (negative) potential (e.g. -8.0 V). When a moderate potential (e.g. -3.0 V) was applied, slight expansion at BP cathode was observed after 24 h. This result is consistent with previous theoretical studies that the structure of host BP crystal transforms from orthorhombic (BP, space group *Cmca*) to hexagonal (Li_3P or Na_3P, space group $P6_3/mmc$) with an increasing extent of lithiation or sodiation (**Table 4.1**), and the volume variation of BP crystal is relatively small under such condition.[14]

Table 4.1 Description of intermediate Li_xP and Na_xP phases ($0 \leq x \leq 3$)[14]

Stoichiometry	x in Li_xP	Space group	Stoichiometry	x in Na_xP	Space group
BP	0	*Cmca*	Na_3P_{11}	0.273	*Pbcn*
LiP_7	0.143	$I4_1/acd$	Na_3P_7	0.429	$P2_12_12_1$
Li_3P_7	0.429	$P2_12_12_1$	NaP	1	$P2_1/c$
LiP	1	$P2_1/c$	Na_5P_4	1.25	*C2/m*
Li_3P	3	$P6_3/mmc$	Na_3P	3	$P6_3/mmc$

Different from alkali ions, quaternary ammonium cations generally exhibit large diameters (e.g. TMA^+ 0.56 nm, TEA^+ 0.67 nm, and TBA^+ 0.83 nm),[10b] even greater than the interplanar spacing of BP (d = 0.53 nm). Notably, when applying a voltage of -8.0 V, dramatic volume expansion, together with mild bubbling, were observed within 15 min in the solution of tetra-*n*-butyl-ammonium bisulfate ($TBA{\cdot}HSO_4$) (**Fig. 4.3**). In contrast, tetra-methyl-ammonium bisulfate ($TMA{\cdot}HSO_4$) and tetra-ethyl-ammonium bisulfate ($TEA{\cdot}HSO_4$) only promoted limited extent of expansion after a relatively long period (e.g. 1 h).

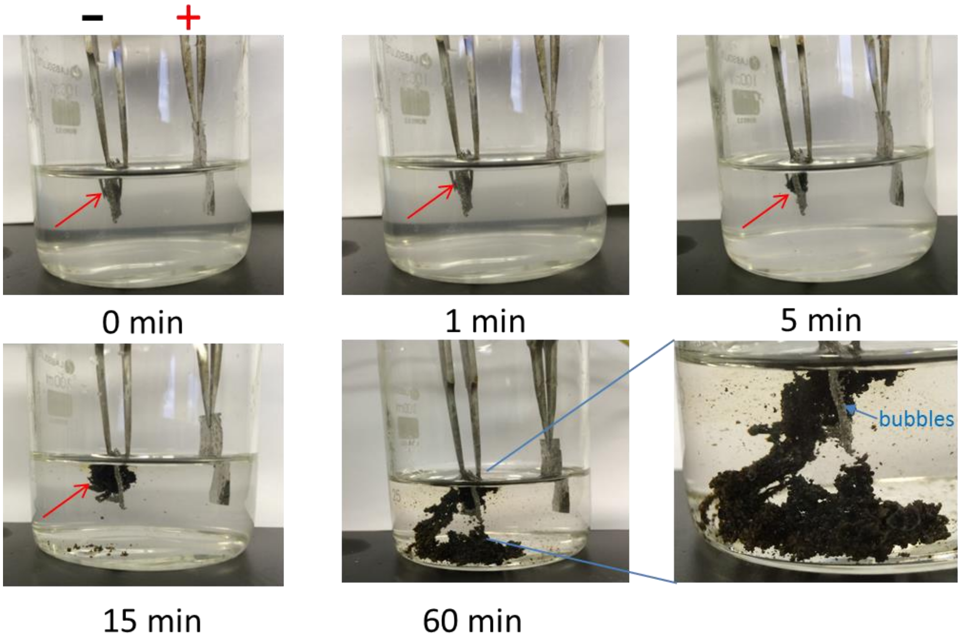

Figure 4.3 (a) Photographs of the cathodic delamination process from 0 to 60 min. The electrolyte is made of $TBA{\cdot}HSO_4$ in propylene carbonate (0.1 M) and the applied bias is -8.0 V.

The delaminated BP flakes were thoroughly washed to remove the residual salts. To achieve stable homogeneous dispersions, the surface tension of solvents should match that of BP (~40 dyne cm^{-1}).[15] The commonly used solvents for BP dispersion typically possess high boiling points, such as NMP (ca. 203 °C), formamide (ca. 210 °C) and dimethyl sulfoxide (ca. 189 °C).[16] However, solvents with low boiling points are favourable for processing BP dispersion into films or composites, especially considering the limited chemical stability of BP. IPA (ca. 83 °C) was found to be a good solvent for hydrophilic BP flakes, although its surface tension does not match.[17]

The delamination yield (η) was obtained from gravimetric calculation using vacuum-assisted filtration. Firstly, the mass of BP crystal was noted as $m1$. After exfoliation and purification, it was dispersed into excessive amount of IPA (e.g. 500 mL) by sonication. Then, the dispersion was filtrated by polytetrafluoroethylene (PTFE) filter membrane (0.2 μm pore size). BP film together with PTFE membrane was dried overnight in vacuum at 80 °C and the weight of BP film (excluding the mass of membrane) was precisely measured as $m2$. The yield is therefore calculated as ($\eta = m1/m2 \times 100$ %). As shown in **Fig. 4.4a**, by raising the diameters of intercalated ions, the yield increased from 5.0 % (Li^+) to 17 % (TEA^+). To our great delight, the intercalation of TBA^+ cations provided an average yield up to 78 %, outperforming the ones from liquid-phase sonication which are less than 38 %.[16] Apparently, the delamination yield also has a strong dependence on working bias as well as electrolyte concentrations, which are respectively related to the speed of cation diffusion and ion density. Through the optimisation of the exfoliation characteristics (**Fig. 4.4b, 4.4c**), a gentle electrolytic condition (-8.0 V, 0.10 M) was chosen in terms of the overall control of complete cation intercalation and the production of large size, high-quality BP flakes.

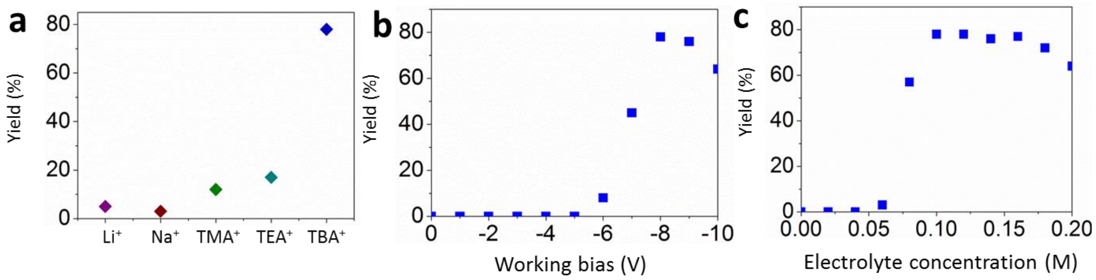

Figure 4.4 (a) The yield variation of BP delamination as a function of intercalating cations. (b, c) The delamination yields obtained in TBA·HSO_4 electrolyte with different working bias and initial concentrations.

BP dispersions with diverse concentrations were studied by UV-vis absorption spectroscopy (**Fig. 4.5a, 4.5b**). The absorption intensity over the cell length (A/l) at λ=468 nm shows a linear relationship with the concentration (C_{BP}), in agreement with Lambert-Beer Law ($A/l=\alpha C_{BP}$, where α is absorbance coefficient), implying good dispersibility of BP flakes in IPA. Such dispersion with defect-free flakes is stable for at least three days without apparent aggregation. After centrifugation with steps from 1000 rpm (212 × *g*) to 5000 rpm (5310 × *g*), the concentration of as-prepared BP dispersion decreased from 0.32 mg mL^{-1} to 0.05 mg mL^{-1} (5000 rpm), which is reflected by the colour change from black to brown (**Fig. 4.5c, 4.5d**).

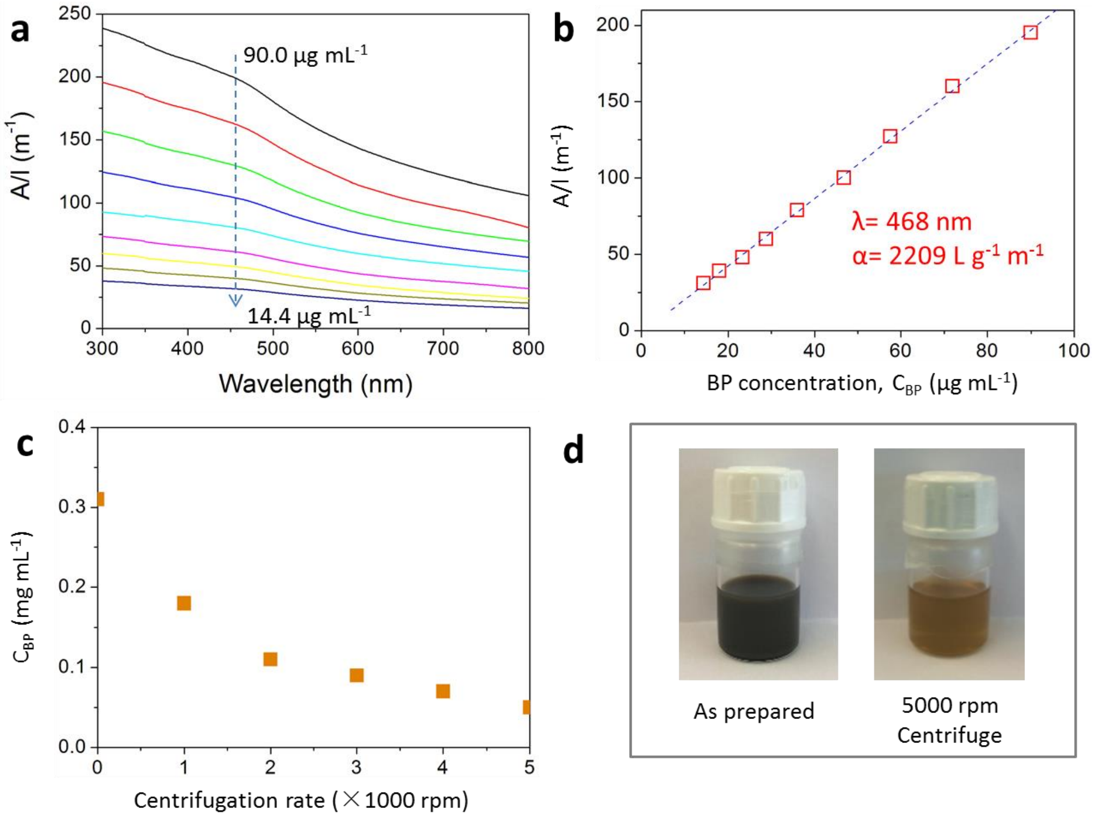

Figure 4.5 (a) UV-vis spectroscopy of BP dispersion in IPA with concentrations varying from 14.4 to 90.0 μg mL^{-1} at the wavelength from 300 nm to 900 nm. (b) Optical absorbance (A, at λ=468 nm) over the cell length (l) at various concentrations of dispersed BP flakes in IPA, affording absorbance coefficient (α) of 2209 L g^{-1} m^{-1}. (c) The influence of the centrifugation rate on the concentration of the BP dispersion in IPA. (d) Optical images of as-prepared BP dispersion (left) and the one after centrifugation (5000 rpm, 10 min) (right).

4.3 The delamination mechanism

As aforementioned, in order to delaminate bulk BP, efficient intercalation of cations is a key step. From our experimental evidence, TBA$^+$ cation, with formula (n-Bu)$_4$N$^+$, is the most effective among the tested tetra-alkyl-ammonium cations, thanks to the flexibility of n-butyl chains.[18] Depending on the conformations, its vertical diameter varies from 0.47 nm (flatten) to 0.89 nm (tetrahedral).[19] The dissociation of organic bisulfate salt results in quantitative TBA^+ cations in the electrolyte:

$TBA\cdot HSO_4 \rightleftharpoons TBA^+ + HSO_4^-$

The diffusion of large, low-charge-density TBA^+ cations within BP is quite difficult unless applying an external current flow. Initially, only flattened TBA^+ cations are able to accommodate inside the interlayer of bulk BP (*d* = 0.53 nm) since they have comparable sizes (**Fig. 4.6**).

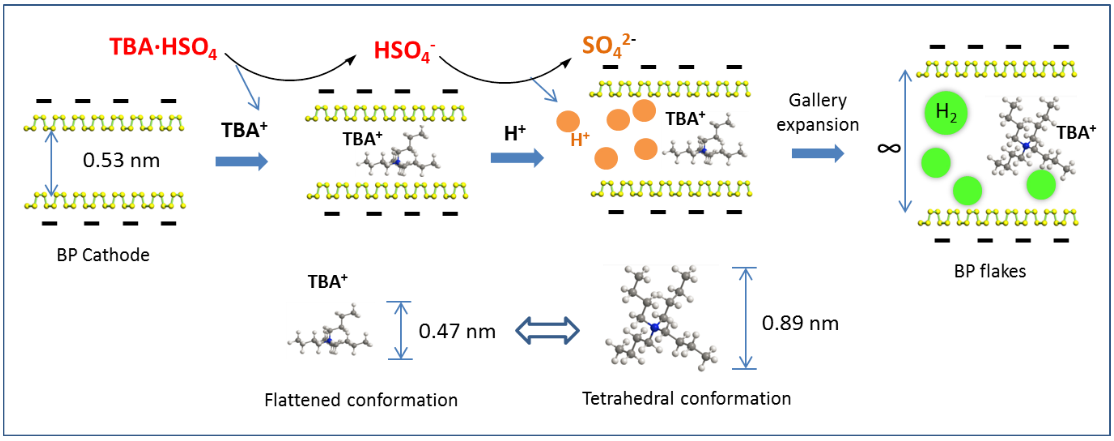

Figure 4.6 Schematic illustration for the intercalation process of TBA^+ cation and proton into the interlayer spacing of BP.

We propose that, following the migration of TBA^+ cations, the insertion and reduction of solvated protons at BP interfaces, give birth to hydrogen bubbles:

$2H^+ + 2e \longrightarrow H_2$

Given that PC is a polar aprotic solvent and quite stable against cathodic reduction,[19] the solvated protons are generated from the dissociation of bisulfate anions:

$HSO_4^- \rightleftharpoons SO_4^{2-} + H^+$

The partial and variable dissociation is responsible for the limited conductivity of the electrolyte, associated with mild expanding rate at the BP cathode. Nevertheless, the formation of bubbles enlarges the gaps between neighbouring BP layers, which offers the space for the intercalation of tetrahedral TBA^+ cations with a maximum gallery expansion of 0.89 nm. Some theoretical results suggest that, for layered BP, an intersheet separation of 0.80 nm is wide enough to overcome the van der Waals interactions.[11, 20]

In the meantime, cathodic reduction converts TBA^+ cations into various species.[21] Although without gas release, the volume expansion further enhances the interlayer distance.

$(n\text{-Bu})_4N^+ + e^- \rightarrow (n\text{-Bu})_4N\cdot$

$(n\text{-Bu})_4N\cdot \rightarrow n\text{-Bu}\cdot + (n\text{-Bu})_3N$

$n\text{-Bu}\cdot + e^- \rightarrow n\text{-Bu}^-$

In order to validate the role of bisulfate anions, we further investigated tetra-*n*-butyl-ammonium perchlorate ($TBA\cdot ClO_4$) and tetra-*n*-butyl-ammonium hexafluorophosphate ($TBA\cdot PF_6$) under the same conditions. Clearly, sole cation intercalation without bubble formation led to a lower exfoliation efficiency (~55 %). In addition, perchlorate anions were destructive to BP flakes, the colour of electrolyte turned to yellow during the delamination process (**Fig. 4.7a**). Notable defects were observed on BP flakes. High-resolution TEM images, captured by Dr. [redacted] with Zeiss Libra, also displayed the disorder in the lattice structure (**Fig. 4.7b, 4.7c**).

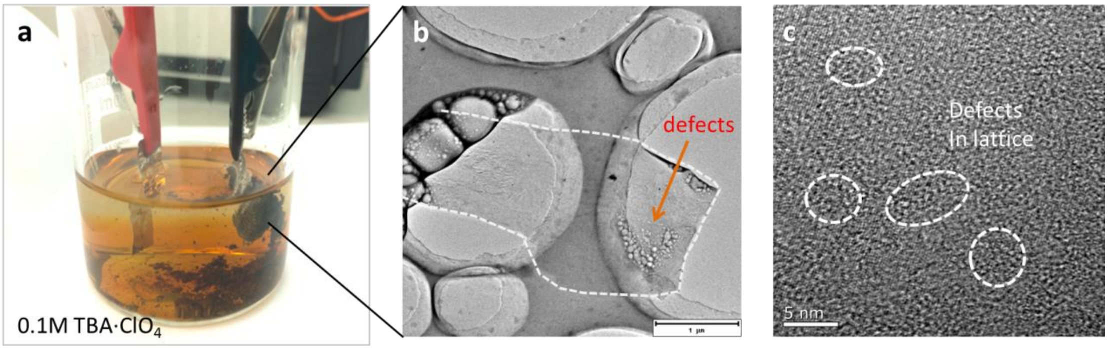

Figure 4.7 (a) Delamination of BP in the electrolyte of $TBA\cdot ClO_4$ in propylene carbonate (0.1 M) at a voltage of -8 V. (b, c) Defects were noticeable in the TEM image of a resulted BP flake.

As to the PC, here it serves not only as medium for ion diffusion, but also ensures that freshly delaminated BP sheets remain dispersed rather than re-aggregated, since it has a moderate surface tension (40.8 dyne cm^{-1}),[22] close to that of BP sheets (~40 dyne cm^{-1}).[15]

Cyclic voltammetry (CV) measurements were performed to understand the exfoliation process. As depicted in **Fig. 4.8**, scanning from 1.0 to -2.0 V and -2.5 V does not show apparent peaks. However, from 1.0 to -3.0 V, a clear cathodic peak current associated with the intercalation of TBA cations appears. On the reverse scan an anodic peak current is observed which is connected to the de-intercalation of TBA cations. Other small anodic peaks are resulted from the oxidation of BP, as it is chemically unstable under oxidative conditions. In the meantime, the BP electrode undertakes irreversible expansion which does not recover after the removal of applied voltages. Therefore, the potential requires for TBA intercalation into bulk BP is between -2.5 V and -3.0 V (vs. SCE). Successive scans from -3.5 V to 1.0 V and from -5.0 V to -1.0 V yield a steady increase in the peak currents, indicating that the solvent/electrolyte is stable at large negative potentials. It is worth noting that when a high potential of -8 V is applied in this system, the shared potential on BP cathode is -3.72 V (*vs.* SCE), based on open circuit potential measurements (**Fig. 4.9**).

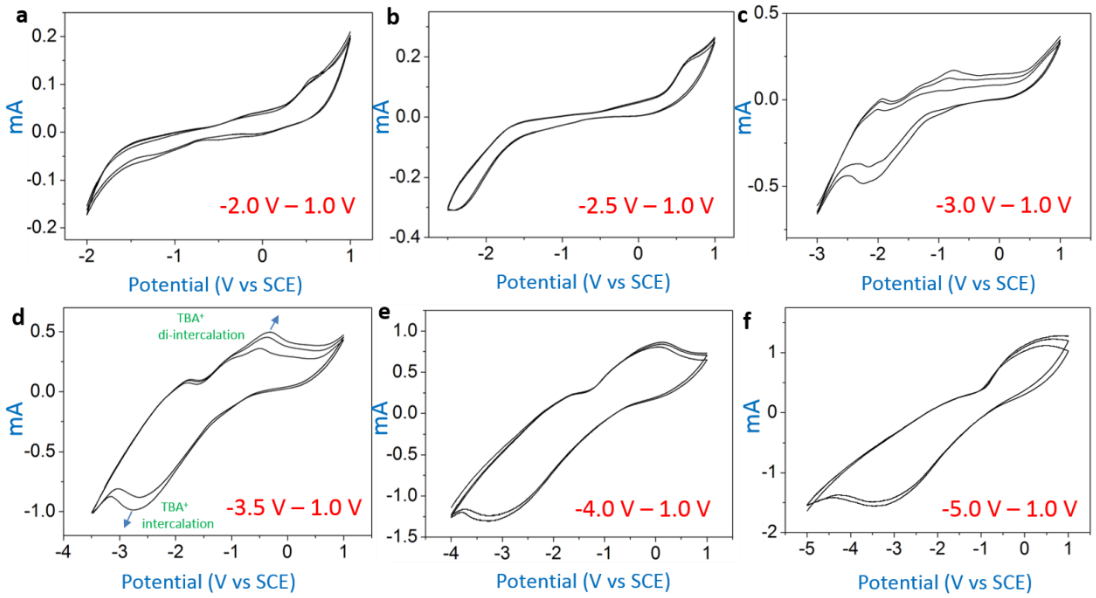

Figure 4.8 CV curves of a three-electrode system including BP working electrode (without Pt gauze), Pt counter electrode and saturated calomel reference electrode in propylene carbonate containing 0.1 M tetra-*n*-butyl-ammonium bisulfate, recorded at a scan rate of 100 mV s^{-1} in various scan ranges.

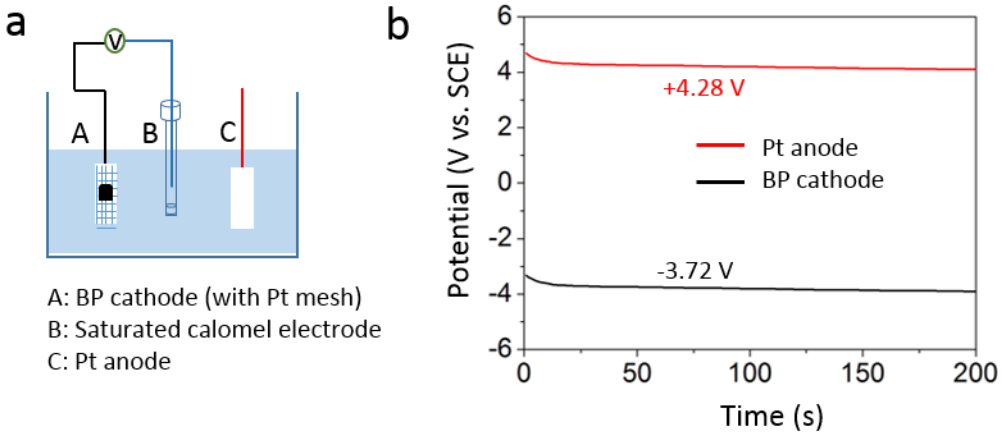

Figure 4.9 (a) Cell Configuration for the measurement of open circuit potential when applying -8 V between A and C, (b) The potentials at cathode and anode (vs. SCE) as a function of running time.

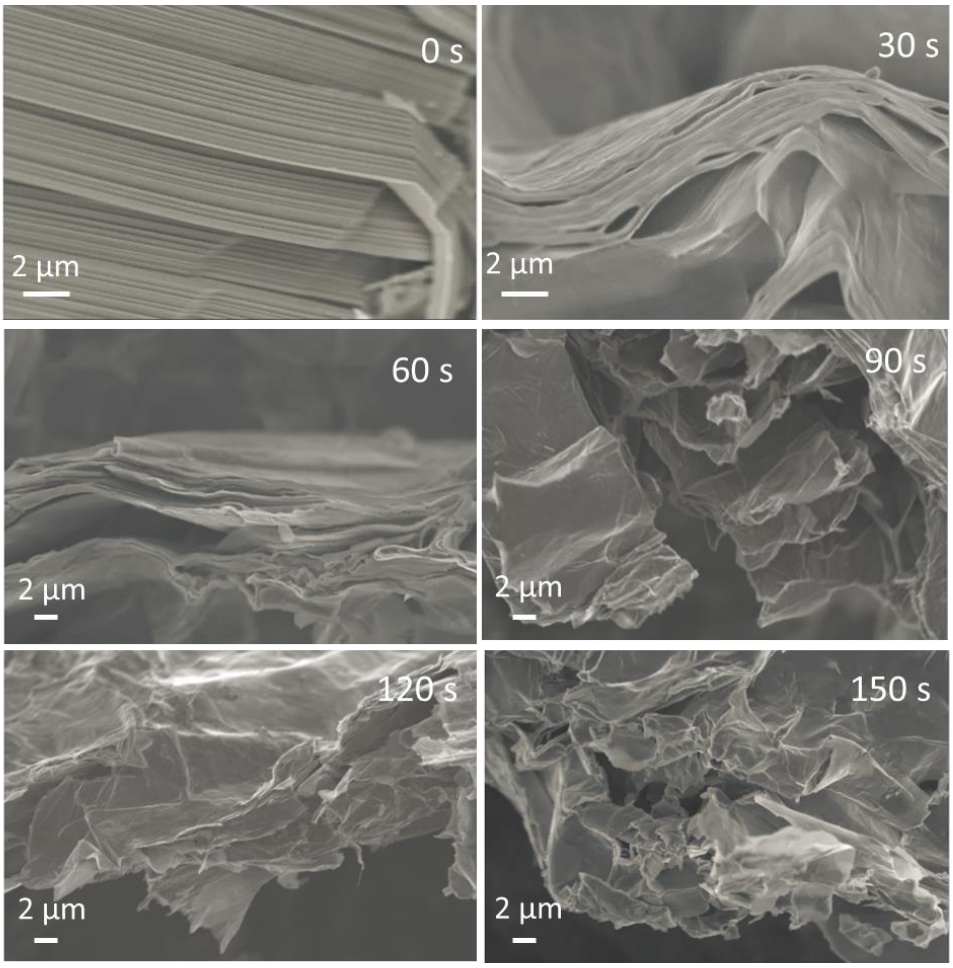

Figure 4.10 SEM images of structural deformation at the BP cathode with various duration of intercalation.

In order to examine the morphological evolution at the BP cathode, SEM images (**Fig. 4.10**) were taken by [redacted] from TU Dresden. In prior to the intercalation, parent BP crystal was closely packed with well-defined layers. Within 30 s, the insertion of TBA^+ cations combined with gas release resulted in a curved and porous structure. The expanded galleries were favourable for further penetration of cations, leading to inhomogeneous expansion at the edges after 60 s. A large extent of segmented expansion was achieved at previously activated boundaries in 90 s. After 150 s, complete cation intercalation boosted structural distortion with dramatic increase of interlayer gaps, splitting bulk BP into individual flakes. The overall intercalation and exfoliation were very efficient under electrochemical circumstance, which agreed with the proposed mechanism.

4.4 Morphological Characterization of BP sheets

BP dispersion in IPA was centrifuged at 3000 rpm prior to basic characterizations. Afterwards, the supernatant was spin-coated onto a Si/SiO_2 wafer (2000 rpm, 30 s) and the samples were annealed at 150 °C for 1 h to remove the solvents. SEM images (**Fig. 4.11a, 4.11b**) reveal a broad size distribution of irregular BP flakes with lateral dimensions generally larger than 2 µm. Some of the flakes even reach a size of 20.6 µm. The statistical analysis of 346 individual flakes (**Fig. 4.11c**) reveals a bimodal size distribution, with modes related to 1.2 μm^2 and 3.9 μm^2. The overall average flake area is estimated as 2.1 μm^2. Since all the tiny pieces (less than 0.2 µm) are also taken into account, the majority of flakes actually exceeds 3.0 μm^2. In contrast, the dimension of liquid-phase exfoliated BP flakes is usually smaller than 1.0 μm^2, as fragmentation is inevitable during the prolonged agitation (e.g. 4 hours). [16, 23]

The crystal structure of BP sheets was elucidated by transmission electron microscopy (TEM). **Fig. 4.11d** and **4.11e** display typical TEM images of thin BP flakes with large lateral sizes. The diffraction pattern shows (002) and (200) facets, which correspond to lattice constants of 0.44 nm and 0.34 nm, respectively. High-resolution TEM image (**Fig. 4.11f**) was obtained by Dr. [redacted] from Fraunhofer Institute for Ceramic Technologies and Systems (IKTS). It demonstrates impressively the orthogonally symmetric structure with intact lattice. The crystal parameters are consistent with the intrinsic features of pristine BP, which implies that cathodic delamination in non-aqueous electrolyte does not cause any defects in the crystal structure of the BP flakes. This is also confirmed by the lattice over a broad region (~700 nm^2) (**Fig. 4.12**).

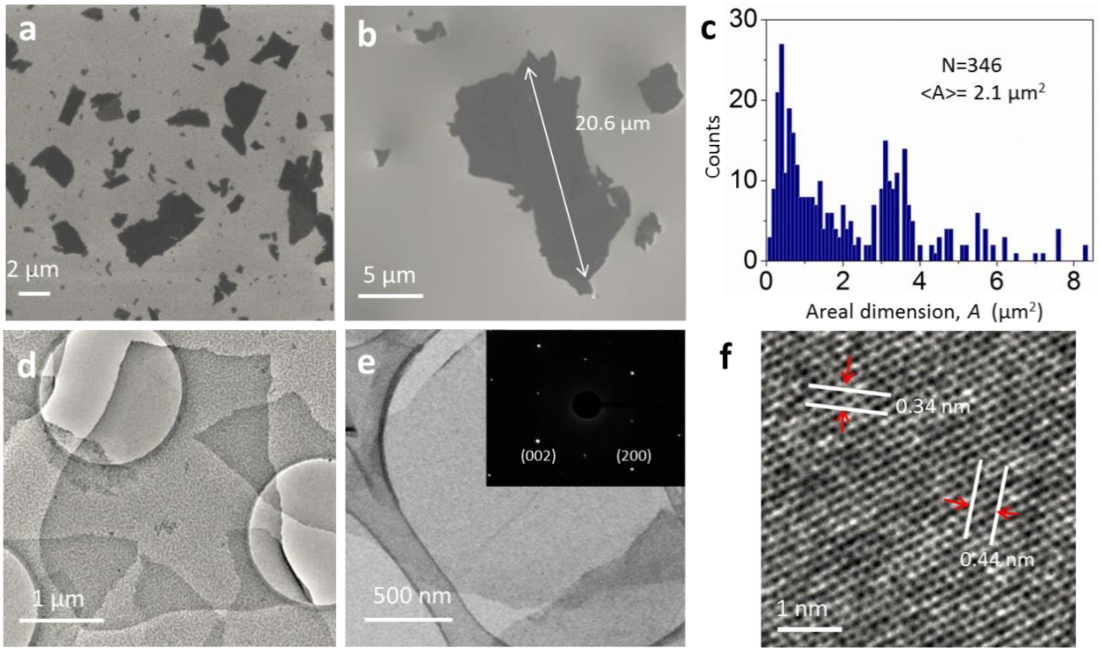

Figure 4.11 (a, b) Representative SEM images of BP flakes from electrochemical delamination. (c) Histogram of dimensional distribution obtained from the analysis of 346 individual sheets with NIH software *ImageJ*. (d, e) Typical low-resolution TEM images by lacey carbon support (inset: the corresponding diffraction pattern). (f) High-resolution TEM image of BP flake.

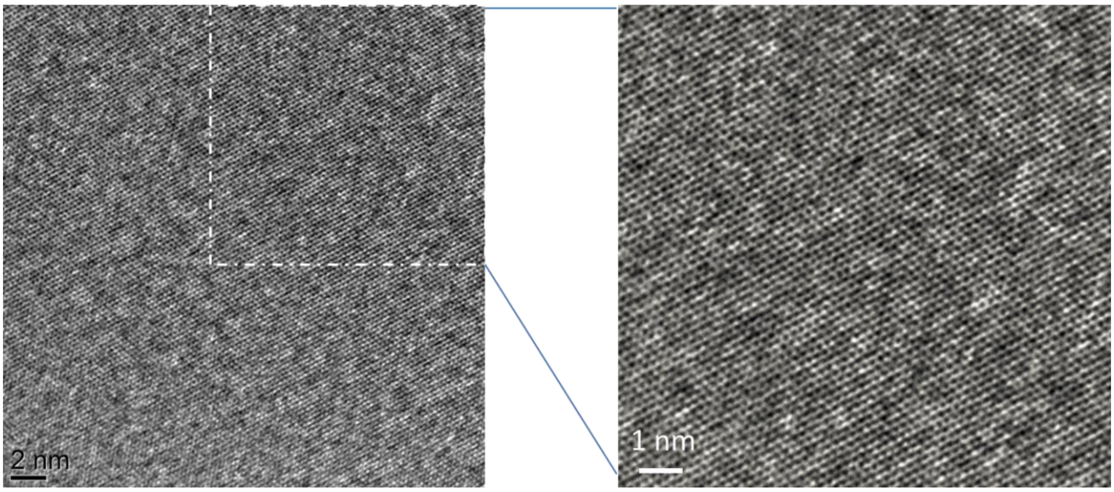

Figure 4.12 High-resolution TEM images of BP sheets at a board region of ca. 720 nm^2, without showing lattice defects.

The thickness of the BP flakes varies from 1.3 nm to 9.5 nm, based on the atomic force microscopy (AFM) analysis with Bruker Multimode 8 (**Fig. 4.13a-4.13c**). The small fragments have lower height profiles (ca. 2.0 nm), while most of the large sheets are between 3.0-6.0 nm thick. Counting from 120 randomly selected flakes, the mean thickness appears at 3.7±1.3 nm (corresponding to 4-10 layers) (**Fig. 4.13d**). Note that, for solution-processed BP flakes, the apparent AFM heights are usually overestimated because of the residual solvents and the possible capillary adhesion.[9]

Moreover, the air stability of solution-processed BP flakes was monitored by AFM under ambient condition. BP dispersion was drop-casted onto Si/SiO_2 substrates and directly sent to the measurements without using additional heating process. As shown in **Fig. 4.14**, the surface of flake does not show any bubbles, as an indication of degradation,[13] until 5-day air exposure. Considering the electrolyte is not volatile and has high boiling point (242 °C), a thin layer of residual solvent, despite with a small amount, behaves as an isolating barrier that prevents BP flakes against surface oxidation. This is thus attractive for the scaled-up processing of BP flakes, compared to other passivation methods using polymer dielectrics,[24] atomic oxide layers,[25] van der Waals heterostructure[26] or covalent functionalization.[27]

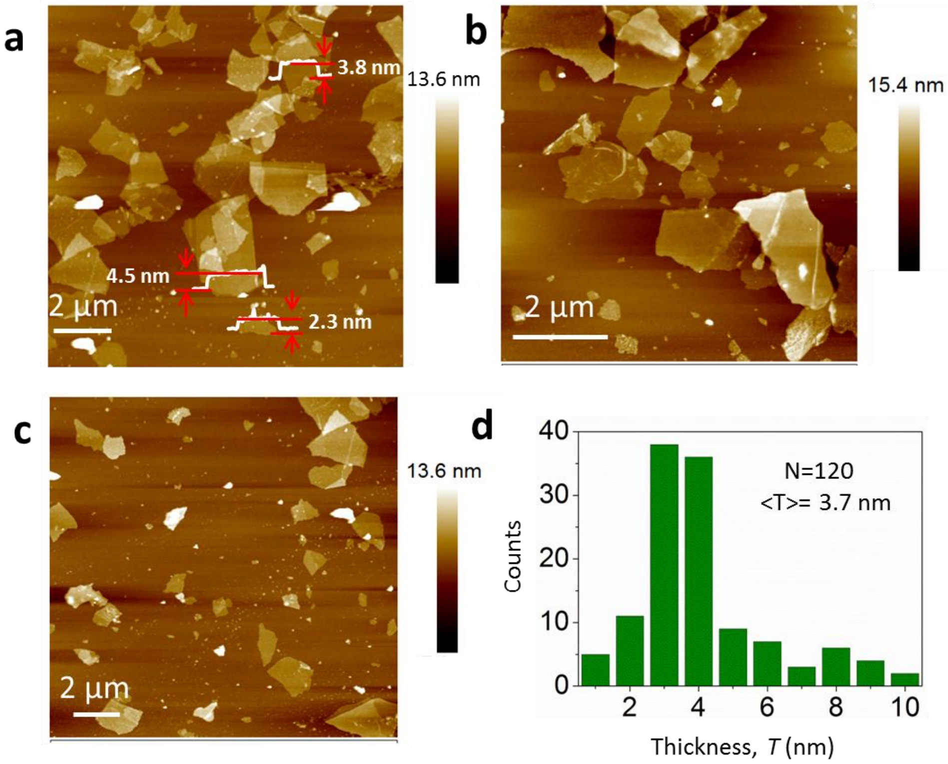

Figure 4.13 (a, b, c) Representative AFM images of BP sheets. (d) Statistical calculation from the height profile of 120 separate sheets.

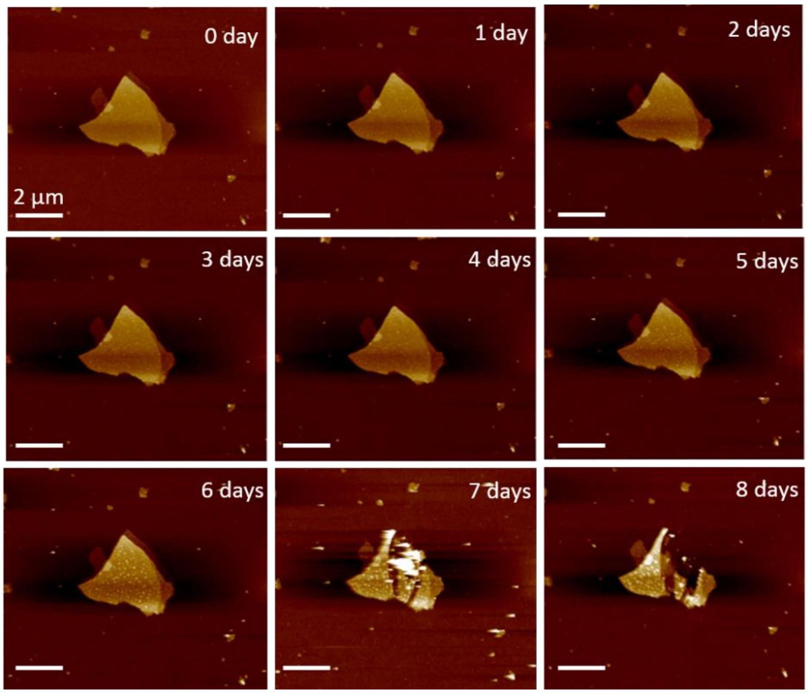

Figure 4.14. AFM images of solution-processed BP flake exposed in air from 0-8 days.

4.5 Structural elucidation

Raman spectra (**Fig. 4.15a**) of BP flakes disclose three characteristic phonon modes located at 362 cm^{-1} (A_g^1), 439 cm^{-1} (B_{2g}) and 466 cm^{-1} (A_g^2). The integrated intensity ratio A_g^1/A_g^2 is sensitive to quality variation caused by degradation. For instance, BP sheets with low oxidation level have A_g^1/A_g^2 values greater than 0.20, while non-oxidized pristine sheets lie in the range 0.40-0.60.[13a] The statistical analysis (**Fig. 4.15b**) reveals that the A_g^1/A_g^2 ratios of BP sheets are 0.33-0.70, quite comparable to bulk BP. Partial oxidation on some flakes may be ascribed to the ambient exposure during Raman measurements.[13b] Because the average thickness of BP flake is around 3.7 nm (7-8 layers), the position of A_g^2 mode does not change when compare the exfoliated flakes with bulk crystal. This observation agrees with many other reports.[13, 15, 16]

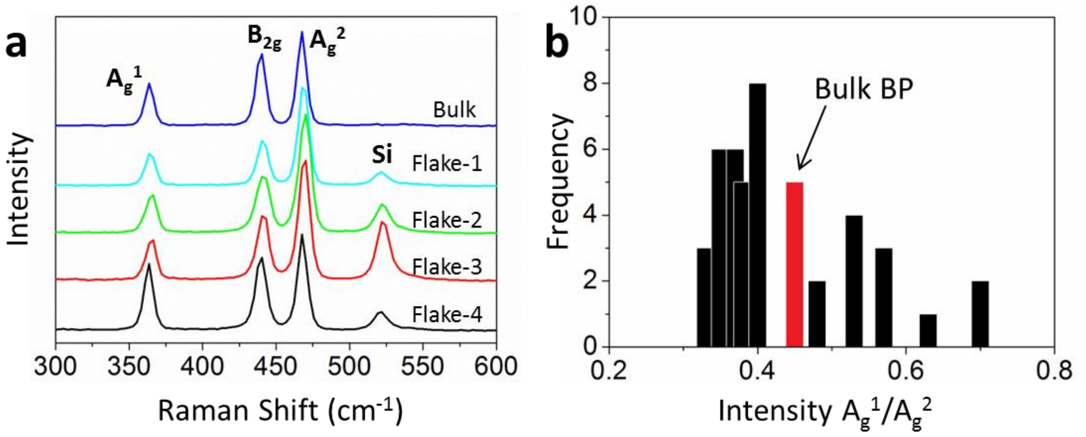

Figure 4.15 (a) Raman spectra of bulk BP and separate flakes, excited by 633 nm laser (sample size = 45). (b) Histogram of A_g^1/A_g^2 intensity ratio from Raman spectra.

To further verify the quality of delaminated flakes, the dispersion was filtrated onto a Teflon membrane (0.2 µm pore size) and dried in a vacuum oven at 100 °C. Afterwards, the free-standing films were peeled off from membrane (**Fig. 4.16a**). The SEM images of the BP film (**Fig. 4.16b-4.16d**) showed that the thin flakes were homogeneously distributed and overlapped with each other. The element mapping was carried out by [redacted] from TU Dresden. It confirmed the high purity of phosphorus (**Fig. 4.16e, 4.16f**). The structural of BP films was further investigated by X-ray diffraction (XRD) and X-ray photoelectron spectroscopy (XPS). XRD spectrum (**Fig. 4.17a**) displays the main characteristic of high crystalline BP (JCPDS NO. 73-1358), as evidenced by strong intensity of (020), (040) and (060) peaks at 17.0°, 34.2° and 52.4°, respectively. The high-resolution spectrum and survey spectrum of XPS were provided by Dr. [redacted] from Shanghai Jiao Tong University. They were presented in **Fig. 4.17b, 4.17c** respectively. The band associated with P2p appears at ca. 130 eV, which can be divided into $P2p_{1/2}$ (130.5 eV) and $P2p_{3/2}$ (129.5 eV), as the key feature of crystalline BP. Moreover, the sub-band related to the oxidized phosphorus (PO_x) (ca. 136 eV) is hard to distinguish, indicating that the structural integrity of BP sheets is well preserved under cathodic exfoliation process.

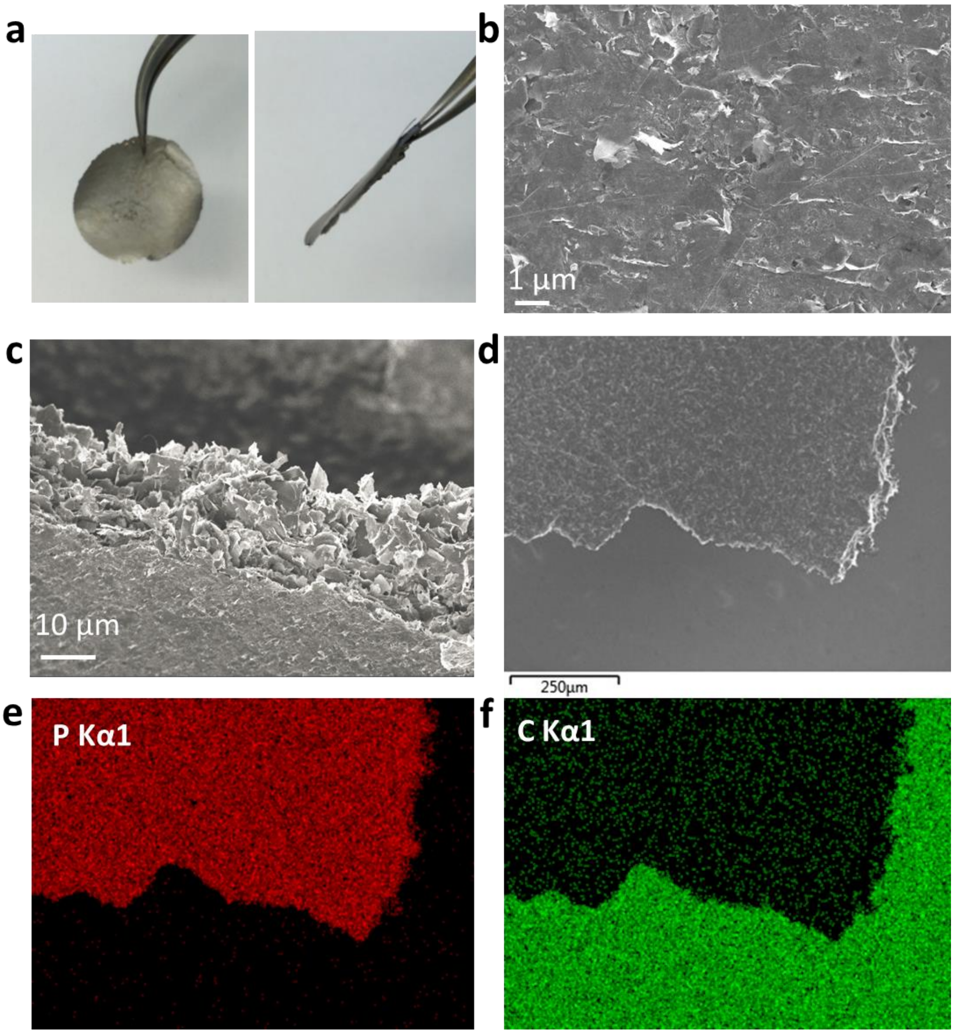

Figure 4.16 (a) Photograph of a free-standing BP film made by filtration. (b) Surface and (c, d) edges of BP film pasted on a conductive carbon tape under SEM. (e, f) Element mappings of BP film show strong intensity of phosphorus and carbon, respectively.

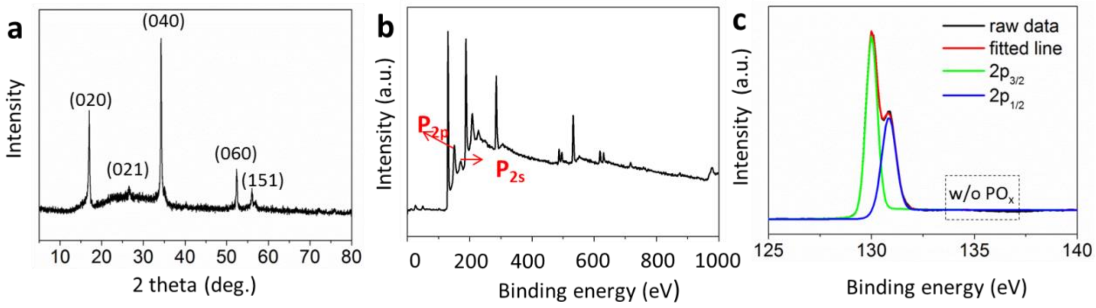

Figure 4.17 (a) Representative XRD spectrum and (b, c) XPS spectra of BP films.

4.6 Electronic properties

To study the electronic properties of our BP flakes, FET devices were fabricated in a nitrogen-filled glove box using heavily n-doped silicon substrates that were covered with a 300 nm-thick thermally grown oxide dielectric. This part of work was carried out by [redacted] from MPI-P. Bottom-gate and bottom-contact devices were fabricated by spin-coating (2000 rpm, 60 s) of the BP dispersion. The concentration of BP dispersion in IPA was 0.10 mg mL^{-1}. Afterwards, the samples were annealed at 300 °C for 10 hours inside the glove box to remove any residual solvents. The hole mobility was calculated from the linear regime of the transfer curves following this equation:

$$\mu = \frac{L}{W C_i V_d} \times \frac{\Delta I_d}{\Delta V_g}$$

(where C_i is the dielectric capacitance), L and W are the channel length and width between source/drain electrode, respectively).

All device tests were carried out under vacuum using a HEWLETT PACKARD 4155B semiconductor parameter analyzer.

The schematic structure of a representative BP-based FET device is shown in **Fig. 4.18a**, where a piece of BP flake covers on the top of source and drain electrodes. SEM and AFM images (**Fig. 4.18b, 4.18c**) reveal that a large BP flake bridges the 2.5 μm long transistor channel between the source and drain electrodes. The BP flake is 3.1 μm wide and 8.5 nm thick.

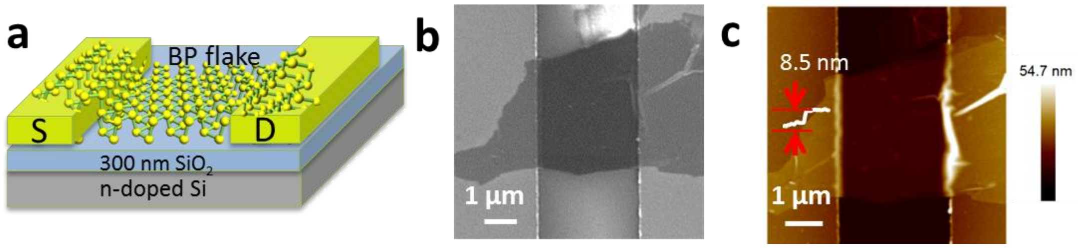

Figure 4.18 (a) Illustration of the field effect transistor based on few-layer BP

(BP-FET), (b, c) SEM and AFM images of BP-FET transistor channel with the BP flake bridging the source and drain electrodes.

The charge transport behaviour of the few-layer BP transistor (BP-FET) was characterized at room temperature under vacuum condition (~1×10^{-5} mbar). The transfer curve (**Fig. 4.19a**) shows a maximum drive current (I_{ds}) of 157 μA μm^{-1} at V_{ds} of 1 V. Based on the linear slope of I_{ds}, the hole mobility is calculated to be 201 cm^2 V^{-1} s^{-1}, which is well comparable with the reported values of mechanically exfoliated BP flakes and superior to liquid-exfoliated sheets under similar testing conditions (**Table 4.2**). For V_{ds} varying from 1 V to 1 mV, the hole mobilities remain constant at around 200 cm^2 V^{-1} s^{-1}, while the turn-on current at positive gate voltages gradually weakens with the decrease of V_{ds}. The hole dominated charge transport characteristics may originate from the doping effect by residual solvent,[28] since it is difficult to remove the solvent molecules underneath the BP flakes via thermal annealing. The I-V characteristics (**Fig. 4.19b**) show excellent linearity in the V_{ds} range from -0.2 to 0.2 V under different V_{gs}, indicating an Ohmic contact in this region. In addition, the temperature dependent transfer curves demonstrate that both hole mobility and drain current modulation (I_{on}/I_{off}) increase with temperature decrease from 300 K to 143 K (**Fig. 4.19c**).

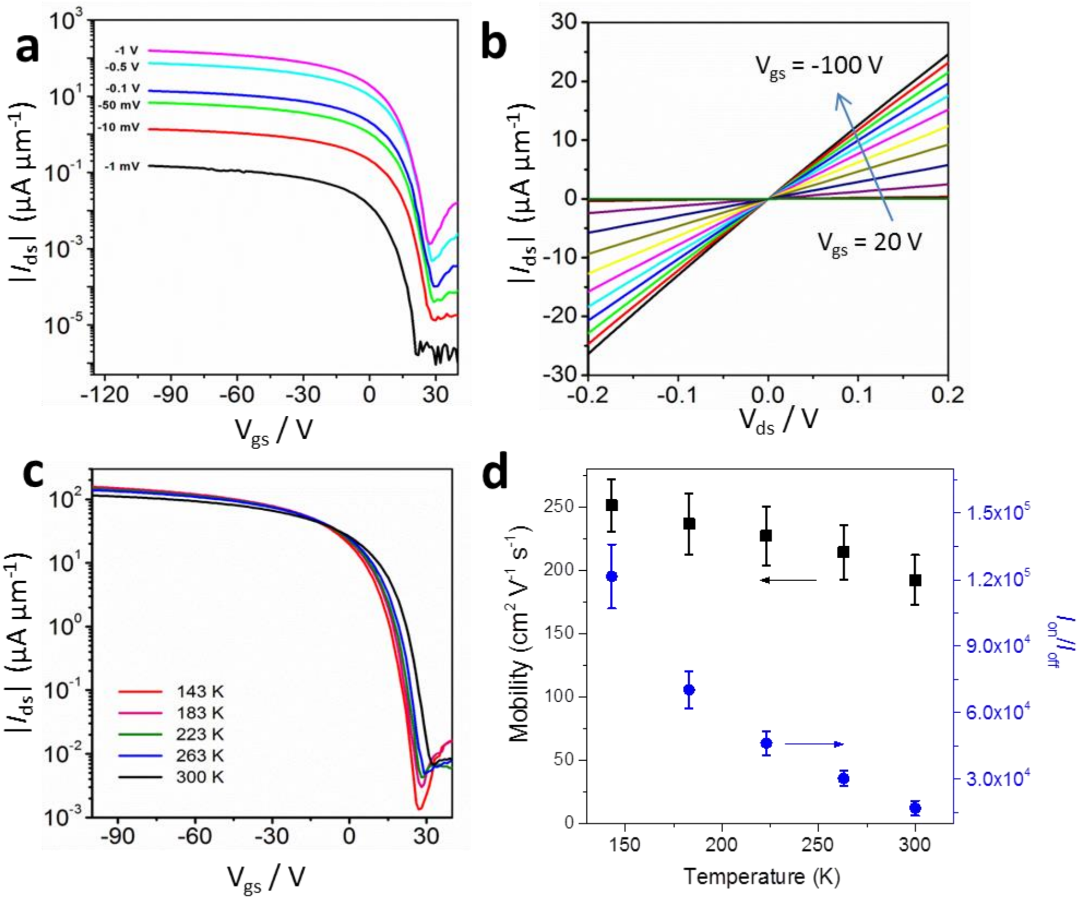

Figure 4.19 (a) Transfer curves of a BP-FET with different source-drain bias (V_{ds}) from -1 mV to -1 V measured under vacuum conditions. (b) The *I*-*V* characteristics for the same BP-FET. (c) Temperature-dependent transfer curves measured from 300 to 143 K. (d) Temperature-dependent hole mobility and I_{on}/I_{off} ratio. Error bars for field-effect mobility and on/off ratio represent the uncertainties arising from anisotropic nature and irregular shape of BP samples.

The I_{on}/I_{off} ratio and hole mobility are 1.2×10^5 and 250 cm^2 V^{-1} s^{-1} at 143 K, respectively, which can be attributed to the decrease of electron-phonon scattering at low temperatures.[29] A series of FET devices (>10 devices) have been measured (**Fig. 4.19d, 4.20**) and they follow similar charge-carrier behaviour with an average I_{on}/I_{off} ratio of $(1.7\pm0.03)\times10^4$ and hole mobility of 195±15 cm^2 V^{-1} s^{-1} at 300 K in vacuum, which are further increased to 252±18 cm^2 V^{-1} s^{-1} and $(1.2\pm0.15)\times10^5$ at 143 K, respectively. The error bars here represent the uncertainties arising from anisotropic nature and irregular shape (size) of BP samples. The electronic performances of our BP-FET devices exhibit the best charge carrier mobility reported so far for solution-processed BP flakes, strongly suggesting the outstanding quality of the delaminated flakes. In comparison, pristine BP flakes obtained from mechanical exfoliation usually show ambipolar field-effect characteristics and deliver hole mobility of 10-1000 cm^2 V^{-1} s^{-1} and current switching ratios of 100-10000, depending on the thickness of BP flakes and architecture of devices.[30-34] On the other hand, BP flakes made by prolonged liquid-phase sonication (e.g. 4 h) come with structural damage,[35] thus leading to limited FET mobility (less than 30 cm^2 V^{-1} s^{-1}).[28, 36]

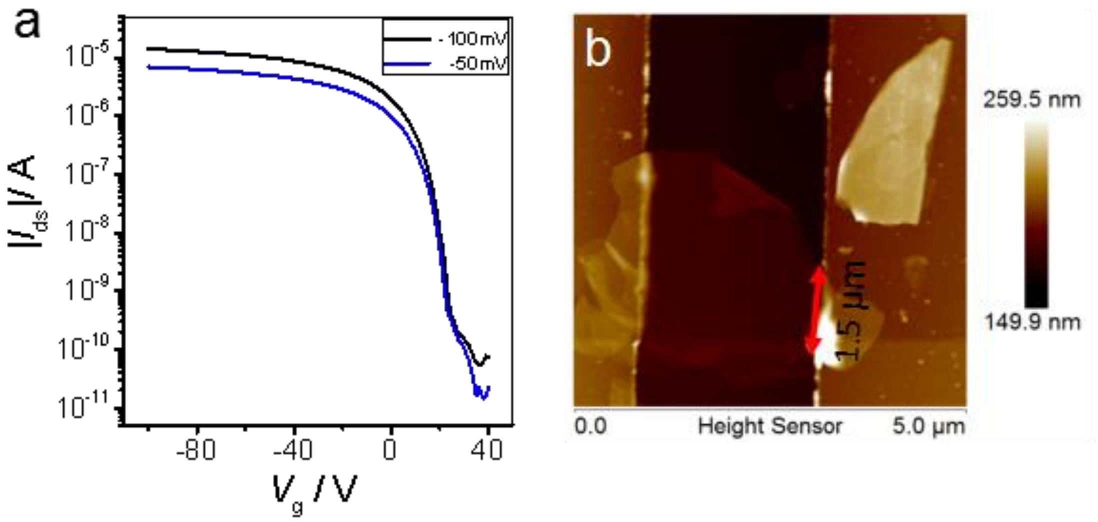

Figure 4.20 (a) Transfer curves of a BP-FET measured at 143 K under vacuum conditions that gives an I_{on}/I_{off} ratio of 1.5×10^5. (b) The AFM image of the corresponding BP flake.

Table 4.2 A summary of FET performance based on few-layer BP flakes

BP flakes	**Synthetic methods**	**Mobility (cm^2 V^{-1} s^{-1})**	I_{on}/I_{off}	**Test temperature (K)**	**Ref**
Few layers (10 nm thick)	Mechanical Exfoliation	242	~5000	300	[30]
Few layers (15 nm thick)		1000-600	~1 × 10^5	120	[31]
Few layers (5 nm thick)		205	~1 × 10^5		
Few layers (8.9 nm thick)		74	~1000	300	[32]
Few layers (5 nm thick)		286	~1 × 10^4	300	[33]
Multiple layers (18.7 nm thick)		170.5	~100	300	[34]
Few layers (7.4 nm thick)	Liquid sonication in DMF	0.58	~1000	300	[28]
Few layers (unknown thickness)	Liquid sonication in NMP	25.9	~1600	300	[36]
Few layers (unknown thickness)	Liquid sonication in water	---	~5000	300	[23]
Few layers (3.7±1.3 nm thick)	Cathodic exfoliation in non-aqueous electrolyte	195±15	$(1.7\pm0.03)\times10^4$	300	This work
		252±18	$(1.7\pm0.03)\times10^4$	143	

4.6 Summary and conclusion

In conclusion, we demonstrate a reliable and efficient method to isolate defect-free BP flakes by using an electrochemical strategy. Especially, the cathodic intercalation process in an oxygen-free environment hinders any defects in the BP flakes. Quaternary ammonium cations are most effective in terms of high exfoliation yield (up to 78 %) and large dimension of exfoliated flakes (up to 20.6 µm). Three key factors are proposed to be responsible for the efficient intercalation and exfoliation: (1) the variable vertical diameter of flexible *n*-butyl chains (0.47-0.89 nm) matches the interlayer distance of BP (0.53 nm); (2) the penetration and reduction of solvated protons ($HSO_4^- \rightleftharpoons SO_4^{2-} + H^+$, $2H^+ + 2e \rightarrow H_2$) further increases the distance between two neighbouring BP layers; (3) the solvent (propylene carbonate) stabilizes the exfoliated flakes against re-aggregation. Field effect transistors based on few-layered BP demonstrated a high I_{on}/I_{off} ratio of $(1.2\pm0.15)\times10^5$ and a hole mobility of 252±18 $cm^2\ V^{-1}\ s^{-1}$ under vacuum condition at 143 K, which are among the best results of solution-processed BP flakes.

The future studies will focus on the selection or preparation of exfoliated BP flakes with well-defined number of layers. This is important for the design of novel electronics, since the band gaps of BP are thickness-dependent. In addition to the devices with simple architecture, the exploration of unconventional device structure and integration of BP flakes with other semiconducting materials will bring new features or enhance the device performances. We believe that this scalable and simple-to-use approach implies exciting opportunities and prospects for the next generation of BP-based technologies.

4.7 References

[1] X. Ling, H. Wang, S. Huang, F. Xia, M. S. Dresselhaus, *Proc. Natl. Acad. Sci. U.S.A.* **2015**, *112*, 4523-4530.

[2] a) A. H. Woomer, T. W. Farnsworth, J. Hu, R. A. Wells, C. L. Donley, S. C. Warren, *ACS Nano* **2015**, *9*, 8869-8884; b) N. Youngblood, C. Chen, S. J. Koester, M. Li, *Nat. Photon.* **2015**, *9*, 247-252.

[3] a) K. Kim, J.-Y. Choi, T. Kim, S.-H. Cho, H.-J. Chung, *Nature* **2011**, *479*, 338-344; b) F. A. Rasmussen, K. S. Thygesen, *J. Phys. Chem. C* **2015**, *119*, 13169-13183.

[4] a) X. Wang, A. M. Jones, K. L. Seyler, V. Tran, Y. Jia, H. Zhao, H. Wang, L. Yang, X. Xu, F. Xia, *Nat Nano* **2015**, *10*, 517-521; b) J. Tao, W. Shen, S. Wu, L. Liu, Z. Feng, C. Wang, C. Hu, P. Yao, H. Zhang, W. Pang, X. Duan, J. Liu, C. Zhou, D. Zhang, *ACS Nano* **2015**, *9*, 11362-11370.

[5] a) L. Li, Y. Yu, G. J. Ye, Q. Ge, X. Ou, H. Wu, D. Feng, X. H. Chen, Y. Zhang, *Nat Nano* **2014**, *9*, 372-377; b) J. Qiao, X. Kong, Z.-X. Hu, F. Yang, W. Ji, *Nat. Commun.* **2014**, *5*, 4475.

[6] a) D. J. Perello, S. H. Chae, S. Song, Y. H. Lee, *Nat. Commun.* **2015**, *6*, 7809; b) D. Xiang, C. Han, J. Wu, S. Zhong, Y. Liu, J. Lin, X.-A. Zhang, W. Ping Hu, B. Özyilmaz, A. H. C. Neto, A. T. S. Wee, W. Chen, *Nat. Commun.* **2015**, *6*, 6485.

[7] H. Yuan, X. Liu, F. Afshinmanesh, W. Li, G. Xu, J. Sun, B. Lian, A. G. Curto, G. Ye, Y. Hikita, Z. Shen, S.-C. Zhang, X. Chen, M. Brongersma, H. Y. Hwang, Y. Cui, *Nat. Nanotechnol.* **2015**, *10*, 707-713.

[8] N. I. Kovtyukhova, Y. Wang, A. Berkdemir, R. Cruz-Silva, M. Terrones, V. H. Crespi, T. E. Mallouk, *Nat. Chem.* **2014**, *6*, 957-963.

[9] D. Hanlon, C. Backes, E. Doherty, C. S. Cucinotta, N. C. Berner, C. Boland, K. Lee, A. Harvey, P. Lynch, Z. Gholamvand, S. Zhang, K. Wang, G. Moynihan, A. Pokle, Q. M. Ramasse, N. McEvoy, W. J. Blau, J. Wang, G. Abellan, F. Hauke, A. Hirsch, S. Sanvito, D. D. O'Regan, G. S. Duesberg, V. Nicolosi, J. N. Coleman, *Nat. Commun.* **2015**, *6*, 8563.

[10] a) Z. Y. Xia, S. Pezzini, E. Treossi, G. Giambastiani, F. Corticelli, V. Morandi, A.

Zanelli, V. Bellani, V. Palermo, *Adv. Funct. Mater.* **2013**, *23*, 4684-4693; b) A. J. Cooper, M. Velický, I. A. Kinloch, R. A. W. Dryfe, *J. Electroanal. Chem.* **2014**, *730*, 34-40; c) Z. Y. Xia, G. Giambastiani, C. Christodoulou, M. V. Nardi, N. Koch, E. Treossi, V. Bellani, S. Pezzini, F. Corticelli, V. Morandi, A. Zanelli, V. Palermo, *ChemPlusChem* **2014**, *79*, 439-446.

[11] V. Sresht, A. A. H. Pádua, D. Blankschtein, *ACS Nano* **2015**, *9*, 8255-8268.

[12] A. Castellanos-Gomez, *J. Phys. Chem. Lett.* **2015**, *6*, 4280-4291.

[13] a) A. Favron, E. Gaufres, F. Fossard, A.-L. Phaneuf-Lheureux, N. Y. W. Tang, P. L. Levesque, A. Loiseau, R. Leonelli, S. Francoeur, R. Martel, *Nat. Mater.* **2015**, *14*, 826-832; b) F. Alsaffar, S. Alodan, A. Alrasheed, A. Alhussain, N. Alrubaiq, A. Abbas, M. R. Amer, *Sci. Rep.* **2017**, *7*, 44540.

[14] a) M. Dahbi, N. Yabuuchi, M. Fukunishi, K. Kubota, K. Chihara, K. Tokiwa, X.-f. Yu, H. Ushiyama, K. Yamashita, J.-Y. Son, Y.-T. Cui, H. Oji, S. Komaba, *Chem. Mater.* **2016**, *28*, 1625-1635; b) M. Mayo, K. J. Griffith, C. J. Pickard, A. J. Morris, *Chem. Mater.* **2016**, *28*, 2011-2021.

[15] G. Hu, T. Albrow-Owen, X. Jin, A. Ali, Y. Hu, R. C. T. Howe, K. Shehzad, Z. Yang, X. Zhu, R. I. Woodward, T.-C. Wu, H. Jussila, J.-B. Wu, P. Peng, P.-H. Tan, Z. Sun, E. J. R. Kelleher, M. Zhang, Y. Xu, T. Hasan, *Nat. Commun.* **2017**, *8*, 278.

[16] Y. Zhang, H. Wang, Z. Luo, H. T. Tan, B. Li, S. Sun, Z. Li, Y. Zong, Z. J. Xu, Y. Yang, K. A. Khor, Q. Yan, *Adv. Energy Mater.* **2016**, *6*, 1600453-n/a.

[17] A. Castellanos-Gomez, L. Vicarelli, E. Prada, J. O. Island, K. Narasimha-Acharya, S. I. Blanter, D. J. Groenendijk, M. Buscema, G. A. Steele, J. Alvarez, *2D Mater.* **2014**, *1*, 025001.

[18] A. J. Cooper, N. R. Wilson, I. A. Kinloch, R. A. W. Dryfe, *Carbon* **2014**, *66*, 340-350.

[19] W. Sirisaksoontorn, A. A. Adenuga, V. T. Remcho, M. M. Lerner, *J. Am. Chem. Soc.* **2011**, *133*, 12436-12438.

[20] L. Shulenburger, A. D. Baczewski, Z. Zhu, J. Guan, D. Tománek, *Nano Lett.* **2015**, *15*, 8170-8175.

[21] C. E. Dahm, D. G. Peters, *J. Electroanal. Chem.* **1996**, *402*, 91-96.

[22] X. You, M. I. Chaudhari, L. R. Pratt, N. Pesika, K. M. Aritakula, S. W. Rick, *J. Chem. Phys.* **2013**, *138*, 114708.

[23] J. Kang, S. A. Wells, J. D. Wood, J.-H. Lee, X. Liu, C. R. Ryder, J. Zhu, J. R. Guest, C. A. Husko, M. C. Hersam, *Proc. Natl. Acad. Sci. U.S.A.* **2016**, *113*, 11688-11693.

[24] M. Engel, M. Steiner, P. Avouris, *Nano Lett.* **2014**, *14*, 6414-6417.

[25] J. Na, Y. T. Lee, J. A. Lim, D. K. Hwang, G.-T. Kim, W. K. Choi, Y.-W. Song, *ACS nano* **2014**, *8*, 11753-11762.

[26] R. A. Doganov, E. C. T. O'Farrell, S. P. Koenig, Y. Yeo, A. Ziletti, A. Carvalho, D. K. Campbell, D. F. Coker, K. Watanabe, T. Taniguchi, A. H. C. Neto, B. Özyilmaz, *Nat. Commun.* **2015**, *6*, 6647.

[27] C. R. Ryder, J. D. Wood, S. A. Wells, Y. Yang, D. Jariwala, T. J. Marks, G. C. Schatz, M. C. Hersam, *Nat. Chem.* **2016**, *8*, 597-602.

[28] P. Yasaei, B. Kumar, T. Foroozan, C. Wang, M. Asadi, D. Tuschel, J. E. Indacochea, R. F. Klie, A. Salehi-Khojin, *Adv. Mater.* **2015**, *27*, 1887-1892.

[29] G. Wang, L. Bao, T. Pei, R. Ma, Y.-Y. Zhang, L. Sun, G. Zhang, H. Yang, J. Li, C. Gu, S. Du, S. T. Pantelides, R. D. Schrimpf, H.-j. Gao, *Nano Lett.* **2016**, *16*, 6870-6878.

[30] L. Chen, G. Zhou, Z. Liu, X. Ma, J. Chen, Z. Zhang, X. Ma, F. Li, H.-M. Cheng, W. Ren, *Adv. Mater.* **2016**, *28*, 510-517.

[31] F. Xia, H. Wang, Y. Jia, *Nat. Commun.* **2014**, *5*, 4458.

[32] J. D. Wood, S. A. Wells, D. Jariwala, K.-S. Chen, E. Cho, V. K. Sangwan, X. Liu, L. J. Lauhon, T. J. Marks, M. C. Hersam, *Nano Lett.* **2014**, *14*, 6964-6970.

[33] H. Liu, A. T. Neal, Z. Zhu, Z. Luo, X. Xu, D. Tománek, P. D. Ye, *ACS Nano* **2014**, *8*, 4033-4041.

[34] Y. Du, H. Liu, Y. Deng, P. D. Ye, *ACS Nano* **2014**, *8*, 10035-10042.

[35] A. Ambrosi, Z. Sofer, M. Pumera, *Angew. Chem. Int. Ed.* **2017**, *56*, 10443-10445.

[36] J. Kang, J. D. Wood, S. A. Wells, J.-H. Lee, X. Liu, K.-S. Chen, M. C. Hersam, *ACS Nano* **2015**, *9*, 3596-3604.

Chapter 5

Conclusion and Outlook

5.1 Conclusion

In conclusion, this PhD work focuses on the scalable exfoliation of van der Waals crystals (e.g. graphite, black phosphorus) into high-quality two-dimensional flakes by means of electrochemical engineering in solutions. In contrast to conventional physical or chemical exfoliation strategies by which the production of these materials has to compromise between scalability and quality, in this thesis, the electrolytic parameters including ionic species, working bias and cell configuration were systematically studied and carefully considered to enable low structural damage as well as high throughput capability of the exfoliated materials. The potential applications such as printable inks, flexible supercapacitors, lithium ion batteries were explored to evaluate the advantages of high-quality graphene. In each chapter, field effect transistors were fabricated to reveal the electronic properties of individual sheets.

Among all solvents that have been used for electrochemical exfoliation, water is certainly the optimal choice regarding its natural abundance and sustainability. However, water electrolysis generates massive radicals (e.g. hydroxyl radical). During exfoliation process, they continuously attack the graphite anode and leave oxygen-containing groups (e.g. hydroxyl group, epoxy group) on the exfoliated graphene, therefore seriously hamper the production of high-quality graphene. To address this problem, in the first chapter of this thesis, a series of reducing agents and radical scavengers have been investigated. In which, sodium borohydride, hydroiodic acid and hydrazine are expected to remove oxide groups from the exfoliated graphene; Ascorbic acid and some scavengers are introduced to capture hydroxyl radicals in the electrolyte. Specifically, a stable radical, namely (2,2,6,6-tetra-methyl-piperidin

-1-yl)oxyl (TEMPO), is very effective towards this end. In the presence of TEMPO, graphite exfoliation in aqueous solution of ammonium sulfate results in large graphene sheets (5-10 μm on average) with good quality in terms of excellent field-effect mobility (~405 $cm^2\ V^{-1}\ s^{-1}$), low I_D/I_G ratios (sub 0.1 in Raman spectra) and high carbon to oxygen (C/O) ratios (~25.3). Moreover, this wet-chemical protocol preserves the solution-processability of exfoliated flakes that ensures high-concentration graphene ink in DMF for printable electronics, transparent conductive films and flexible supercapacitors. In general, this robust electrochemical method provides opportunities for the scalable synthesis of high-quality graphene and the development of integrated graphene composites and graphene-based energy storage devices.

To date, significant research progress on the graphene-based devices or technologies has been achieved using high-quality graphene as conductive matrix or supporting layers. The mass production of high-quality graphene, especially in a cost-effective manner, must be realized to bridge the gap between bench studies and commercial prospects. The previous electrochemical strategies are based on a simple cell configuration including one graphite working electrode and one metallic counter electrode. However, the counter electrode does not contribute to overall production rate. To overcome this limitation, in the second chapter of this thesis, we have designed and fabricated a new power system to output alternating currents with tunable frequencies. The polarity of working bias switches every few seconds for the alternative intercalation of sulfate anions and quaternary ammonium cations in an organic sulfate solution. Compared to conventional exfoliation with direct current, alternating currents boost fast exfoliation at both graphite electrodes that largely enhances the production rate exceeding 20 g h^{-1} in laboratory tests. This scalable strategy also facilitates excellent exfoliation yield (~75 %, 1-3 layers), graphene sheets with low defect density (a C/O ratio of 21.2) and great electronic property (a hole mobility of 430 $cm^2\ V^{-1}\ s^{-1}$) thanks to the cathodic electrochemical reduction. The as-prepared high-quality graphene serves as an excellent building block for lithium-ion batteries. Graphene-wrapped lithium iron phosphate ($LiFePO_4$) particles deliver a high capacity of 167 mAh g^{-1} at 1 C rate after 500 cycles. The capacity is very close to the theoretical value of $LiFePO_4$ (170 mAh g^{-1}).

The electrochemical strategies are not only suitable for the graphene synthesis, but also attractive for the scalable exfoliation of semiconducting materials. Beyond graphene, black phosphorus (BP) is a promising material for the next-generation electronics and optoeletronics because of the intrinsic bandgaps. Unfortunately, pristine BP flakes produced by mechanical cleavage methods can hardly reach a large quantity. In the last chapter, great advances have been achieved through the cathodic delamination of bulk BP in an organic electrolyte. The interlayer spacing of BP crystal is expanded by incorporating ionic species with various diameters, leading to efficient intercalation/exfoliation process under oxygen-free condition. Especially, the intercalation of tetra-*n*-butyl-ammonium cations, followed by the insertion and reduction of solvated protons, results in high exfoliation yield up to 78 %. The exfoliated flakes are mainly few layers (average 7-8 layers) and exhibit great structural integrity with large lateral dimension. It is noteworthy that the BP flakes exhibit excellent electronic properties, well comparable to those of mechanically cleaved sheets. Based on exfoliated BP flakes, bottom-gate and bottom-contact field effect transistors reveal an average mobility of 195±15 $cm^2\ V^{-1}\ s^{-1}$ and a current on/off ratio of $(1.7\pm0.03)\times10^4$ at 300 K in vacuum. At low temperature (e.g. 143 K), the values are further increased to 252±18 $cm^2\ V^{-1}\ s^{-1}$ and $(1.2\pm0.15)\times10^5$, respectively. This approach opens up a new opportunity for the future development of BP-based technologies.

5.2 Outlook

For a long time, the bulk production of high-quality graphene flakes in economical and environmentally friendly manner holds the key to the graphene commercialization. The studies present in this thesis contribute a deeper insight into the electrochemical methods, which provide possible solutions to push graphene products to the market. The exfoliation process has been carefully studied to solve the scaling-up issues, improve graphene quality and prepare other semiconducting materials. However, the complete mechanisms behind the exfoliation are still not explicitly understood, there remains several issues for the future research, as detailed in the following sections.

5.2.1 Electrolytes

It has been demonstrated that the quality of 2D sheets is strongly dependent on the selection of electrolytes. The ideal electrolytes should induce effective intercalation of guest ions and produce gaseous species that subsequently separate the layers without causing any destruction of the 2D morphology, and also work as dispersants to stabilize the exfoliated flakes, avoiding re-aggregation. Moreover, the solvents can be easily removed when fabricating devices or preparing hybrid materials. For example, water is a universal solvent but problematic for anodic exfoliation due to the oxidation on working electrodes caused by water splitting. Cathodic exfoliation in organic solvents is able to avoid excess oxidation, however, in most cases, few-layer materials are the major products because of insufficient gas production. Beyond the monocomponent electrolytes, the studies on binary systems or mixed solvents may suggest right directions to achieve pristine thin flakes.

5.2.2 Exfoliation Mechanism

Owing to the high complexity of electrochemical reactions, the exfoliation process at the interfaces of layered materials is not trivial. Essentially, successful exfoliation involves three stages: intercalation of anions/cations, expansion of interlayer distance, and exfoliation from the electrode surfaces. In practice, exfoliation begins at any part of electrodes and these stages do not occur in order, which is the main reason for the wide distribution of exfoliated layers. It seems to be a trade-off between the efficiency of exfoliation and the preservation of sheet quality. The collaboration with *in-situ* characterization techniques (e.g. Raman, XRD, TEM), theoretical modeling and calculation are therefore important for an in-depth understanding of the fundamental mechanisms, which are crucial for the optimization of exfoliation processes to produce 2D sheets with homogeneous size and thickness distribution.

5.2.3 Exfoliation Conditions

The concentration of electrolytes, working bias, temperature and the quality of precursors are of great significance with respect to the production rate and material quality. For instance, graphite sources from different suppliers and synthetic methods, such as HOPG, expanded graphite, natural graphite flakes, graphite powder, graphite foil, graphite rod and graphite intercalated compounds, have variable oxygen contents and defect density. It is necessary to consider the starting materials and working conditions, according to the needs in diverse practical applications.

5.2.4 Equipment Engineering

To connect the laboratory-scale tests to industrial production, the design of electrochemical cells is essential. The working parameters and the connection of each step have to be rescheduled when increasing the size of cell. From an engineering point of view, continuous feeding and production, separation of exfoliated flakes from the cell, recycle use of electrolytes, precise control over exfoliation temperature, and removal of un-exfoliated impurities are considerable factors for the scale-up process.

5.2.5 Other Conductive Layered Materials

As introduced in chapter 1, many conductive or semi-conductive materials have drawn much attention in the recent years owing to their unique properties. However, the practical uses of these materials are hindered by low production yield and/or poor quality. Taking advantages of electrochemical strategy, the delamination of other (semi)conductive layered materials (e.g. antimony, tin selenide, transition metal dichalcogenides, etc) is able to realize, as they follow similar charge transfer and intercalation principles to those of graphite exfoliation.

5.2.6 Modification of Exfoliated Materials

Besides the attainment of high-quality or defect-free 2D materials, in the past years, electrochemical exfoliation has been applied for the synthesis of heteroatom-doped 2D materials or functionalized hybrids with organic moieties, polymers, nanoparticles or nanosheets. By changing basic parameters such as the electrolytes or introducing *in-situ* electrochemical reactions along the exfoliation process, the quality and properties of the 2D materials can be tailored to meet the demands of various applications. For example, the surface functionalization with organic molecules or conductive polymers is able to tune the dispersibility of exfoliated graphene in low boiling point solvents and control the electronic properties such as work function or band gap, which are necessary for ink-jet printed electronics, sensors or transistors.

List of Publications

1. **S. Yang,** A. G. Ricciardulli, S. Liu, R. Dong, M. R. Lohe, A. Becker, M.A. Squillaci, P. Samori, K. Müllen,* X. Feng,* Ultrafast Delamination of Graphite into High-quality Graphene using Alternating Currents, *Angew. Chem. Int. Ed.*, **2017**, 56, 6669; *Angew. Chem.* **2017**, 129, 6770.

2. **S. Yang,** M. R. Lohe, K. Müllen,* X. Feng,* New-Generation Graphene from Electrochemical Approaches: Production and Applications, *Adv. Mater.*, **2016**, 28, 6213. (*Review paper*)

3. **S. Yang,** S. Brüller, Z. S. Wu, Z. Liu, K. Parvez, R. Dong, F. Richard, P. Samori, X. Feng,* K. Müllen,* Organic Radical-Assisted Electrochemical Exfoliation for the Scalable Production of High-quality Graphene, *J. Am. Chem. Soc.*, **2015**, 137, 13927.

4. **S. Yang,** K. Zhang, A. G. Ricciardulli, P. Zhang, Z. Liao, M. Lohe, E. Zschech, W. Pisula, P. Blom, K. Müllen,* X. Feng,* A Delamination Strategy for Thinly Layered Defect-Free High-Mobility Black Phosphorus Flakes, *Angew. Chem. Int. Ed.*, **2018**, in press.

5. A.G. Ricciardulli, **S. Yang**, X. Feng, P. Blom,* Solution-Processable High-Quality Graphene for Organic Solar Cells, *ACS Appl. Mater. Interfaces*, **2017**, 9, 25412

6. A.G. Ricciardulli, **S. Yang**, G. A. H. Wetzelaer, X. Feng, P. Blom,* Hybrid Silver Nanowire and Graphene based Solution-processed Transparent Electrode for Organic Optoelectronics, *Adv. Funct. Mater.*, **2018**, 1706010.

7. J. Heodler, **S. Yang**, K. Müllen, X. Feng, K. Asadi,* Ferroelectric Field-Effect Transistors Based on Electrochemically Exfoliated Graphene, *Solid State Electron.*, **2018**, 144, 90.

8. G. Wang, J. Zhang, **S. Yang**, F. Wang, X. Zhuang, A. Narita, K. Müllen,* X. Feng,* Vertically Aligned MoS2 Nanosheets Patterned on Electrochemically Exfoliated Graphene for High-Performance Lithium and Sodium Storage, *Adv. Energy. Mater.*, **2017**, 1702254.

9. J. Li,* S. S. Deleka, P. Zhang, **S. Yang**, M. Lohe, X. Zhuang, X. Feng, M. Östling. Scalable Fabrication and Intergration of Graphene Microsupercapacitors through Full Inkjet Printing, *ACS Nano*, **2017**, 11, 8249.

10. Z. Liu, S. Liu, R. Dong, **S. Yang**, H. Lu, A. Narita, X. Feng,* K. Müllen,* High Power In-Plane Micro-supercapacitors Based on Mesoporous Polyaniline Patterned Graphene, *Small*,

2017, 13, 1603388.

11. Z. Liu, Z. S. Wu, **S. Yang**, R. Dong, X. Feng,* K. Müllen,* Ultraflexible In-Plane Micro-Supercapacitors by Direct Printing of Solution-Processable Electrochemically Exfoliated Graphene, *Adv. Mater.*, **2016**, 28, 2217.

12. M. Belekoukia, M. S. Ramasamy, **S. Yang**, X. Feng, G. Paterakis, V. Dracopoulos, C. Galiotis, P. Lianos,* Electrochemically Exfoliated Graphene/PEDOT Composite Film as Efficient Pt-free Counter Electrode for Dye-sensitized Solar Cells, *Electrochim. Acta*, **2016**, 194, 110.

13. W. Wei, G. Wang, **S. Yang,** X. Feng,* K. Müllen,* Efficient Coupling of Nanoparticles to Electrochemically Exfoliated Graphene, *J. Am. Chem. Soc.*, **2015**, 137, 5576.

14. Z. S. Wu, K. Parvez, S. Li, **S. Yang**, Z. Liu, S. Liu, X. Feng,* K. Müllen,* Alternating stacked Graphene-Conducting Polymer Compact Films with Ultrahigh Areal and Volumetric Capacitances for High-energy Micro-supercapacitors, *Adv. Mater.*, **2015**, 27, 4054.

15. Z. S. Wu, **S. Yang**, L. Zhang, J. Wagner, X. Feng,* K. Müllen,* Binder-free Activated Graphene Compact Film for All-Solid-State Micro-Supercapacitors with High Areal and Volumetric Capacitances, *Energy Storage Mater.*, **2015**, 1, 119.

16. K. Parvez, **S. Yang**, X. Feng,* K. Müllen,* Exfoliation of Graphene via Wet Chemical Routes, *Synth. Met.*, **2015**, 210, 123. (*Review paper*)

17. **S. Yang,** W. Yue,* J. Zhu and X. Yang,* Graphene-based Mesoporous SnO_2 with Enhanced Electrochemical Performance for Lithium-ion Batteries, *Adv. Funct. Mater.*, **2013**, 23, 3570.

18. **S. Yang**, W. Yue*, D. Huang, C. Chen, H. Lin and X. Yang*, “A Facile Green Strategy for Rapid Reduction of Graphene Oxide by Metallic Zinc”, *RSC Adv.*, **2012**, 2, 8827.

19. W. Yue,* **S. Yang**, Y. Liu, X. Yang,* A Facile Synthesis of Mesoporous Graphene-Tin Composites as High-Performance Anodes for Lithium-ion Batteries, *Mater. Res. Bull.*, **2013**, 48, 1575.

20. W. Yue,* **S. Yang**, Y. Ren, X. Yang,* In situ Growth of Sn, SnO on Graphene Nanosheets and Their Application as Anode Materials for Lithium-ion Batteries, *Electrochim. Acta*, **2013**, 92, 412.

Acknowledgements

First of all, I would like to dedicate my deepest gratitude to Prof. Dr. [redacted] for his unwavering support, constant encouragement and helpful advices along the entire journey of my scientific adventure. His passion and wisdom in science has always inspired me with my research.

Next I sincerely appreciate Prof. Dr. [redacted] for sharing his knowledges and experiences, giving sustainable guidance, insightful discussion and innovative ideas for work progress. I would also thank him for his kindness and efforts regarding the revision of reports, manuscripts and thesis.

My acknowledgement also extends to my colleagues and collaborative partners from Max Planck Institute for Polymer Research (MPI-P), Technische Universität Dresden (TUD) and University of Strasbourg for their kind support and cooperation.

MPI-P: Dr. [redacted] gave me a nice introduction into the standard techniques of electrochemical exfoliation. The AFM instruction from [redacted] was valuable for me to understand the thickness of 2D structure. [redacted] provided me good guidance on how to fabricate the graphene devices using focused ion beam. Dr. [redacted] showed me the steps of Raman measurements. Dr. [redacted] helped me with the assembly and measurements of flexible supercapacitors. Dr. [redacted] inspired me with some nice ideas regarding the radical scavengers. [redacted], Prof. [redacted] and Prof. [redacted] assisted me with the studies on field effect transistors. Dr. [redacted] carried out high resolution TEM for graphene samples. [redacted] performed X-ray diffraction with graphene powder and black phosphorus films. Dr. [redacted] shared his instruments and hood with me. [redacted] was always warm-hearted and helpful with lab issues. Dr. [redacted] taught me the knowledge of organic synthesis. Dr. [redacted] helped me with the experiments of three-electrode supercapacitors. [redacted] made the power supply for alternating currents. [redacted]

[redacted] fabricated the devices and performed AFM measurements for the research work on BP.

TUD: Dr. [redacted] helped with patent applications and was kind with work coordination. Dr. [redacted] provided me the precursors for exfoliation. Dr. [redacted] collected the Raman spectra for graphene samples. Dr. [redacted], [redacted] and [redacted] managed to keep a good working environment in the lab and office. Dr. [redacted] was always willing to make TEM measurements. Dr. [redacted], [redacted] and Dr. [redacted] performed the SEM investigations and elemental mapping.

I would like to thank Prof. [redacted], Dr. [redacted] and Dr. [redacted] (University of Strasburg, France) for the measurements and discussion of XPS; Dr. [redacted] and Prof. [redacted] (Fraunhofer Institute for Ceramic Technologies and Systems, Germany) for high resolution TEM; Dr. [redacted] and Dr. [redacted] (Leibniz Institute for Solid State and Materials Research, Germany) for *in-situ* Raman spectroscopy and theoretical studies.

In addition, I want to express my appreciations to all the members in the groups of Prof. [redacted] at MPI-P and Prof. [redacted] at TUD, including Dr. [redacted], Dr. [redacted], Dr. [redacted], Dr. [redacted], Dr. [redacted], Dr. [redacted], [redacted], [redacted], Dr. [redacted], Dr. [redacted], Dr. [redacted], Dr. [redacted], [redacted], Dr. [redacted], Dr. [redacted], Dr. [redacted], [redacted], [redacted], [redacted], Dr. [redacted], Dr. [redacted]… If anybody is missing here, please forgive me for unintentional omissions.

At last, special thanks are dedicated to my parents and sister, for their everlasting trust and unconditional love that always inspire me in my life, from the past to the future.